

Stresses in nanocrystalline materials

Von der Fakultät Chemie der Universität Stuttgart
zur Erlangung der Würde eines Doktors der Naturwissenschaften (Dr. rer. nat.)
genehmigte Abhandlung

vorgelegt von

Jianfeng Sheng

aus Ningxia, China

Hauptberichter:	Prof. Dr. Ir. E. J. Mittemeijer
Mitberichter:	Prof. Dr. J. Bill
Prüfungsvorsitzender:	Prof. Dr. R. Niewa

Tag der Einreichung:	21.05.2010
Tag der mündlichen Prüfung:	26.07.2010

MAX-PLANCK-INSTITUT FÜR METALLFORSCHUNG STUTTGART
INSTITUT FÜR MATERIALWISSENSCHAFT DER UNIVERSITÄT STUTTGART

Stuttgart, 2010

*Dedicated to my parents, my wife, my son, and
Granny Berta Kleimenhagen*

Content

1. General introduction	9
1.1. <i>Nanostructured materials</i>	11
1.1.1. Classification of nanostructured materials	11
1.1.2. Characteristics of nanostructured materials	12
1.1.3. Fabrication	14
1.2. <i>Stress and diffusion in thin-film diffusion couples</i>	18
1.2.1. Classification of film stress	18
1.2.2. Relationship between stress and diffusion	19
1.3. <i>Size-dependence of lattice parameter</i>	20
1.3.1. Size-dependent phenomena	20
1.3.2. Size-dependence of lattice parameters of nanocrystalline metals	21
1.4. <i>Main methods for characterization</i>	22
1.4.1. X-ray diffraction	23
1.4.2. Sputter-depth profiling using Auger Electron Spectroscopy	27
1.5. <i>Outline</i>	31
<i>References</i>	32
2. Interdiffusion, solid solution formation and decomposition and stress development in thin-film Ni-Cu diffusion couples	37
2.1. <i>Introduction</i>	38
2.2. <i>Experimental details</i>	40
2.2.1. Preparation of bilayers, single layers and alloy layers	40
2.2.2. Microstructure investigation	41
2.2.3. Concentration-depth profiling	41
2.2.4. Phase and texture analysis and macrostress evaluation	43
2.3. <i>Results and discussion</i>	45
2.3.1. Microstructure	45
2.3.2. Diffusional intermixing	50
2.3.3. Formation and decomposition of the (Cu, Ni) solid solution	52
2.3.4. Stress development	55
2.4. <i>Conclusions</i>	63

References	65
3. Non-monotonic crystallite-size dependence of the lattice parameter of thin films of metals	69
3.1. Introduction	70
3.2. Experimental details	71
3.2.1. Specimen preparation	71
3.2.2. Ex situ and in-situ X-ray diffraction measurements and their evaluation	71
3.3. Results	73
3.4. Discussion	77
3.5. Conclusion	79
References	81
4. The lattice parameter of nanocrystalline Ni as function of crystallite size	83
4.1. Introduction	84
4.2. Experimental procedures and data evaluation	85
4.2.1. Specimen preparation and processing	85
4.2.2. Microstructure investigation	86
4.2.3. Ex situ and in situ X-ray diffraction measurements and their evaluation	88
4.3. Results	93
4.3.1. Microstructure of the Ni layer	93
4.3.2. Non-monotonic size-dependence of the lattice parameter of Ni thin film	96
4.3.3. Microstructure of the ball-milled Ni powder	97
4.3.4. Non-monotonic size-dependence of the lattice parameters of Ni powder	100
4.4. Discussion	101
4.5. Conclusion	104
References	105
5. Summary	109
6. Kurzfassung der Dissertation in deutscher Sprache	119
List of publications	131
Acknowledgement	133
Curriculum Vitae	135

1. General introduction

“I can't see exactly what would happen, but I can hardly doubt that when we have some control of the arrangement of things on a small scale we will get an enormously greater range of possible properties that substances can have, and of different things that we can do. ” Richard Feynman said in late 1959 [1]. Nowadays, his prediction turns into reality as research in the field of nanotechnology has become one of the most important, but also one of the most vibrant areas in science.

Nanotechnology involves the use of nanomaterials, i.e. materials with at least one dimension smaller than a one tenth of a micrometer. The investigations of nanomaterials focus particularly on such materials which have special properties, as compared to their bulk counterparts, stemming from their nanoscale dimensions [2]. Nanomaterials are not an invention of the 20th century, but such materials have been used unwittingly for centuries: As an example, a Luster technique was used for generating a glittering effect on the surface of pots [3]. The first rigorous scientific study in this field was done by Michael Faraday, who investigated the optical properties of nanometer-scale metals in the 1850s [4].

The “size effect” is one of the most important aspects of nanostructured materials as pronounced changes of the properties of solids (e.g. coefficient of thermal expansion [5], Young's modulus [6], magnetic properties [7], plastic behavior [8], etc) can occur when the crystallite size is reduced [9]. A thorough understanding of the size effect is important both for controlling and optimizing the properties of nanomaterials as nanoparticles and nanostructured (e.g. nanocrystalline) bulk materials.

A prominent example is the plastic behavior of nanocrystalline metallic materials. Compared with conventional coarse-grained materials, ultrahigh yield and

fracture strengths, superior wear resistance, and possibly superplastic formability at low temperatures and/or high strain rates can be achieved by nanostructuring [10]. These drastic changes in the plastic behavior occur, as the plasticity of nanostructured materials is dominated by grain-boundary deformation, whereas dislocation movement at relatively low temperature and diffusional creep at higher temperatures dominate the plastic behavior of coarse-grained metals [11].

Nanotechnology requires methods both for the controlled preparation of nanomaterials and their characterization. Important milestones in the fabrication of nanomaterials were the preparation of fullerenes [12], carbon nanotubes [13], quantum dots [14], etc. For metallic nanocrystalline materials, inert gas condensation (IGC) and *in-situ* consolidation [15], electrodeposition [2] as well as severe plastic deformation [16] constituted important landmarks.

The characterization of nanomaterials made important advancements both by the extension of established methods of characterization as diffraction [17], as well as by the invention of dedicated techniques as scanning tunneling microscopy [18-19].

This work addresses in particular the relationship between stress and diffusion in nanocrystalline Ni-Cu thin films and the size dependence of the lattice parameters of nanocrystalline metals (Cu, Ni, and Pd). *In-situ* X-ray diffraction (XRD) measurements combined with complementary methods such as transmission electron microscopy (TEM), atomic force microscopy (AFM) and Auger electron spectroscopy (AES) in combination with sputter-depth profiling were employed.

Considerable diffusional intermixing, accompanied by the formation of the (Cu,Ni) solid solution and considerable stress changes in the thin bi-layer diffusion couples of Cu and Ni have been observed and analyzed quantitatively.

A non-monotonic crystallite-size dependence of the lattice parameter of nanocrystalline Ni, i.e., *lattice contraction* followed by *lattice expansion* with decreasing crystallite size, has been observed for the first time in contrast with the monotonic lattice contraction of the lattice parameter of nanocrystalline Cu and nanocrystalline Pd with decreasing crystallite size observed in this work. The variation of the lattice parameter of nanocrystalline metals is explained by considering the influences of interface stress and intracrystalline pressure. Moreover, in order to

explain all the experimental findings in this work, the influence of the change of spin interaction during the transition from multidomain to a single domain for ferromagnetic materials has been discussed.

1.1. Nanostructured materials

1.1.1. Classification of nanostructured materials

Nanostructured materials may contain crystalline, quasicrystalline, or amorphous phases and can be metals, ceramics, polymers or composites. If the materials are composed of nanosized crystals, the material is termed nanocrystalline. On the other hand, if the materials are composed of amorphous or quasicrystalline phases, they are called nanoglasses [20]. Nanostructured materials can be classified into different categories on the basis of their geometrical shape and on the number of dimensions in which the material has nanometer modulations. Siegel classified nanostructured materials into four categories according to their dimensionality namely 0D (nanoclusters), 1D (multilayers), 2D (nanograined layers), and 3D (equi-axed bulk solids) (see Fig. 1.1) [21]. Gleiter further classified the nanostructured materials according to composition, morphology, and distribution of the nanocrystalline component (see Fig. 1.2) [9].

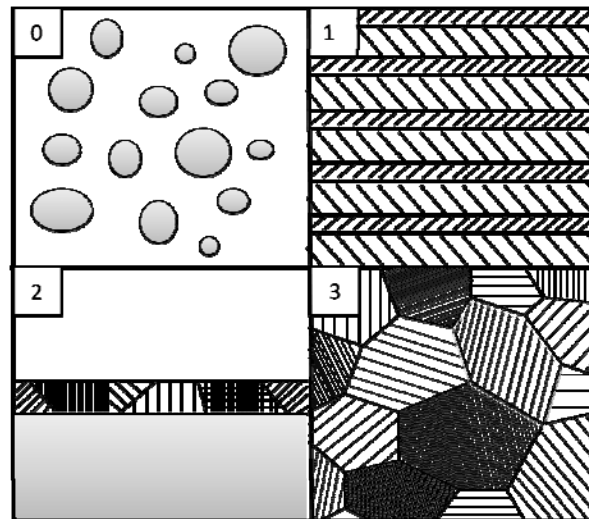


Fig. 1.1 Schematic of the four types of nanostructured materials: “0” – zero dimensional; “1” – one dimensional; “2” – two dimensional; “3” – three dimensional (redrawn after Ref. [21]).

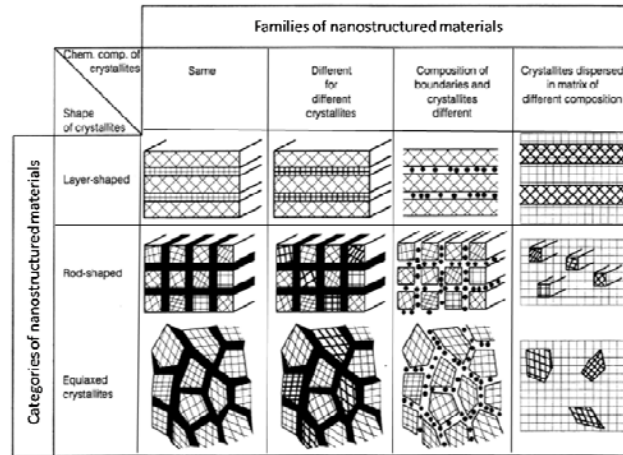


Fig. 1.2. Classification scheme for nanostructured materials taking into account both the dimensionality and the chemical composition of the nanostructured regions. The boundary regions of the first and the second family of nanostructured materials marked in black highlight the different atomic arrangements in the crystallites and in the boundaries (redrawn after Ref. [9]).

1.1.2. Characteristics of nanostructured materials

Due to the reduced dimension(s), nanostructured materials contain a high number of interfaces and surfaces. Thus, the volume fraction of atoms residing in the grain boundaries or at surfaces, respectively, is substantial. In contrast, for coarse-grained materials with a grain size exceeding 1 μm , the volume fraction of atoms in the grain boundaries is negligible. As an example, a nanocrystalline metal contains typically a high number of interfaces (about $6 \times 10^{25} \text{ m}^{-3}$ for a 10 nm grain size) with random orientation relationships, and consequently, a substantial fraction of atoms lie in the interfaces.

Assuming that grains have the shape of spheres or cubes, the volume fraction of nanocrystalline materials associated with the boundaries can be calculated as [22]:

$$C = \frac{3\Delta}{d} \quad (1.1)$$

where Δ is the average grain boundary thickness and d the average grain diameter. Thus, the volume fraction of atoms in the grain boundaries can be as much as 50% for

General introduction

5 nm grains and decreases to about 30% for 10 nm grains, and to about 3% for 100 nm grains.

With decreasing grain size below about 20 nm, the triple junction (i.e., intersection lines of three or more adjoining crystals) becomes an important component of the microstructure, and the volume fraction of the triple junction displays greater grain size dependence than the grain-boundary volume fraction as shown in Fig. 1.3. The triple junction volume fraction increases by three orders of magnitude as the grain size decreases from 100 nm to 2 nm, while in the same range the grain boundary volume fraction increases by only a little over one order of magnitude.

A schematic representation of a hard sphere model of an equiaxed nanocrystalline metal is shown in Fig. 1.4, from which it can be concluded that nanocrystalline materials can be considered to consist of two structural components, namely small crystallites with long-range order and different crystallographic orientations and a network of intercrystalline regions, with structural variations from region to region.

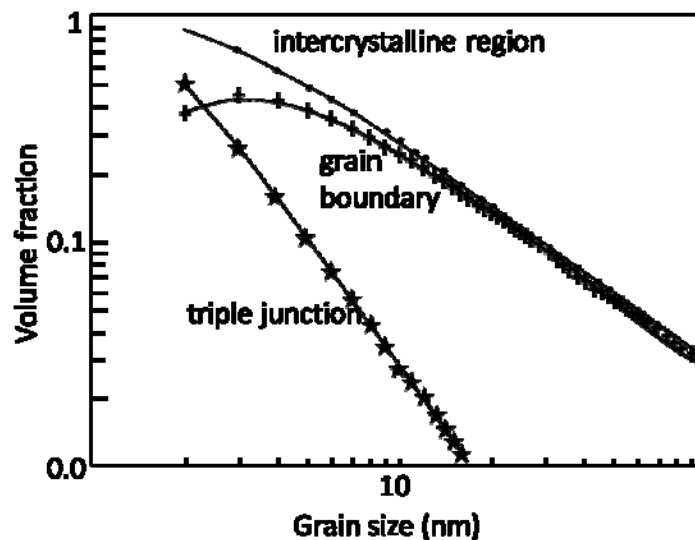


Fig. 1.3. Influence of grain size on volume fractions of intercrystalline regions and triple junctions with an assumption that the grain-boundary thickness is 1 nm (redrawn after Ref. [23]).

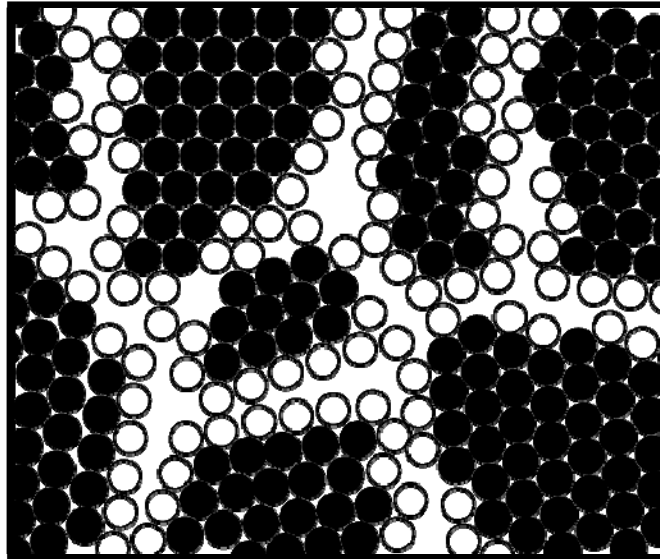


Fig. 1.4. Schematic for a nanocrystalline metal showing atoms associated with the individual grains (black dots) and those constituting a grain boundary network (open circles) (figure redrawn after Ref. [9]).

1.1.3. Fabrication

Nanomaterials can be synthesized via vapour, liquid, and solid-state processing routes. Methods for the fabrication of nanocrystalline material have been gathered in Table. 1.1

Table 1.1. Methods for the fabrication of nanocrystalline materials [20].

Starting phase	techniques
vapour	inert gas condensation – IGC
	physical vapour deposition (sputtering, evaporation) – PVD
	chemical vapour deposition – CVD
	atomic layer deposition – ALD
liquid	electrodeposition – ED
	rapid solidification
solid	mechanical milling – MM
	equal channel angular pressing – ECAP
	high pressure torsion – HPT

General introduction

In the following, two methods relevant to this work, namely physical vapour deposition and mechanical milling, will be discussed in more detail.

1.1.3.1. Thin-film fabrication

Thin films can be prepared employing a variety of deposition methods as physical vapour deposition (PVD) [24], chemical vapour deposition (CVD) [24-25], atomic layer deposition (ALD) [26], electrodeposition and thermal spraying [27].

PVD deposition processes can be facilitated by methods such as magnetron sputtering, arc evaporation, and pulsed laser deposition. In this work, magnetron sputtering has been employed for thin film deposition. The magnetron sputtering process is illustrated in

Fig. 1.5: Sputtering is the removal of atoms from a solid due to bombardment of its surface layer by ions or neutral particles. A negative voltage (typically of the order of some 100 V) applied to the target accelerates positively charged ions towards the target, whereas electrons are accelerated in an opposite direction. These electrons can collide with gas atoms (often Ar is used as an inert gas) and create new ion-atoms pairs such that a self-sustaining plasma develops in the near-target region. Upon collision of a positive gas ion with atoms at the surface of a solid, an energy and momentum transfer occurs. If the energy transferred to an atom is sufficiently large, primary recoil atoms can be created which can collide with other atoms and distribute their energy via collision cascades. A surface atom can be sputtered of the surface if the energy transferred to it normal to the surface is larger than about 3 times the surface binding energy (i.e. approximately equal to the heat of sublimation).

The sputter process can be enhanced by applying a suitably oriented magnetic field: Electrons with a velocity component perpendicular to the magnetic field lines are forced on spiral paths around the magnetic field lines due to the action of the Lorentz force. Due to the longer spiral path, as compared to a straight path, more ionizing collisions with neutral gas atoms occur. This enhances the ionisation of the plasma near the target leading to a higher sputter rate. It also implies that the plasma can be sustained at a lower pressure. The sputtered atoms are neutrally charged and so are unaffected by the magnetic trap. This variant of sputtering is called magnetron sputtering.

The microstructure of thin films prepared by PVD methods is very sensitive to various deposition parameters such as magnetron power, temperature and gas pressure. Various structure-zone models have been proposed to describe the morphology of PVD thin films: A first proposal by Movchan and Demichishin in 1969 [28] was followed by the four-zone model of Thornton [29], detailed studies of the substrate temperature [30] and the proposal of a revised four-zone model by Messier *et al.* [31]. In this context, the grain sizes of the sputtered thin-films have been successfully adjusted by tuning the deposition parameters.

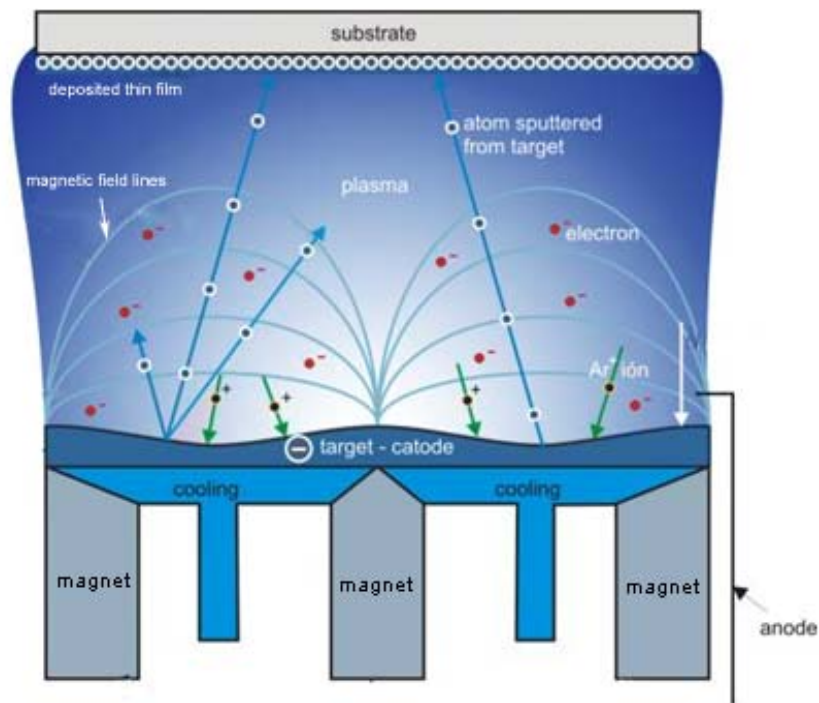


Fig. 1.5. Schematic representation of the process of direct-current magnetron sputtering (redrawn after Ref. [32]). For details, see text.

1.1.3.2. Nano-crystalline metal powders prepared by mechanical milling

The use of milling devices such as attrition mills, shaker mills and planetary ball mills has attracted considerable attention during the past 15-20 years [16]. Whereas mechanical milling characterizes a milling process of powders of uniform composition, such as pure metals, intermetallics or pre-alloyed powders, mechanical alloying refers to milling processes involving mixtures of powders to produce a solid solution, intermetallic phases or amorphous materials. Reaction milling is a variant of mechanical alloying involving the occurrence of solid-state reactions [33].

The working principle of a planetary ball mill is shown in Fig. 1.6. The mill consists of one turn disc and up to four milling vessels. The turn disc rotates in one direction while the vessels rotate in the opposite direction. The centrifugal forces created by the rotation of the vessel around its own axis together with the rotation of the turn disc are applied to the powder mixture and milling balls in the vessel. Since the directions of rotation of the vessel and the turn disc are opposite, the centrifugal forces are alternately synchronised. Friction results from the milling balls and the powder mixture being ground alternately by rolling of the milling balls along the inner wall of the vessel, and impact results when they are lifted and thrown across the bowl to strike at the opposite wall. The impact is intensified when the balls strike one another. The impact energy of the milling balls in the normal direction attains a value of up to 40 times higher than that due to gravitational acceleration. The powder particles are then fractured and cold welded under the high-energy impact [34].

The impact energy of the milling balls is changeable by altering the rotational speed of the turn disc. The advantage of this type of ball mill is not only that high impact energy could be obtained but also that a high impact frequency results which can shorten the required duration of the milling process. The materials of the milling case and milling ball can be made of the same material as the powder in order to avoid contamination of the powder with wear from balls and/or the vessel. Based on powder particle size and impact energy required, balls with sizes of 10 to 30 mm are normally used.

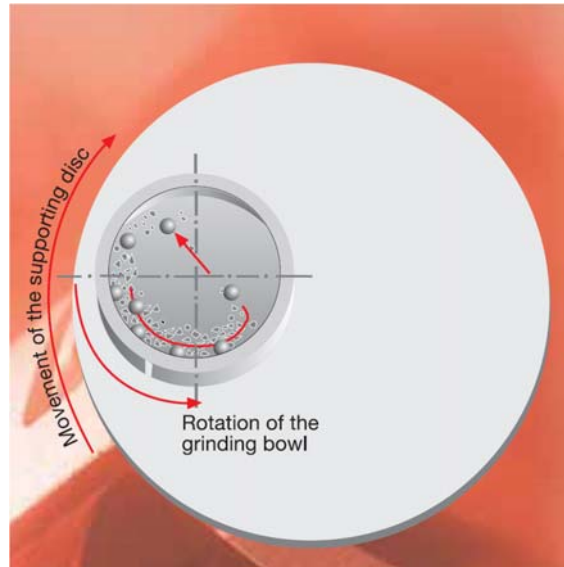


Fig. 1.6. Schematic of the working principle of planetary ball-milling [35].

1.2. Stress and diffusion in thin-film diffusion couples

1.2.1. Classification of film stress

Virtually any thin film bonded to a substrate directly (single layer) or indirectly (multilayer) is subjected to appreciable residual stresses [25]. Residual stresses of thin films can be first categorised into *intrinsic stresses* and *extrinsic stresses*. *Intrinsic stresses* arising during the film growth can be due to surface/interface stresses, cluster coalescence to reduce surface area, grain growth, vacancy annihilation, shrinkage of grain-boundary voids, incorporation of impurities, phase transformations and precipitation, epitaxy etc. [36]. *Extrinsic stress* can occur after completion of the deposition due to external influences as due the difference of thermal expansion coefficients between the film and the substrate when temperature changes, electrostatic or magnetic forces, etc [25].

The residual stresses can further be divided into three additive stresses namely the average of the residual stresses over many grains, σ_1^{RS} , the difference between the average of the residual stress over one particular grain and σ_1^{RS} , and the deviation of the local stress in a particular grain from the average stress in the grain (see Ref. [37] and the references therein).

1.2.2. Relationship between stress and diffusion

The stress state in a thin film can be altered due to diffusion [38-39], and the stress state and its evolution, in turn, can influence the diffusion process. The effect of stress on diffusion is well known for the case of a hydrostatic state of stress: the diffusivity is influenced via the so-called activation volume [40]. The case of a non-hydrostatic stress state, however, has received much less attention both theoretically and, in particular, experimentally. Pioneering theoretical work in this field is due to Cahn and Larché [41]. It followed that stress gradients can act as driving forces for diffusion.

During thermal treatments of thin films, usually more than one mechanism influencing the stress state is operative: As an example, interdiffusion in a layered structure is often accompanied by the annihilation of crystal defects and by grain growth. Above all, plastic accommodation of strains may occur if the yield limit is exceeded. In spite of its scientific and technological importance, systematic investigations of the effect of interdiffusion on residual (internal) stresses in thin films are rare [42-45].

The various mechanisms affecting the stress state such as thermal expansion mismatch, grain growth, defect annihilation and the shrinkage of grain-boundary voids, (inter)diffusion, phase formation, and plastic deformation can be discerned by investigating stress changes of a bi-layer system and by comparing stress variations of bilayers with those of single layers prepared under identical conditions [46].

In the present work, diffusion and stresses in the binary thin-film system Ni/Cu has been investigated. The Cu-Ni system exhibits miscibility at all compositions above about 350°C and absence of intermediate or ordered phases in Ni-Cu alloys. A miscibility gap occurs below about 350°C. The interdiffusion and stress evolution in thin bi-layer (individual layer thickness: 50 nm) diffusion couples of Cu and Ni have been investigated employing Auger-electron spectroscopy in combination with sputter-depth profiling and *ex-situ* and *in-situ* X-ray diffraction measurements. It has been found that upon annealing at relatively low temperatures (125°C to 300°C) for durations up to 100 hours considerable diffusional intermixing, accompanied by considerable stress changes, occurs. In addition, single layers of Ni and Cu have been investigated. The specific residual stresses that emerge due to diffusion between the (sub)layers in the bilayer could then be identified by comparing the stress changes in

the bilayer system with corresponding results obtained for single layers of the components in the bilayer system under identical conditions.

1.3. Size-dependence of lattice parameter

1.3.1. Size-dependent phenomena

When the size scale of nanostructured (e.g. nanocrystalline) materials drops below 100 nm, various properties exhibit appreciable changes as compared to bulk (coarse-grained) materials. Fig. 1.7 gives a vivid example of the size dependence of the colours of CdTe nanoparticles [47]. In addition to large surface/interface-to-volume ratios, the surface, interface, and quantum effects start to play a role with decreasing particle size, which is normally inconsequential for bulk materials. Variations of physical properties such as mechanical strength [6], plasticity [48], sintering and alloying ability [49], diffusivity [50], magnetic properties [51-52], thermodynamic properties [53] as well as the mode of crystal growth (self-assembly) have been found to be dependent upon particle size. As one example, the size dependence of the intrinsic coercivity is schematically shown in Fig. 1.8, which indicates a non-monotonic variation of the intrinsic coercivity with decreasing particle diameter due to the size-induced change of the magnetic structure.



Fig. 1.7. Fluorescence of colloidal CdTe nanoparticles of different size (reprinted with permission) [47].

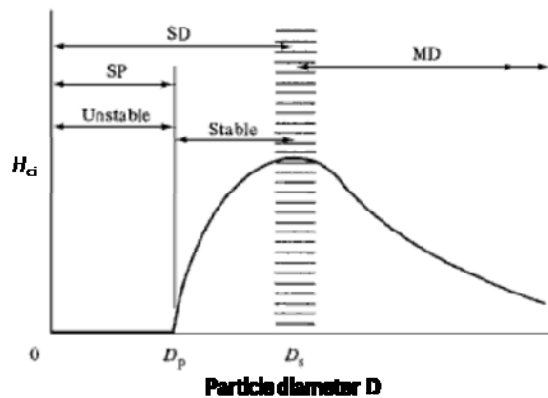


Fig. 1.8. Schematic for the intrinsic coercivity H_{ci} as function of particle diameter D (redrawn after Ref. [54]). MD, SD and SP denote the multi-domain, single domain, and superparamagnetic behaviour, respectively.

1.3.2. Size-dependence of lattice parameters of nanocrystalline metals

The size dependence of the crystal-lattice parameter was first studied in the 1930s mainly employing electron diffraction [55-57], and was further confirmed in 1951 [58]. Although the size dependence of the crystal-lattice parameter(s) has been frequently investigated, the experimental and theoretical results obtained until now are inconclusive: With decreasing crystallite size, the lattice parameters of nanocrystalline materials can, apparently, both contract (for example, Cu [59], Au [60], Sn [61] and Bi [61]) and expand (for example, Nb [62] and Ge [63]). Moreover, inconsistent experimental results have been presented: for example, both lattice contraction in Ni [64] and Pd [65], and lattice expansion in Ni [66-68] and Pd [69] have been reported. Several models/approaches have been proposed to understand the crystallite-size dependence of the lattice parameter(s). These consider the roles of, for example, intracrystalline pressure [66, 70], interface stress [71], interfacial excess volume [72], grain-boundary enthalpy [73], excess grain-boundary volume [74] and the Madelung theory [75]. However, these explanations are of limited generality and none of them can explain all experimental findings.

In this work, the crystallite-size dependence of the lattice parameters of nanocrystalline Cu, Ni, and Pd thin films, with crystallite sizes ranging from about 10 nm to 95 nm, have been investigated using an *in-situ* X-ray diffraction technique.

A dedicated annealing procedure called “loop annealing” was devised, which allows a quicker and more precise determination of the correlation between lattice parameter and crystallite size using one single specimen. To this end, a nanocrystalline specimen is subjected to heat treatments at increasing temperatures to induce coarsening of the crystallite size in a heating chamber mounted on the diffractometer and the lattice parameters are determined after successive anneals at (about) ambient temperature. The lattice contractions of Cu and Pd were confirmed, whereas, for the case of Ni, a non-monotonic variation of the lattice parameter with respect to crystallite size was observed for the first time, i.e., both lattice contraction and later lattice expansion can occur, depending on the range of crystallite size considered. These results are discussed in the light of different models describing the crystallite-size dependence of the lattice parameters. Moreover, the role of a change of spin interaction, during the magnetic structural transition from multi-domain to single domain below the “critical size” of about 40 nm, was discussed for Ni.

1.4. Main methods for characterization

The aim of this dissertation is to study the relationship between (inter)diffusion and stress in thin films and the size dependence of the lattice parameter of nano-sized thin films and powders. X-ray diffraction (XRD) measurements and Auger electron spectroscopy (AES) measurements in combination with sputter-depth profiling constituted the principal methods of investigation, which were complemented with transmission electron microscopy (TEM) and atomic force microscopy (AFM).

XRD measurements can be employed for phase identification as well as the determination of lattice parameters, crystallite size, microstrain, crystallographic texture, lattice strain and thus residual stress at either ambient temperature or elevated temperature without destroying the specimens. AES combined with sputter-depth profiling allows a quantitative determination of the elemental composition of the thin-film diffusion couples as function of sputter depth, which is very useful for investigating ex-situ interdiffusion occurring during thermal treatments.

TEM and AFM investigations were employed for complementing the microstructural investigations.

1.4.1. X-ray diffraction

X-ray diffraction analysis is a very powerful tool to quantitatively assess in particular the crystalline imperfection of materials, that is of cardinal importance for materials properties. The characteristic radiation emitted from an X-ray tube or medium-energy synchrotron radiation ($E=5-15$ keV) is ideally suitable for investigating the microstructure of films and surface layers due to its rather limited penetration depth in solid matter. For more detailed information about the basic principles of X-ray diffraction, the reader is referred to dedicated books [76-78] and references therein.

In the following, the two reference frames shown in Fig. 1.9 will be employed: The specimen reference frame (S), in which the S_3 axis is oriented perpendicular to the specimen surface with the S_1 and S_2 axes lying in the surface plane, and the laboratory reference frame (L), in which L_3 is always parallel to the diffraction vector. The two angles, the rotation angle φ around the specimen surface normal, and the angle between the specimen surface normal and the diffraction vector, ψ , are employed to describe the orientation relationship between the specimen reference frame, S , and the laboratory reference frame, L [37].

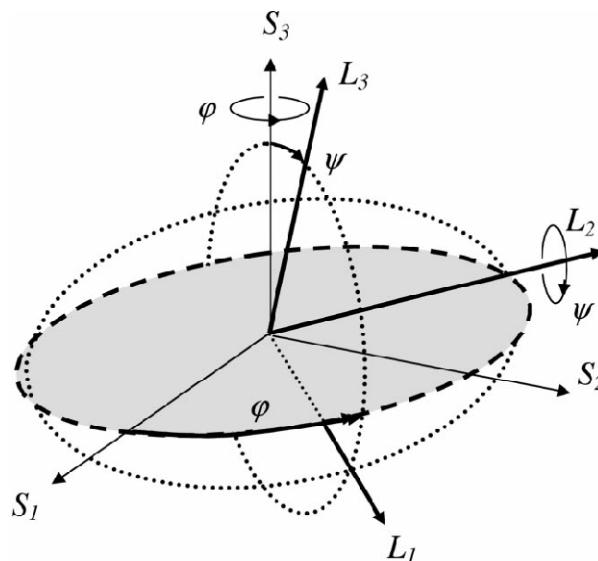


Fig. 1.9. Definition of, and relations between, the sample (S) and laboratory (L) reference frames [37].

1.4.1.1. Crystallographic texture

Crystallographic texture usually occurs in polycrystalline thin films. As a consequence, the fractional intensities of reflections may deviate from the fractional intensities expected for an untextured (ideal powder) specimen; it can even occur that some reflections of thin film samples may be absent in a normal θ - 2θ scan (with the diffraction vector oriented perpendicular to the specimen surface).

The experimental investigation of crystallographic texture can be done employing X-ray diffraction pole figure measurements, which were proposed already in 1927 by the German metallurgists Wever and Schmid. A pole figure is a stereographic projection, with a specified orientation relative to the specimen frame of reference, which shows the variation of the pole density with pole orientation for a selected set of crystal planes [78]. The pole figure is measured at a fixed diffraction angle (constant d spacing) and consists usually of a series of φ -scans at different tilting ψ angles (for the definitions of the angles, see Fig. 1.9).

1.4.1.2. Stress evaluation

Various methods have been devised to evaluate stresses in a thin film, coating, multilayer or the surface region of a bulk material according to the type of specimen and the measurement conditions such as the $\sin^2\psi$ method, the $g(\psi, hkl)$ method and the crystallite-group method, etc [37, 79]. In this work, the crystallite-group method (CGM) is employed to evaluate the stresses as a strong and sharp fibre texture exists in the single layer or multi-layer specimens investigated. The method was proposed by Willemsse *et al.* in 1982 [80] and has been successfully adapted to cold-worked specimens and fibre-textured specimens (see Ref. [37] and references therein).

The crystallite groups, i.e. all crystallites with the same orientation, are treated as being one crystal. For the in-plane, biaxial and rotationally symmetric state of stress (for example, the stress state in thin films), the calculation of the stress can be simplified as shown in Table 1.2 [79].

Table 1.2. Simplified $\sin^2\psi$ laws and the corresponding strain-free directions (indicated by ψ^*) for differently fibre-textured specimens consisting of cubic materials. The S_{ij} are the components of the single-crystal compliance tensor in Voigt notation and $S_0 = S_{11} - S_{12} - 1/2S_{44}$.

crystallite group	simplified $\sin^2\psi$ law	$\sin^2\psi^*$
{111}	$\epsilon_\psi = \left(2S_{12} + \frac{2}{3}S_0 + \frac{1}{2}S_{44} \sin^2\psi\right) \sigma_\parallel$	$\sin^2\psi^* = \frac{-2S_{12} - \frac{2}{3}S_0}{\frac{1}{2}S_{44}}$
{100}	$\epsilon_\psi = \left(2S_{12} + \left(S_0 + \frac{1}{2}S_{44}\right) \sin^2\psi\right) \sigma_\parallel$	$\sin^2\psi^* = \frac{-2S_{12}}{S_0 + \frac{1}{2}S_{44}}$

1.4.1.3. Crystallite size and microstrain

The existence of crystal imperfections, as finite crystallite size, dislocations, planar faults etc., in polycrystalline materials invariably results in the broadening of the Bragg reflections. The width and shape of diffraction lines of crystalline materials contain a wealth of microstructural information: Compositional inhomogeneity, the crystallite size and shape distributions and the concentrations and distributions of crystal defects such as vacancies, dislocations, stacking and twin faults. In many cases such information is not easily and statistically assured accessible by methods other than diffraction [76].

The analysis of diffraction-line broadening evolved already very shortly after the discovery of diffraction of X-rays: Already in 1918, Scherrer revealed that the line breadth varied inversely with the crystallite size. Since these early days of line profile analysis (LPA), numerous approaches have been established to extract the crystallite size and the microstrain such as the Williamson-Hall analysis, the single-line method, the Warren-Averbach analysis and whole powder pattern modelling (WPPM) (for further details, see Refs. [76, 81-83] and the references therein).

The integral breadth methods involve the use of analytical functions to describe the diffraction line profiles. For the single-line method employed in this work, a diffraction line is conceived as a convolution of a Gaussian and a Lorentzian (also called Cauchy) profile (i.e. as a Voigt function), where the Gaussian component is due

to microstrain and the Lorentzian component is due to finite crystallite size (for details, see Ref. [81] and references therein). More sophisticated methods for the analysis of the diffraction-line broadening exist [81]. However, the single-line method can be employed relatively easily and rapidly (as only one particular diffraction line has to be recorded) to obtain estimates for the size of the coherently diffracting domains D and the microstrain ε and, in particular, to observe the evolution of these parameters *in-situ* as function of temperature.

1.4.1.4. *In-situ* X-ray diffraction measurements

The *in-situ* X-ray diffraction (XRD) technique is a powerful approach for (residual) stress measurement. To perform *in-situ* X-ray diffraction stress measurements, it is essential to record diffractograms as fast as possible. For this reason the XRD analyses concerned with these topics have been performed using a parallel-beam laboratory diffractometer, equipped with a $\text{CuK}\alpha$ X-ray source, Eulerian cradle, polycapillary collimator, parallel-plate collimator and an energy-dispersive detector (see Figure 1.6). For temperature-dependent *in-situ* X-ray diffraction measurements a commercially available hot stage DHS900 from Anton Paar was mounted on the sample stage of the laboratory diffractometer (for details see chapter 2).

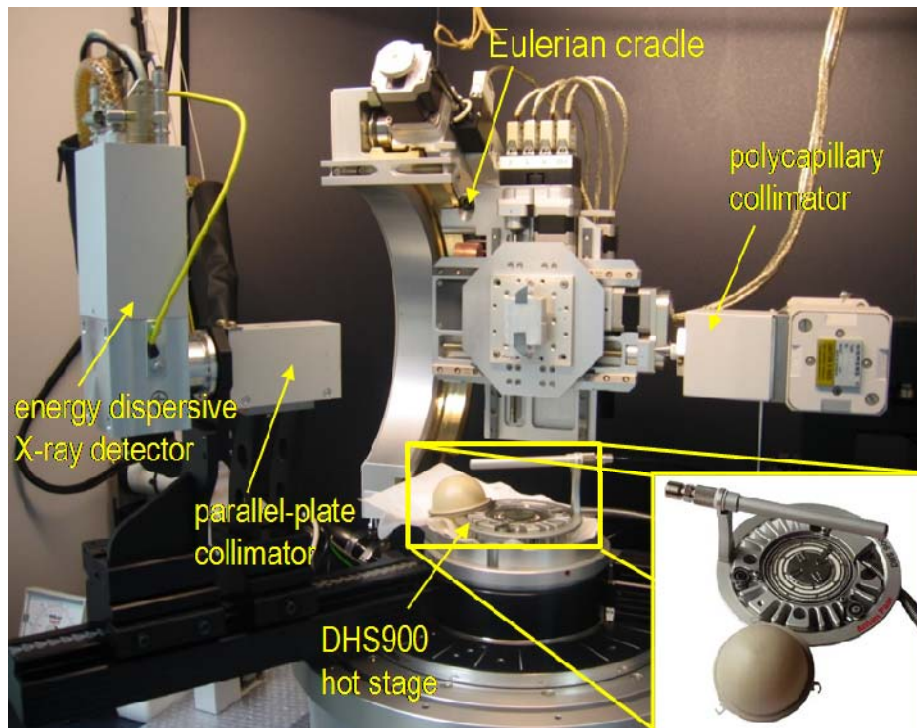


Fig. 1.10. Bruker D8 Discover X-ray diffractometer combined with a hot stage (DHS 900, Anton Paar) to perform in-situ thermal treatment.

1.4.2. Sputter-depth profiling using Auger Electron Spectroscopy

Sputter-depth profiling for investigating elemental concentration as function of the depth from the surface into the layers can be accomplished either by analyzing the sputtered matter (secondary ion mass spectrometry (SIMS), sputtered neutral mass spectrometry (SNMS), and glow discharge optical emission spectroscopy or GDOES) or by analyzing the surface after successive removal of surface layers (Auger electron spectroscopy (AES), X-ray photoelectron spectroscopy (XPS), and ion scattering spectroscopy (ISS)). Among these techniques, AES and SIMS are most frequently used for thin-film chemical analysis in materials science research [84].

The process of AES depth profiling to investigate the concentrations of Ni and Cu of the Ni-Cu thin-film diffusion couple is schematically illustrated in Fig. 1.11.

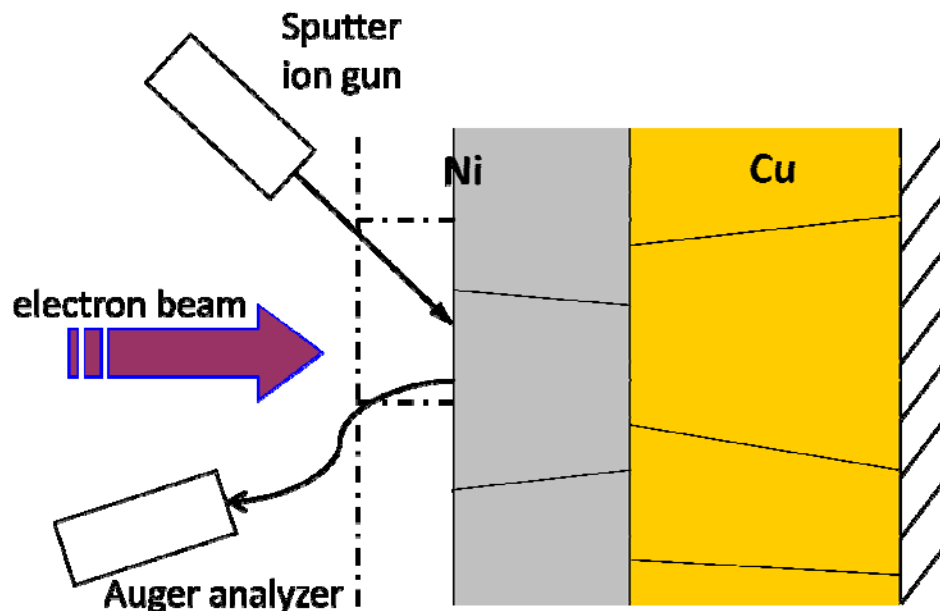


Fig. 1.11. Schematic for investigating the Ni-Cu bilayer diffusion couple using Auger electron spectroscopy (AES) depth profiling.

The Auger effect is named after its discoverer, Pierre Auger (1899-1993), who made a careful study of this effect by observing radiationless relaxation of excited ions in a cloud chamber during the 1920s. Auger electrons are emitted at discrete energies that allow the atom of origin to be identified during the interaction between the primary electron beam and the sample as shown in Fig. 1.12. Since the Auger electrons can only escape from the outer 5-50 Å of a solid surface at their characteristic energy, AES analysis is extremely sensitive and suitable for surface investigation.

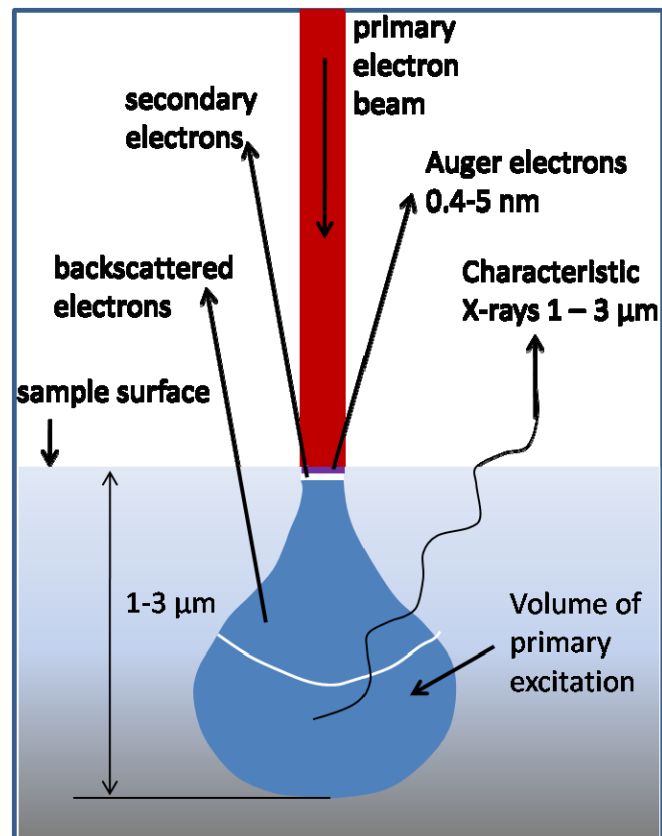


Fig. 1.12. Electrons and X-ray excited during the interaction between the primary electron beam and the sample (redrawn after Ref. [85]).

In this work, the concentration-depth profiles of the Ni-Cu thin-film diffusion couples before and after annealing have been investigated employing a JEOL JAMP 7830F field emission Auger microprobe as shown in Fig. 1.13. The raw data give information of intensity as function of sputter time.

General introduction

Depth profiling is performed by ion bombardment of a selected area of a sample. In order to obtain a quantitative determination of the real concentration-depth distribution, the calibration of the intensity scale (given in counts per second) in units of instantaneous concentration (e.g. at.-%) and of the sputtering time scale in units of depth (the distance from the original surface), and the depth resolution function are to be carried out. Usually these procedures require the investigation of a reference sample [84].

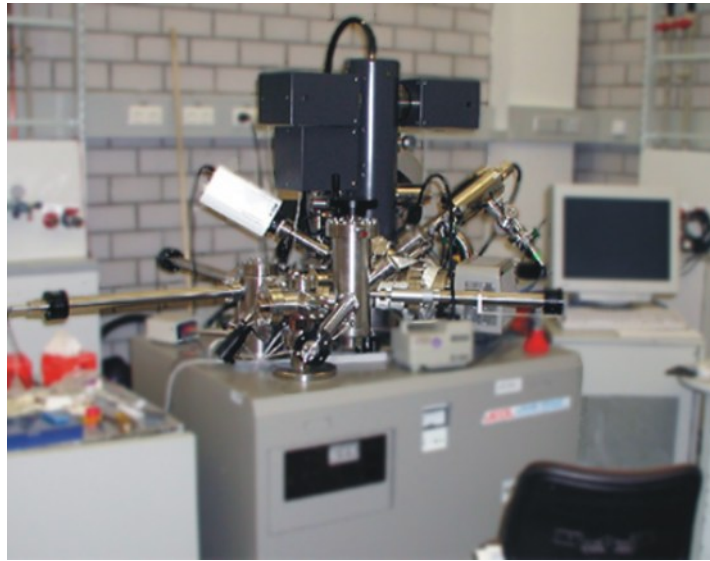


Fig. 1.13. Auger Electron Spectroscopy (AES) with depth profiling using ion sputtering in a JEOL JAMP 7830F field emission Auger microprobe.

1.4.2.1. Sputtering time- depth conversion

The sputtered depth, z , at a time, t , is determined by the instantaneous sputtering rate, $v = dz/dt$, according to [86]:

$$z = \int_0^t v(t) dt \quad (1.2.)$$

The sputtering rate, v , is related to the primary ion current density (flux), j_p , the sputtering yield of material, Y_M , the atomic density, N , and the elementary charge, e by $v = \frac{j_p \cdot Y_M}{N \cdot e}$ [86]. The conversion can be simplified by assuming that the sputtering

rate is constant. Hence, the sputtering depth is directly proportional to the sputtering time, i.e. $z = v \cdot t$.

For a two-component system, the mean sputtering rate can be calculated as

$$\bar{v} = v_A \cdot X_A + v_B \cdot X_B \quad (1.3.)$$

where the mole fractions of element A, X_A , and element B, X_B , satisfy the equation $X_A + X_B = 1$ (for details, cf. Ref. [87]).

1.4.2.2. Intensity-concentration conversion

In general, the matrix effects are limited in AES analysis. The assumption of the existence of a linear relationship between intensity and concentration, therefore, can be made. With this assumption, the conversion of the measured elemental signal intensity into concentration becomes straightforward employing only the sensitivity factors for investigated elements. The sensitivity factors, S , adopted in this work are $S=0.485$ for Ni, $S=0.574$ for Cu, $S=0.137$ for Si, $S=0.158$ for N, and $S=0.371$ for O taking Ag as the reference (i.e., $S_{Ag}=1$).

1.4.2.3. Profile shape considerations: Depth resolution

The shape of the as-measured depth profile is generally distorted with respect to the true concentration-depth profile by various factors such as instrumental factors, ion beam-sample interactions, and sample characteristics. The instrumental factors includes, for example, non-uniform ion beam intensity, impurity and neutrals in the ion beam, adsorption and contamination from the residual gas atmosphere, and resputtering; the ion beam-sample interactions include, for example, primary ion and recoil implantation, induced surface topography, atomic mixing, preferential sputtering, enhanced diffusion and segregation, phase formation, decomposition, charging and electromigration; the sample characteristics include, for example, surface roughness and topography, crystalline structure, defects, second phases, and compounds [86]. As a consequence, the as-measured depth profile of sample with a physically sharp interface always presents a broadened measured sputter-depth profile. In investigations of diffusion in thin films it is therefore important to investigate also

the sputter-depth profile of an as-prepared specimen. This can be taken as a reference for sputter-depth profiles obtained for specimens subjected to diffusion anneals.

1.5. Outline

This thesis is divided in two principal parts: In the first part, the interdiffusion, solid solution formation and stress development in thin-film Ni-Cu diffusion couples are investigated (Chapter 2). It has been found that considerable diffusional intermixing occurred at relatively low annealing temperature. The extent of interdiffusion can be greatly influenced by pre-annealing of the bottom layer (i.e. annealing to reduce the defect density prior to the deposition of the top layer). The influence of interdiffusion on the stress change of sublayers has been analysed quantitatively.

The second part deals with the crystallite-size dependence of the lattice parameter of nanocrystalline metals particularly for nanocrystalline Ni: Both thin films (Chapter 3) and ball-milled powders (Chapter 4) have been investigated. A dedicated annealing procedure called “loop annealing” was devised, which allows a quicker and more precise determination of the correlation between lattice parameter and crystallite size using one single specimen. The lattice contractions of Cu and Pd were confirmed, whereas, for the case of Ni, a non-monotonic change of the lattice parameter with respect to crystallite size was observed for the first time, i.e., both lattice contraction and lattice expansion can occur, depending on the range of crystallite size considered. These results are discussed in the light of different models describing the crystallite-size dependence of the lattice parameters.

References

- [1] Feynman R. There is plenty of room at the bottom. Lecture at the California Institute of technology, 1959.
- [2] Koch CC, Ovid'ko IA, Seal S, Veprek S. Structural Nanocrystalline Materials: Fundamentals and Applications: Cambridge University Press, 2007.
- [3] Rawson P. Ceramics. London, New York: University of Pennsylvania Press, 1984.
- [4] Faraday M. Philos. Trans. R. Soc. London 1857;147:145.
- [5] Kuru Y, Wohlschlägel M, Welzel U, Mittemeijer EJ. Applied Physics Letters 2007;90:243113.
- [6] Chen CQ, Shi Y, Zhang YS, Zhu J, Yan YJ. Phys. Rev. Lett. 2006;96.
- [7] Zhong WH, Sun CQ, Li S. Solid State Commun. 2004;130:603.
- [8] Volkert CA, Lilleodden ET. Philos. Mag. 2006;86:5567.
- [9] Gleiter H. Acta Mater. 2000;48:1.
- [10] Dao M, Lu L, Asaro RJ, De Hosson JTM, Ma E. Acta Mater. 2007;55:4041.
- [11] Meyers MA, Mishra A, Benson DJ. Jom 2006;58:41.
- [12] Kroto HW, Heath JR, O'Brien SC, Curl RF, Smalley RE. Nature 1985;318:162.
- [13] Iijima S. Nature 1991;354:56.
- [14] Alivisatos AP. Science 1996;271:933.
- [15] Hansen N. Deformation of polycrystals: mechanisms and microstructures. Roskilde: Risø National Laboratory, 1981.
- [16] Suryanarayana C. Mechanical alloying and milling New York: CRC Press, 2004.
- [17] Egami T, Billinge SJL. Underneath the Bragg Peaks, Volume 7: Structural Analysis of Complex Materials. New York: Pergamon, 2003.
- [18] Binnig G, Rohrer H. IBM Journal of Research and Development 1986;30:355.
- [19] Hansma PK, Tersoff J. J. Appl. Phys. 1987;61:R1.
- [20] Suryanarayana C, Koch CC. Hyperfine Interact. 2000;130:5.
- [21] Siegel RW. Nanostruct. Mater. 1993;3:1.
- [22] Mutschele T, Kirchheim R. Scr. Metall. 1987;21:1101.
- [23] Suryanarayana C, Mukhopadhyay D, Patankar SN, Froes FH. J. Mater. Res. 1992;7:2114.

General introduction

- [24] Ohring M. The materials science of thin films. San Diego: Academic press, 2002.
- [25] Freund LB, Suresh S. Thin film materials: stress, defect formation, and surface evolution. Cambridge: Cambridge university press, 2006.
- [26] Knez M, Niesch K, Niinisto L. *Advanced Materials* 2007;19:3425.
- [27] Herman H, Sampath S, McCune R. *MRS Bull.* 2000;25:17.
- [28] Movchan BA, Demchish.AV. *Physics of Metals and Metallography-Ussr* 1969;28:83.
- [29] Thornton JA. *Annu. Rev. Mater. Sci.* 1977;7:239.
- [30] Hentzell HTG, Grovenor CRM, Smith DA. *Journal of Vacuum Science & Technology a-Vacuum Surfaces and Films* 1984;2:218.
- [31] Messier R, Giri AP, Roy RA. *Journal of Vacuum Science & Technology a-Vacuum Surfaces and Films* 1984;2:500.
- [32] <http://www.umms.sav.sk/data/files/167.jpg>.
- [33] Meyers MA, Mishra A, Benson DJ. *Progress in Materials Science* 2006;51:427.
- [34] Li L, Man OL. *Mechanical Alloying*. Massachusetts: Kluwer academic publisher, 1998.
- [35] http://www.pauleyequipment.co.uk/UPLOADS/DOCS/e_pulverisette6.pdf.
- [36] Doerner MF, Nix WD. *Crc Critical Reviews in Solid State and Materials Sciences* 1988;14:225.
- [37] Welzel U, Ligot J, Lamparter P, Vermeulen AC, Mittemeijer EJ. *J. Appl. Crystallogr.* 2005;38:1.
- [38] Beke DL, Szabó IA, Erdélyi Z, Opposits G. *Mater. Sci. Eng. A Struct. Mater.* 2004;387:4.
- [39] Opposits G, Szabó S, Beke DL, Guba Z, Szabó IA. *Scripta Materialia* 1998;39:977.
- [40] Shewmon PG. *Diffusion in solids*. Warrendale, Pa.: Minerals, Metals, & Materials Society, 1989.
- [41] Larché FC, Cahn JW. *Acta Metall.* 1985;33:331.
- [42] Welzel U, Lamparter P, Leoni M, Mittemeijer EJ. *Mater. Sci. Forum* 2000;347-349:405.
- [43] Welzel U, Lamparter P, Mittemeijer EJ. *Mater. Res. Soc. Symp. Proc.* 1999;562:147.

- [44] Kuru Y, Wohlschlögel M, Welzel U, Mittemeijer EJ. *Thin Solid Films* 2008;516:7615.
- [45] Chakraborty J, Welzel U, Mittemeijer EJ. *J. Appl. Phys.* 2008;103:113512.
- [46] Nix WD. *Metallurgical Transactions a-Physical Metallurgy and Materials Science* 1989;20:2217.
- [47] Weller H. http://www.chemie.uni-hamburg.de/pc/weller/index_e.html. Hamburg: Institute of Physical Chemistry, University of Hamburg.
- [48] Lu L, Sui ML, Lu K. *Science* 2000;287:1463.
- [49] Mintova S, Olson NH, Valtchev V, Bein T. *Science* 1999;283:958.
- [50] Horch S, Lorensen HT, Helveg S, Laegsgaard E, Stensgaard I, Jacobsen KW, Norskov JK, Besenbacher F. *Nature* 1999;398:134.
- [51] Kneller EF, Luborsky FE. *J. Appl. Phys.* 1963;34:656.
- [52] Hernando A, Marin P, Lopez M, Kulik T, Varga LK, Hadjipanayis G. *Phys. Rev. B* 2004;69.
- [53] Lai SL, Guo JY, Petrova V, Ramanath G, Allen LH. *Physical Review Letters* 1996;77:99.
- [54] Cullity BD, Graham CD. *Introduction to Magnetic Materials: Wiley-IEEE Press*, 2008.
- [55] Gnan J. *Annalen der Physik* 1934;20:361.
- [56] Finch GI, Fordham S. *Proceedings of the Physical Society* 1936;48:85.
- [57] Pickup E. *Nature* 1936;137:1072.
- [58] Boswell FWC. *Proceedings of the Physical Society of London Section A* 1951;64:465.
- [59] Apai G, Hamilton JF, Stohr J, Thompson A. *Phys. Rev. Lett.* 1979;43:165.
- [60] Mays CW, Vermaak JS, Kuhlmann D. *Surf. Sci.* 1968;12:134.
- [61] Yu XF, Liu X, Zhang K, Hu ZQ. *J. Phys.: Condens. Matter* 1999;11:937.
- [62] Chatterjee PP, Pabi SK, Manna I. *J. Appl. Phys.* 1999;86:5912.
- [63] Wang ZM, Wang JY, Jeurgens LPH, Phillip F, Mittemeijer EJ. *Acta Mater.* 2008;56:5047.
- [64] Birringer R, Zimmer P. *Acta Mater.* 2009;57:1703.
- [65] Lamparter P, Mittemeijer EJ. *Int. J. Mat. Res.* 2007;98:485.
- [66] Gamarnik MY. *Physica Status Solidi B-Basic Research* 1991;168:389.
- [67] Okram GS, Devi KN, Sanatombi H, Soni A, Ganesan V, Phase DM. *J. Nanosci. Nanotechno.* 2008;8:4127.

General introduction

- [68] Liu XD, Zhang HY, Lu K, Hu ZQ. *J. Phys.:Condens. Matter* 1994;6:L497.
- [69] Heinemann K, Poppa H. *Surf. Sci.* 1985;156:265.
- [70] Gamarnik MY. *Physica Status Solidi B-Basic Research* 1991;164:107.
- [71] Vermaak JS, Mays CW, Kuhlmann D. *Surf. Sci.* 1968;12:128.
- [72] Lu K, Sui ML. *Scripta Metall. Mater.* 1993;28:1465.
- [73] Lu K, Sun NX. *Philos. Mag. Lett.* 1997;75:389.
- [74] Qin W, Chen ZH, Huang PY, Zhuang YH. *J. Alloys Compd.* 1999;292:230.
- [75] Perebeinos V, Chan SW, Zhang F. *Solid State Commun.* 2002;123:295.
- [76] Mittemeijer EJ, Scardi P. *Diffraction analysis of the microstructure of materials.* Berlin: Springer, 2004.
- [77] Warren BE. *X-ray diffraction.* New York: Addison-Wesley, 1990.
- [78] Cullity BD, Stock SR. Prentice Hall 2001.
- [79] Hauk V. *Structural and residual stress analysis by nondestructive methods.* Amsterdam: Elsevier 1997.
- [80] Willemsse PF, Naughton BP, Verbraak CA. *Materials Science and Engineering* 1982;56:25.
- [81] Mittemeijer EJ, Welzel U. *Z. Kristall.* 2008;223:552.
- [82] Klug HP, Alexander LE. John Wiley and Sons, New York 1974:643.
- [83] Jiang HG, Ruhle M, Lavernia EJ. *Journal of Materials Research* 1999;14:549.
- [84] Hofmann S. *Surface and Interface Analysis* 2003;35:556.
- [85] Physical-Electronics. <http://www.phis.com/surface-analysis-techniques/aes.html>.
- [86] Hofmann S. *Progress in Surface Science* 1991;36:35.
- [87] Hofmann S. *Surface and Interface Analysis*|*Surface and Interface Analysis* 1980;2:148.

2. Interdiffusion, solid solution formation and decomposition and stress development in thin-film Ni-Cu diffusion couples

J. Sheng, U. Welzel, E. J. Mittemeijer

Abstract

Thin film Ni-Cu diffusion couples (individual layer thicknesses: 50 nm) were prepared by direct-current magnetron sputtering on silicon substrates. Interdiffusion and solid-solution formation, the associated changes of microstructure and the evolution of mechanical stresses of the Ni-Cu diffusion couples during thermal treatments were investigated employing *ex-situ* X-ray diffraction phase and texture measurements and *in-situ* X-ray diffraction stress measurements, transmission electron microscopy and Auger-electron spectroscopy (sputter) depth-profiling. Annealing at relatively low temperatures (about $0.4 T_m$) results in considerable diffusional intermixing, which is accompanied by the formation of the (Cu,Ni) solid solution. In addition to thermal stresses, tensile stress contributions arise in the sublayers during the diffusion anneals, which diffusion-induced stress contributions were identified by comparing the measured stress changes of the sublayers in the bilayer with those recorded from single layers of Cu and Ni annealed under identical conditions. The diffusion-induced stress changes of the sublayers could be quantitatively evaluated considering the measured concentration-depth profiles of the annealed Ni-Cu diffusion couples and were discussed in terms of possible mechanisms of stress generation. The dominant sources of stress buildup and relaxation were identified.

2.1. Introduction

Mechanical stresses in thin films are of paramount importance for the reliability and performance of technological applications (e.g. micro-electronic). These stresses can be due to the deposition process (intrinsic stresses), to a mismatch of the coefficients of thermal expansion of the film(s) and the substrate upon cooling or heating (extrinsic, thermal stresses) or can arise due to thermally activated processes as annihilation of crystal defects, grain growth, diffusion and/or phase transformations (e.g. Refs. [1-2] and references therein). Interdiffusion and phase transformation can occur pronouncedly in thin films at much lower homologous temperatures than as observed for bulk diffusion couples due to the presence of a high density of defects and grain boundaries [3-6], which thereby can bring about great changes of the state of stress already at comparatively low annealing temperatures.

For the case of substitutional diffusion, as pertains to this work, interdiffusion is a source of stress generation if the partial molar volumes of the components are not identical and/or if the diffusion fluxes of the diffusing species differ, i.e. if a net vacancy flux occurs (cf. the Kirkendall effect) [7-9].

The diffusion-induced, changing stress state, in turn, can affect the diffusion process. The influence of stress on diffusion is well known for the case of a hydrostatic state of stress: the diffusivity is influenced via the so-called activation volume. [10] The case of a non-hydrostatic stress state, however, has received only limited attention both theoretically and, in particular, experimentally. Pioneering theoretical work in this field is due to Cahn and Larché [11]. In this context, the so-called diffusion potential was introduced and on that basis stress gradients can be described as driving forces for diffusion.

Experimental investigations of the stress evolution during thermal treatments of thin film diffusion couples are cumbersome: As the state of stress of each phase/component is to be determined separately, the substrate curvature method [1, 12] often employed for the measurement of stresses in thin films cannot be used. Only (X-ray) diffraction-stress measurements permit the determination of the stresses of the phases/components individually [13]. Moreover, usually more than one mechanism influencing the stress state is operative: As an example, interdiffusion in a layered structure is often accompanied by the annihilation of crystal defects and by grain

growth, which by themselves can lead to pronounced tensile stress development (e.g. see Ref. [14]. Above all, plastic accommodation of strains may occur if the local yield limit is exceeded [3].

A possible way to identify stress changes occurring in a layered system upon annealing, due to processes other than interdiffusion, is to also perform experiments with single layers, of the components (sublayers) of the layered system investigated, produced under conditions identical to those employed for the sublayers of the layered system. Changes of residual stresses due to diffusion (and reactions) between the sublayers in the layered structure can then be identified (i.e. separated) by comparing the stress evolutions upon annealing of the single layers with those recorded for the sublayers in the layered system.

In spite of its scientific importance and technological urgency, systematic investigations of the interrelation of interdiffusion and residual (internal) stresses in thin film are rare [3, 5, 15-17]. The Cu-Ni system investigated in this work exhibits miscibility at all compositions above about 350°C and absence of intermediate or ordered phases in Ni-Cu alloys (at about 1 atm); a miscibility gap occurs below about 350°C [18]. The interdiffusion and stress evolution in thin bi-layer (individual layer thickness: 50 nm) diffusion couples of Cu and Ni have been investigated employing ex-situ and *in-situ* X-ray diffraction measurements (XRD) and Auger-electron spectroscopy in combination with sputter-depth profiling (AES). Microstructural analysis has been performed employing transmission electron microscopy (TEM). In addition, single layers of Ni and Cu have been investigated. The (XRD) individual specific residual stress contributions that emerge due to only the diffusion between the (sub)layers in the bilayer then have been determined by comparing the stress changes occurring in the sublayers of the bilayer system with corresponding results obtained for the single layers of the components in the bilayer system. As a result, diffusion-induced stress generating and relaxing mechanisms have been identified.

2.2. Experimental details

2.2.1. Preparation of bilayers, single layers and alloy layers

The substrate used in this work consists of a Si (100) wafer (500 μm thick) covered with a SiO_2 (50 nm thick) layer on top of a Si_3N_4 (50 nm thick) layer. The amorphous SiO_2 and Si_3N_4 layers act as diffusion-barrier layers. Polycrystalline thin-film Ni-Cu bilayers were prepared by successive deposition of Cu and Ni on to the substrate by DC magnetron sputtering in a sputter chamber with a base pressure of 5×10^{-8} mbar. Prior to deposition, the substrates were sputter-cleaned for about 1 min. by irradiation with Ar^+ ions accelerated with a voltage of -105 V. During the film deposition, the chamber pressure was maintained at 1.4×10^{-4} mbar using pre-cleaned Ar (employing a Messer Oxisorb gas cleaning cartridge) as a sputter gas and the substrates were rotated around their surface normal at about 12 rpm. The Cu and Ni targets were operated at 200 W. The purities of the target metals of Cu and Ni are 99.999 wt% and 99.99 wt%, respectively. The Ni and Cu sublayers each had a thickness of 50 nm. The film thickness was determined by calibration of the deposition rate using a stylus profilometer. For this purpose a sample with a step in height was produced. During deposition, the substrate temperature increased slightly due to the atomic bombardment, but did not exceed 40°C . The Ni-Cu bilayers thus prepared are denoted by “normally deposited” (ND).

To decrease the defect density in the Cu bottom sublayer, a pre-annealing treatment was applied to some of the specimens: in that case the Cu sublayer was annealed at 500°C for 3 hours and cooled back to 30°C after its deposition without breaking the vacuum. The state of such a Cu sublayer is called “pre-annealed (PA) condition” in the following. Thereafter, the Ni layer was deposited.

For investigating the *de*-mixing tendency of a Cu-Ni alloy at low temperatures in the region of the miscibility gap (i.e. $T < 350^\circ\text{C}$; cf. Section 2.1), a Cu-Ni alloy layer with a composition of 57 at% Ni was prepared by co-sputtering from pure Cu and Ni targets. The composition was adjusted by controlling the magnetron power and checked by both X-ray diffraction measurements and X-ray photoelectron spectroscopy (XPS). The alloy layers were *ex-situ* annealed after encapsulation in quartz ampoules, initially evacuated to a pressure of 1×10^{-6} mbar and subsequently

filled with Ar gas in order to avoid oxidation, at 300°C for 30 days in a salt-bath and subsequently air cooled.

2.2.2. Microstructure investigation

The cross-sectional microstructure of both as-deposited and annealed Cu-Ni thin-film diffusion couples was investigated using a Philips CM200 transmission electron microscope (TEM) operating with a 200 kV electron beam. The TEM samples were prepared by cutting two pieces off the bilayer/substrate specimens and sandwiching these pieces (bilayers of both pieces facing each other) with epoxy glue. After subsequent mechanical thinning by grinding, the resulting thin slice of material was embedded with the bilayers parallel to the cylinder axis into a specially designed cylindrical polycrystalline Al₂O₃ tube of 3 mm diameter as a holder for the cross-sectional sample. Then, the tube was cut into slices with a thickness about 350 μm. The slices underwent mechanical grinding, dimpling from both sides, and, finally, ion thinning (Ar⁺ ions with 3.5 keV energy and 1 mA ion current in a BAL-TEC RES 010 apparatus with liquid nitrogen cooling) for several hours to achieve electron transparency. Details of the cross-sectional specimen preparation can be found elsewhere [19].

2.2.3. Concentration-depth profiling

Concentration-depth profiles were obtained by using ion sputtering combined with Auger Electron Spectroscopy (AES) in a JEOL JAMP 7830F field emission Auger microprobe. Auger lines of Cu at 842 eV and at 920 eV and Ni at 848 eV were used for the determination of concentration profiles. The analysis of the Auger spectra of the Cu/Ni system is complicated by the overlapping of the Cu and Ni Auger signals: the strongest Ni Auger peak at 848 eV overlaps with the second strongest Auger peak of Cu at 842 eV. Target factor analysis (TFA) function of the PHI MultiPak Software has been successfully employed to extract the Ni spectrum from the overlapped composite spectra by importing experimentally obtained reference spectra of pure Cu and pure Ni.

The atomic concentration of C_i (i=Cu, Ni, Si, N) was calculated using the following relationship:

$$C_i = \frac{\frac{I_i}{S_i}}{\frac{I_{Cu}}{S_{Cu}} + \frac{I_{Ni}}{S_{Ni}} + \frac{I_{Si}}{S_{Si}} + \frac{I_N}{S_N}} \quad (i = \text{Cu, Ni, Si, N}) \quad (2.1.)$$

where I_i ($i = \text{Cu, Ni, Si, N}$) denotes the peak-to-peak height of the Auger peaks in the differentiated spectrum, and S_i ($i = \text{Cu, Ni, Si, N}$) is the relative Auger yield of Cu, Ni, Si, and N, respectively, with respect to pure Ag. In this work, the values of S_i are measured as 0.574, 0.485, 0.137, and 0.158 for Cu, Ni, Si, and N, respectively.

Sputter time can be converted into sputter depth if the sputter rate is known. To determine the sputter rates of Cu, Ni, and Si_3N_4 , both Cu and Ni single layers and as-deposited Cu-Ni bilayers (all with a Si_3N_4 layer underneath; cf. Section 2.2.1) were measured by Auger depth-profiling.

After correcting the measured profiles by the target factor analysis indicated above, the sputter rates of Cu, Ni, and Si_3N_4 could be determined by dividing the thickness of the total removed layer by sputter time. The thus resulting values for the sputter rates in the current experiments of Cu, Ni, and Si_3N_4 are 6.5 nm/min, 4.6 nm/min, and 5.7 nm/min, respectively. However, the sputter rate can change with changing composition in a binary system when interdiffusion takes place. In order to evaluate the sputter rate of the Ni–Cu binary system a kinetic sputter model has been applied [20]. In order to avoid errors related to possible changes of the sputter rate for different specimens, the sputter rate was re-calibrated individually for each specimen. For the temperature range investigated, the Si_3N_4 (top) layer on the substrate can be considered as a diffusion barrier. A calibration of the sputter rate thus can also be realized by calibrating the sputter rate such that a concentration of 50 at.% Cu (the Cu sublayer is the bottom layer) is identified with the (sputter) depth corresponding to the interface with the Si_3N_4 layer of the substrate.

It should be noted that the concentration–depth profiles obtained by AES in combination with ion sputtering give information on the overall (laterally averaged) interdiffusional behaviors of the diffusing species. Information about the intrinsic diffusional fluxes of the Cu and Ni atoms can only be acquired by marker experiments which are extremely difficult (if not impossible) to conduct for thin-film diffusion couples as employed in this study.

2.2.4. Phase and texture analysis and macrostress evaluation

For *ex-situ* X-ray diffraction phase analysis and texture measurements and *in-situ* temperature-dependent X-ray diffraction stress measurements, a Bruker D8 Discover diffractometer operating in parallel-beam geometry was used. The diffractometer was equipped with a copper X-ray tube operated at 40 kV and 30 mA, an X-ray lens in the primary beam and a parallel-plate collimator in the diffracted beam. The energy-dispersive detector (Bruker Sol-X) was set to $\text{CuK}\alpha$ radiation. A domed hot stage DHS900 (Anton Paar) apparatus was mounted onto the Eulerian cradle and calibrated [21]. With this equipment, it is possible to perform *in-situ* experiments within a temperature range from room temperature to 700°C and to 900°C under vacuum (5×10^{-3} mbar) and protective ($\text{N}_2 + \text{H}_2$) gas flow, respectively.

The specimens were heated and cooled in steps of 25°C. A heating rate of 0.1 K/s was used and a waiting time of 5 minutes was adopted upon arriving at the temperature of each temperature step to guarantee temperature homogenization. Since both the Ni and the Cu sublayers were strongly {111}-fiber textured, the residual (internal) stresses were determined employing the crystallite group method (CGM) using the Cu and Ni 111 reflections (see Ref. [13]; see also below). Each stress measurement comprising scans of the diffraction angle at two tilt angles ($\psi = 0^\circ$ and $\psi = 70.53^\circ$, where ψ , the specimen-tilt angle, indicates the inclination of the diffraction vector with respect to the specimen-surface normal), took only about 25 min during which the specimen did not undergo pronounced microstructural change (as was verified by separate experiments).

For investigating the formation and decomposition of the (Cu,Ni) solid solution, high-resolution powder diffraction patterns were measured employing $\text{CuK}\alpha_1$ radiation using a Panalytical X'Pert MPD Bragg-Brentano diffractometer equipped with a Cu X-ray tube, a monochromator to select $\text{CuK}\alpha_1$ radiation in the primary beam, and a position sensitive detector (Panalytical X'Pert Accelerator).

The software 'ProFit' (Panalytical) was used to determine peak maximum positions, full widths at half maximum (FWHM), integral breadths and integrated intensities by fitting Pseudo-Voigt functions to measured diffraction lines [22].

For the analysis of mechanical stress the interplanar spacing, d_{ψ}^{hkl} , at each specimen-tilt angle, ψ , was calculated from the corresponding position of the hkl diffraction-line maximum, determined by peak fitting (see above) using Bragg's law. In the present work, the 111 reflections were used for stress analysis for both the Cu (-rich) phase and the Ni (-rich) phase. Due to (i) the in-plane rotational symmetry of the biaxial state of stress in the Cu and Ni sublayers (measurements at rotation angles $\varphi=0^{\circ}$ and $\varphi=90^{\circ}$ with respect to the specimen normal yielded the same stress values) and (ii) the presence of a pronounced $\{111\}$ fibre texture (cf. Section 2.3.1), the fibre-texture crystallite group method (CGM) was employed [23]. In this limit, single crystal elastic compliances (values taken from Ref. [24]) can be used in the diffraction stress evaluation instead of the diffraction stress factors (for details, see Refs. [13, 25-26]; for limitations in the application of the CGM in the case of fibre texture, see Ref. [26]).

The measured diffraction profile $h(x)$ can be conceived as the convolution of the only structurally broadened profile $f(x)$ with the instrumentally broadened profile $g(x)$: $h(x) = f(x) \otimes g(x)$. The instrumental broadening expresses the broadening effects owing to all instrumental aberrations, as slit widths, etc. The structural line broadening originates from crystalline imperfections, as finite, small crystallite size and the microstrain due to dislocations, misfitting precipitates etc. Both theory and experiment support that in many cases, the structurally broadened and the instrumentally broadened profiles can well be approximated by Voigt functions (a Voigt function is the convolution of a Cauchy (Lorentz) function and a Gauss function). In this case, the integral breadths of the Gauss- and Cauchy components of the structurally broadened profiles, $\beta_{f,g}$ and $\beta_{f,c}$, respectively, can be obtained from the integral breadths (β_h) and the Voigt parameters (i.e., the ratio of the FWHM to the integral breadth) of the measured profiles (h) employing the so-called Voigt-method [27-30]. To this end, the integral breadths (β_g) and the Voigt parameters of the instrumentally broadened profiles (g) have to be known as well. In order to determine the instrumentally broadened profile of the diffractometer as function of diffraction angle 2θ , 13 hkl reflections of a LaB_6 (NIST SRM660a) standard powder sample were measured. The integral breadths and the Voigt parameters at the diffraction angles of the Cu and Ni 111 reflections were then obtained by interpolation.

Assuming that the Cauchy component of the structurally broadened profile is due to the small crystallite size and that the Gauss component of the structurally broadened profile is due to microstrain, the crystallite size, D , and the microstrain, e , can be obtained from [29-30]:

$$\beta_{f,c} = \frac{\lambda}{D \cos \theta_0} \quad (2.2.)$$

$$\beta_{f,g} = 4e \tan \theta_0 \quad (2.3.)$$

where the size value, D , is the volume-weighted domain size in the direction parallel to the diffraction vector, λ is the wavelength and θ_0 is the position of the diffraction-line maximum. The value of e in Eq. (2.3.) is a measure for the microstrain (variation) in the specimen. For the case of a Gaussian strain distribution it is possible to calculate the local r.m.s. strain $\langle \varepsilon_0^2 \rangle^{1/2}$ from e : $\langle \varepsilon_0^2 \rangle^{1/2} = (2\pi)^{1/2} e$ [29].

This single-line method of diffraction-line broadening analysis is very useful to acquire a general understanding of origins of line broadening and to obtain estimates for crystallite size and microstrain and, in particular, to observe the evolution of their values *in-situ* as functions of temperature and/or time. More sophisticated and more detailed methods for the analysis of diffraction-line broadening exist (see, for example, Ref. [31]), but such analyses require much more measurement time (e.g. a second, weak order of the reflection has to be measured) which damages unacceptably the time resolution necessary for an *in-situ* investigation as performed here.

2.3. Results and discussion

2.3.1. Microstructure

Cross-sectional (bright field) transmission electron microscopy images of the “normally deposited” (ND) and “pre-annealed” (PA) Ni-Cu diffusion couples in the as-prepared condition (cf. Section 2.2.1) and after annealing at 300°C are shown in Figs. 2.1 and 2.2, respectively. Inspection of a number of such micrographs showed that a columnar microstructure (columns traversing the entire sublayer) prevails in both sublayers, with a somewhat more irregular microstructure in some portions of the Cu sublayer. The interface of the sublayers is clearly visible even after annealing. For

the Ni and Cu sublayers of the ND bilayer (Fig. 2.1a) and the Ni layer of the PA bilayer (Fig. 2.1b), a high density of crystal defects is revealed by the pronounced contrast variation within the grains. Evidently, the pre-annealing of the bottom Cu layer has reduced appreciably the crystalline imperfections (see Fig. 2.1b). The in-plane, lateral grain sizes of the layers are around 30 nm for the Ni and Cu sublayers, except for the case of the pre-annealed Cu sublayer, which exhibits a lateral grain size of about 80 nm.

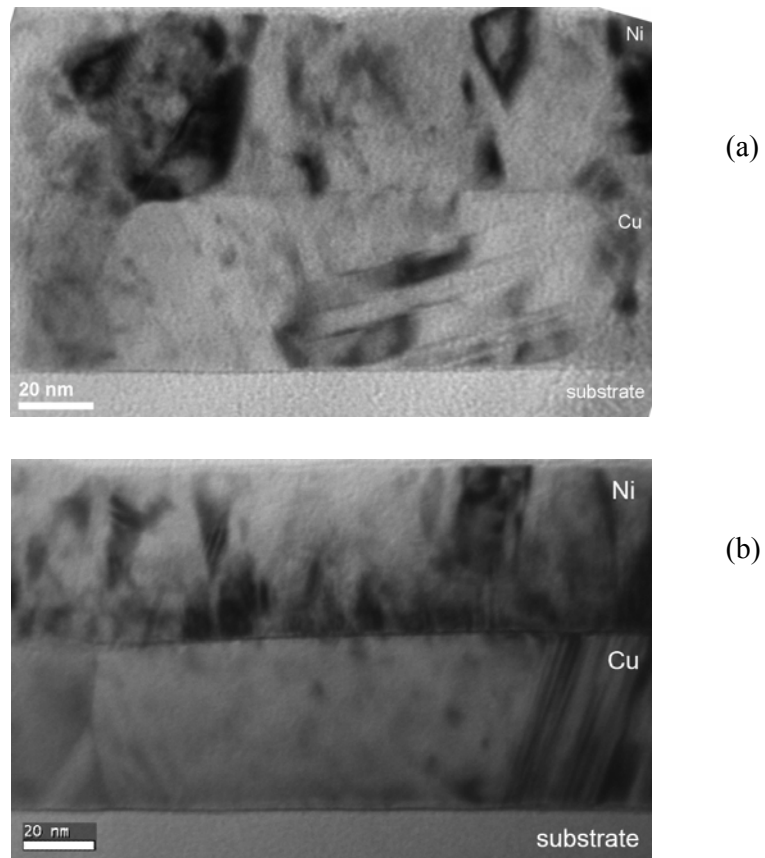


Fig. 2.1. Cross-sectional TEM images (bright field) of the as-deposited Ni-Cu bilayers, (a) normally deposited (ND) and (b) pre-annealed (PA). The pre-annealing was performed for only the bottom Cu sublayer (3 h at 500°C) before deposition of the Ni sublayer.

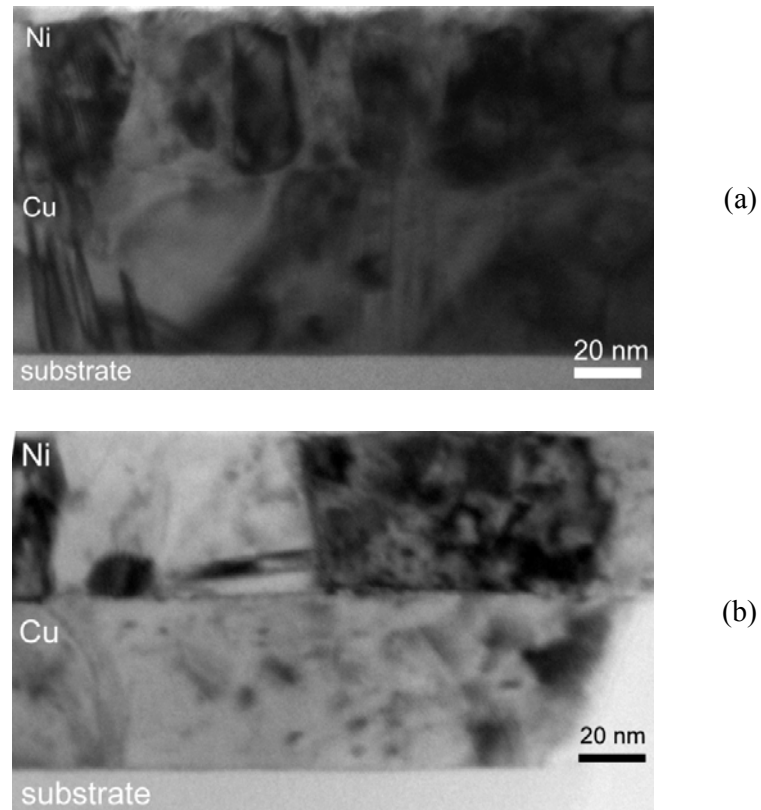


Fig. 2.2. Cross-sectional TEM images (bright field) of the Ni-Cu bilayers *in-situ* annealed at 300° C for 10 hours, (a) normally deposited (ND) and (b) pre-annealed (PA). The pre-annealing was performed for only the bottom Cu sublayer (3 h at 500° C) before deposition of the Ni sublayer.

Upon heating up and annealing grain growth occurs in the Ni and Cu sublayers of the ND specimen and in the Ni sublayer of the PA specimen, whereas this is not the case for the pre-annealed Cu sublayer (cf. Figs. 2.1 and 2.2). Although some equiaxed grains are present, most of the grains in all sublayers still exhibit a columnar morphology also after *in-situ* annealing at 300°C for 10 hours.

The normalized (with respect to the maximum at $\psi=0^\circ$) 111 pole figure sections (integrated intensity of the 111 reflections plotted versus ψ) of both sublayers of the ND and PA bilayers before and after annealing are shown in Fig. 2.3. The Cu and Ni sublayers exhibit relatively strong {111} fibre textures in the as-deposited state

and (even more) after annealing. The annealing of the bilayers led to a relatively pronounced change of the strength and sharpness of the $\{111\}$ fibre texture of, in particular, the Ni sublayer of the PA specimens (see dash-dot line in Fig. 2.3b). Apparently the coarse-grained nature of the pre-annealed Cu bottom layer of these PA specimens (see above discussed TEM graphs, and results shown in Table 2.1 discussed below) allowed a relatively pronounced (lateral) growth of these grains in the Ni sublayer with $\{111\}$ planes parallel to the surface. The pre-annealing of the bottom Cu layer induces the $\{111\}$ fibre texture being strongest and most sharp for this sublayer (see dotted line in Fig. 2.3a).

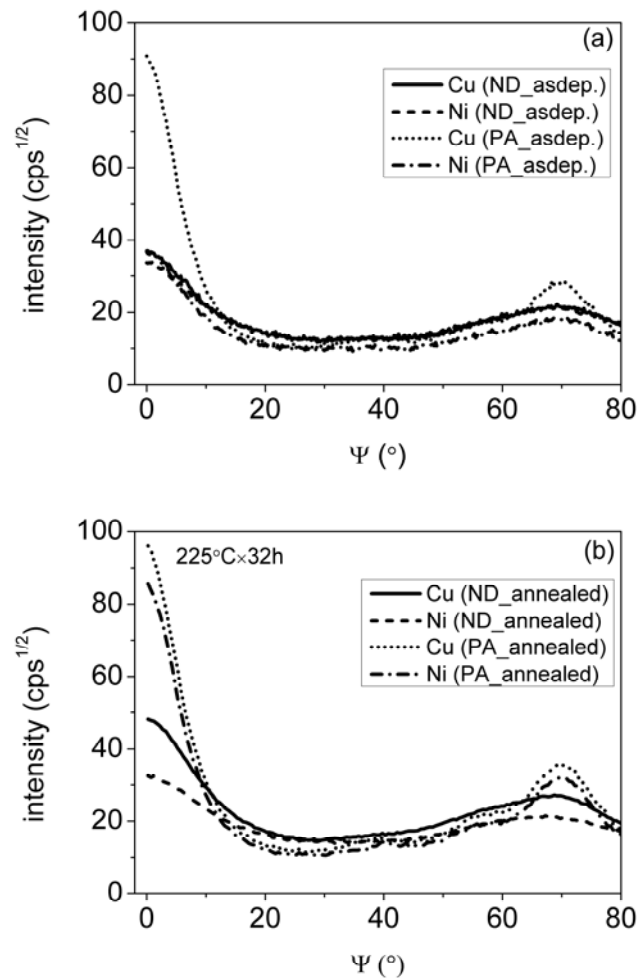


Fig. 2.3. $\{111\}$ pole figure sections (a) for as-deposited ND and PA Ni-Cu bilayers, and (b) for the ND and PA Ni-Cu bilayers after annealing at 225° C for 32 hours.

Table 2.1. The crystallite sizes, D , and the microstrains, e , of the Ni and Cu sublayers of the normally deposited (ND) and the pre-annealed (PA) Ni-Cu diffusion couples at the tilting angle, ψ , at 0° and 70.5° , respectively.

ψ ($^\circ$)	normally deposited (ND)				pre-annealed (PA)			
	Ni		Cu		Ni		Cu	
	D (nm)	e (%)	D (nm)	e (%)	D (nm)	e (%)	D (nm)	e (%)
0	20	0.05	25	0.05	42	0.12	50	0.12
70.5	15	0.20	20	0.15	25	0.15	80	0.10

The rotational symmetry of the texture with respect to the specimen normal was confirmed by measurements at different angles of rotation with respect to the specimen normal, ϕ . The intensity maxima at $\psi=0^\circ$ and $\psi\approx 70^\circ$ correspond to the ideal orientations of the $\{111\}$ fibre texture crystallite group. These results justify employing the CGM for the residual stress analysis of as-deposited and heat treated samples (see results in Section 2.3.4).

The results of the single-line analysis (cf. Section 2.2.4) of the as-prepared ND and PA Ni-Cu diffusion couples have been gathered in Table 2.1 for two inclinations of the diffraction vector with respect to the surface normal ψ : $\psi = 0^\circ$ and $\psi = 70.5^\circ$. The crystallite sizes obtained from line-broadening analysis are well compatible with the results of the transmission electron microscopy investigations: Whereas the Ni and Cu sublayers of bilayers of type ND exhibit crystallite sizes of 20 nm to 30 nm, the pre-annealed Cu sublayer of the PA bilayer exhibits an in-plane crystallite size of about 80 nm. The results reveal also an increase of the crystallite size of the Ni sublayer of the PA bilayer as compared to the Ni sublayer of the ND bilayer, which is ascribed to the growth of the Ni layer occurring onto a coarse-grained pre-annealed bottom Cu layer.

The microstrain is a measure for the (variation of the) (local) lattice strains of the diffracting planes, which originate from microstresses caused by structural imperfections. The considerable value of the microstrains, of the order of 0.1 %, present in all sublayers is compatible with a high density of crystal defects as dislocations etc.

2.3.2. Diffusional intermixing

The concentration-depth profiles of Ni for the normally deposited (ND) and pre-annealed (PA) Ni-Cu diffusion couples annealed for 32 hours at temperatures of 225°C and 300°C are shown in Figs. 2.4a and 2.4b.

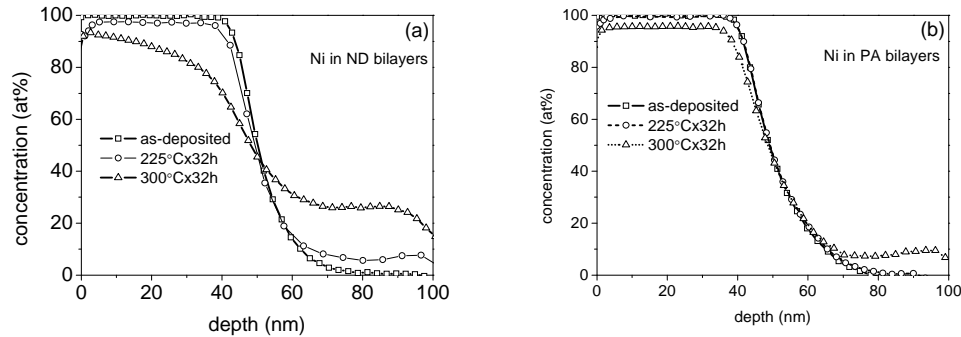


Fig. 2.4. Nickel concentration-depth profiles of (a) normally deposited(ND) and (b) pre-annealed(PA) Ni(top)-Cu(bottom) bilayer diffusion couples after isothermal annealing for 32 h at temperatures of 225°C and 300°C and as-measured for the as-prepared condition.

The sputter–depth profile of the as-deposited sample does not show a truly sharp interface. The diffuseness of the interface is due to: (i) the intrinsic roughness of the interface and (ii) the smearing of the true concentration–depth profile due to instrumental effects during AES depth profiling (cf. Ref. [32] and references therein). The occurrence of appreciable diffusional intermixing in the unannealed diffusion couple is unlikely as all depositions have been performed at temperatures $T < 40$ °C.

After annealing a ND diffusion couple at 225°C for 32 hours, the concentration-depth profile shows a change (reduction of the absolute value) of the slope at the position of the initial interface and the emergence of a plateau region of considerable Ni concentration at the depth range of the in the initially pure Cu sublayer (Fig. 2.4a). The height of this Ni plateau in the Cu sublayer of the ND specimen increases significantly when the annealing temperature increases from 225°C to 300°C. Whereas the change of the slope at the position of the initial interface is due to the volume diffusion across the initial interface, the plateau region on the Cu-rich side of the Ni couple is the result of Ni diffusion through Cu grain

boundaries, oriented more or less perpendicularly to the original interface (columnar grains, cf. Section 2.3.1), accompanied with sideways Ni volume diffusion from the Cu grain boundaries in to the Cu grains. On the initially Ni-rich side of the couple, a Cu plateau development is much less distinct. This implies that sideways Cu diffusion from the Ni grain boundaries through the columnar Ni grains is limited. Recognizing that the grain-boundary density in the Ni sublayers is about equal to (ND specimens) or even higher (PA specimens) than in the Cu sublayers. This is likely a consequence of the concentration-dependence of the interdiffusion coefficient in the Cu/Ni system: the interdiffusion coefficient is pronouncedly smaller at high Ni concentration (see, for example, Ref. [33-34]).

The extent of diffusional intermixing at a given annealing condition is much less pronounced for the pre-annealed (PA) diffusion couple: cf. Figs. 2.4a and 2.4b. The concentration slope at the position of the initial interface changes only slightly even after annealing at a relatively high temperature of 300°C. This is a consequence of very limited volume diffusion across the initial interface due to a reduced density of crystalline defects accelerating volume diffusion (as compared to the ND specimens). The plateau concentrations of Ni and Cu in the initially pure Cu and Ni sublayers, respectively, are significantly lower for the PA diffusion couples as compared to the ND diffusion couples. This effect is a direct consequence of the drastically reduced grain-boundary density in the PA Cu layer as compared to the ND Cu layer: see the in-plane crystallite sizes determined by line-broadening analysis (at $\psi = 70.53^\circ$) presented in Table 2.1.

A significant Cu concentration occurs at the surface of the bilayer specimen, at a stage of annealing where the Cu concentration in the plateau region of the Ni layer is still small. At sufficiently low temperature the contribution of volume diffusion becomes insignificant. Then, the Cu atoms, originating from the bottom layer, propagate along columnar grain boundaries of the Ni layer and reach the free surface (or a layer/substrate interface) and accumulate there without that a pronounced plateau develops in the concentration–depth profile of the layer.

2.3.3. Formation and decomposition of the (Cu, Ni) solid solution

According to the binary phase-diagram of the Cu-Ni system (at about 1 atm), no intermetallic or ordered phases occur, but a miscibility gap exists below about 350°C [18]. X-ray diffraction patterns of the as-deposited Ni-Cu diffusion couples only show reflections of pure Cu and pure Ni.

Annealing the couple at 225°C does not result in pronounced changes of the diffraction patterns (apart from minor peak shifts in particular due to stress changes; see Section 2.3.4). This can be understood recognizing that diffusional intermixing is very limited at this annealing temperature (see results shown and discussed in Section 2.3.2).

The diffraction patterns corresponding to the diffraction-angle ranges of the Cu and Ni 111 reflections of both ND and PA specimens annealed at 300°C for different durations are shown in Figs. 2.5a and 2.5b, respectively. A shoulder had developed after annealing for 4 hours at 300°C at the high-angle side of the Cu 111 reflection, for the ND specimen, indicating the development of a Cu-rich volume fraction of the diffusion couple, at the cost of pure Cu, which shoulder increases in intensity upon continued annealing (Fig. 2.5a). This result is compatible with the development of a pronounced Ni plateau in the originally pure Cu layer (cf. Fig. 2.4a). For the same annealing temperature, and at even a much longer annealing duration, only a small hump had developed at the high-angle side of the Cu 111 reflection for the PA specimen (Fig. 2.5b), which agrees with the concentration-depth profile shown in Fig. 2.4b, as compared to Fig. 2.4a (the much lower grain boundary density in the pre-annealed Cu sublayer allows much less sideways diffusion of Ni; cf. Section 2.3.1).

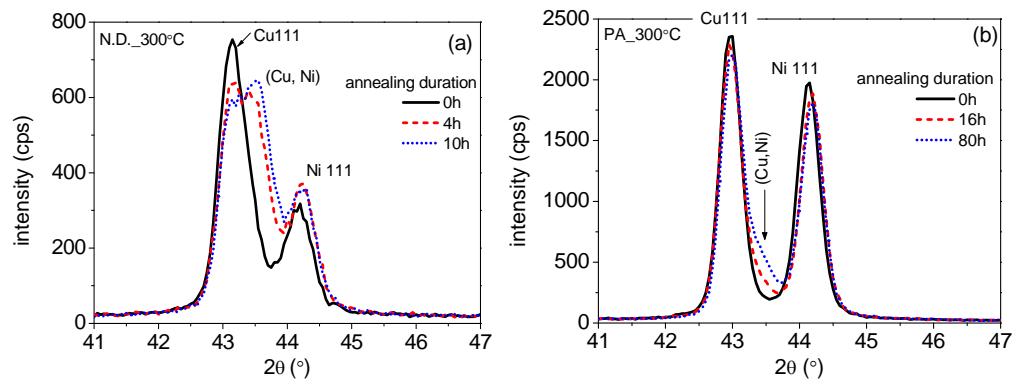


Fig. 2.5. Diffraction patterns (recorded in-situ) of the Ni-Cu thin films upon diffusion annealing at 300°C (in the diffraction range of the 111 reflections of Cu and Ni): (a) normally deposited (ND) and (b) pre-annealed (PA) Ni/Cu bilayers.

Continued annealing of the ND specimen results in the emergence of a separate intensity maximum at the high-angle side of the Cu 111 reflection (see, in particular, the high-resolution powder diffraction pattern in Fig. 2.6), which indicates that most of the originally pure Cu layer has become a Cu-rich solid solution containing a substantial amount of Ni (cf. Fig. 2.4a). According to Vegard's law, the composition of the formed (Cu,Ni) solid solution could be evaluated (using the lattice constant obtained from the (Cu,Ni) 111 reflection determined by interpolation for the strain-free direction in a plot of the lattice plane spacing versus $\sin^2 \psi$) [35]. Thus it is obtained for 80 h annealing at 300°C: 29.5 at.% Ni. This composition of the (Cu,Ni) solid solution is close to but outside the miscibility gap. It can therefore be suggested that the existence of the miscibility gap limits the maximum Ni concentration in the Cu-rich solid solution developing below the critical temperature in Ni-Cu thin-film diffusion couples.

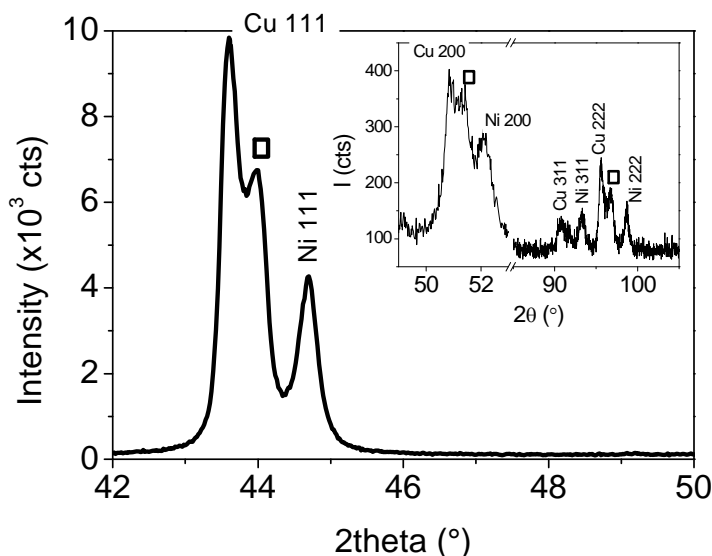


Fig. 2.6. High-resolution powder diffraction pattern of the normally deposited (ND) diffusion couple after annealing at 300°C for 80 h. The pattern was recorded at room temperature using $\text{CuK}\alpha_1$ radiation, “□” denotes the 111 and 200 (inset) and 222 (inset) reflections of the (Cu,Ni) solid solution.

For investigating if a homogeneous Ni-Cu alloy with a composition in the miscibility gap decomposes upon annealing at 300°C in Ni-rich and Cu-rich solid solutions, a (Cu,Ni) alloy layer with a composition of 57 at.% Ni was prepared by co-deposition (cf. Section 2.3.1). The X-ray diffraction measurement of the unannealed alloy revealed that a single-phase alloy layer was obtained. The specimen was encapsulated and *ex-situ* annealed in a salt-bath at a temperature of 300°C for 30 days. The high resolution X-ray diffraction pattern recorded after the long-time annealing treatment (Fig. 2.7) indicates that the initially present peak corresponding to the 111 reflection of the (Cu,Ni) alloy has split into two distinct 111 diffraction lines: One peak corresponding to the 111 reflection of the Cu-rich solid solution (α_1 phase) at $2\theta=43.7259^\circ$ and one peak corresponding to the 111 reflection of the Ni-rich solid solution (α_2 phase) at $2\theta=44.0945^\circ$. This is the first time that direct evidence has been provided for the decomposition of a (Cu,Ni) solid solution as caused by the presence of a miscibility gap at such low temperatures until now shown in the Cu-Ni phase diagram on the basis of thermodynamic calculation [18].

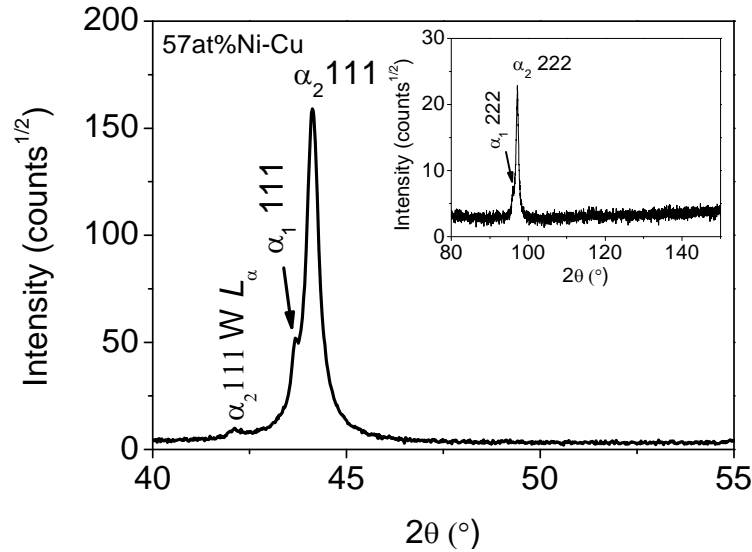


Fig. 2.7. High-resolution powder diffraction pattern of the originally homogenous (Cu,Ni) alloy layer containing 57 at% Ni after annealing at 300°C for 30 days. The pattern was recorded at room temperature using CuK α_1 radiation. α_1 and α_2 denote diffraction lines from the Cu-rich solid solution and Ni-rich solid solution resulting from the annealing induced decomposition. Note the presence of a weak peak at the lower-angle side of the 111 reflection of the α_1 phase caused by parasitic W L α radiation not fully suppressed by the monochromator.

2.3.4. Stress development

For an in-situ thermal treatment, the complete temperature cycle consists of three segments, namely heating from 30°C (ambient temperature in the diffractometer) to the annealing temperature, isothermal annealing, and cooling back to ambient temperature. The evolution of the internal, mechanical stresses (parallel to the surface) in the Ni and Cu sublayers of both ND and PA Ni-Cu diffusion couples during the three segments are shown in Figs. 2.8a-d for an annealing temperature of 225°C. A fully elastic accommodation of the thermal strain during heating and cooling as imposed by the (rigid, thick) substrate (in the following called 'thermal stress/strain') would result in linear dependencies of the stresses of the individual sublayers on temperature, which is the case for the PA bilayer as shown in Fig. 2.8(b).

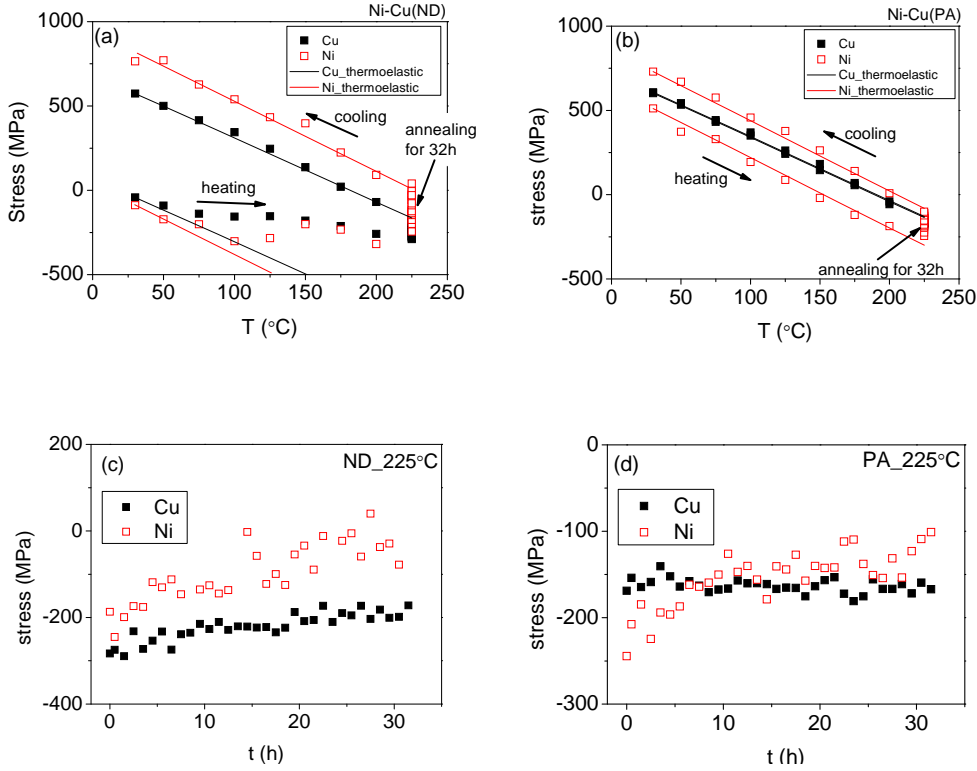


Fig. 2.8. Stress (parallel to the surface) evolution obtained from in-situ measurements in the originally pure Cu sublayer and the originally pure Ni sublayer of (a) and (c) normally deposited (ND) and (b) and (d) pre-annealed (PA) Ni/Cu bilayers during the heating and cooling cycle between 30°C and 225°C ((a) and (b)) and during the isothermal annealing for 32 hours ((c) and (d)).

The thermoelastic slopes \mathcal{E} ($\mathcal{E} = \Delta\sigma_{ij} / \Delta T$, i.e. stress (σ) changes per K) can be estimated from the coefficients of thermal expansion of the (sub)layers and the substrate and the so-called biaxial moduli of the (sub)layers. The theoretical extremes for the biaxial moduli are given by the cases of randomly oriented and of perfectly $\{111\}$ -fibre textured polycrystals and have been gathered in Table 2.2 (cf. Appendix of Ref. [3]). Considering the strength and the sharpness of the textures of both sublayers, it can be expanded that the values for perfectly $\{111\}$ -fibre texture polycrystals are appropriate estimates of reality for the present thin film systems. This is supported by comparison of the experimental results and theoretical predictions presented in Table 2.2.

Table 2.2. Thermoelastic slopes ($\bar{\epsilon}$) for the Ni and Cu sublayers of the Ni-Cu bilayer on a Si₃N₄/SiO₂/Si(100) substrate during cooling: Comparison of calculated and experimental values (elastic data and coefficients of thermal expansion were taken from Refs. [36] and [37], respectively). The experimentally determined values (last two columns) pertain to the cooling segment of the Ni and Cu sublayers of the PA bilayer.

$\bar{\epsilon}$, calc. (MPa/K)				$\bar{\epsilon}$, expt. (MPa/K)	
polycrystalline untextured		perfectly {111}-fibre textured			
Ni	Cu	Ni	Cu	Ni	Cu
-3.11	-2.85	-4.16	-3.79	-4.37	-3.85

Whereas the stress changes in the sublayers of the PA specimen exhibit thermoelastic behavior during both heating and cooling, this is only the case for the cooling segment for the sublayers of the ND specimen (cf. Figs. 2.8a and 2.8b). The stress development of the ND specimen upon *heating* can be discussed as follows: the residual stress contributions that emerge due to only diffusion between the (sub)layers in the bilayer can be determined by comparing the stress changes for the sublayers in the bilayer system with corresponding results obtained for single layers of the components in the bilayer system prepared and annealed under identical conditions. After subtraction of the calculated thermal *compressive* stress contribution developing upon heating it follows that significant *tensile* stress develops upon heating in both sublayers of the ND bilayer and in the single layers (see Figs. 2.9a and 2.9b). Thus, apart from thermal misfit as a source of stress, other stress-generating/relaxing mechanisms must be operative upon heating: (i) the relaxation of compressive thermal stress due to plastic yielding and (ii) the generation of tensile stress upon heating a layer sputter-deposited at ambient temperature due to the thermally activated compaction of the material as a consequence of grain growth [38] can be considered as possible sources of stress generation. The crystallite sizes, as obtained by diffraction line-broadening analysis [30], during heating up to the annealing temperature, subsequent isothermal annealing and following cooling, are shown for

the Ni and Cu single layers in Fig. 2.10. Indeed, substantial grain growth occurs in both layers during heating up to the annealing temperature. The evolutions of stress in the sublayers in the ND bilayer and in the single layers during heating are practically identical (Figs. 2.9a and 2.9b). Hence, it is concluded that grain growth (possibly in association with defect annihilation) is the dominant source of the tensile stress contribution developing during heating of the sublayers. A stress contribution due to interdiffusion during heating appears to be negligible.

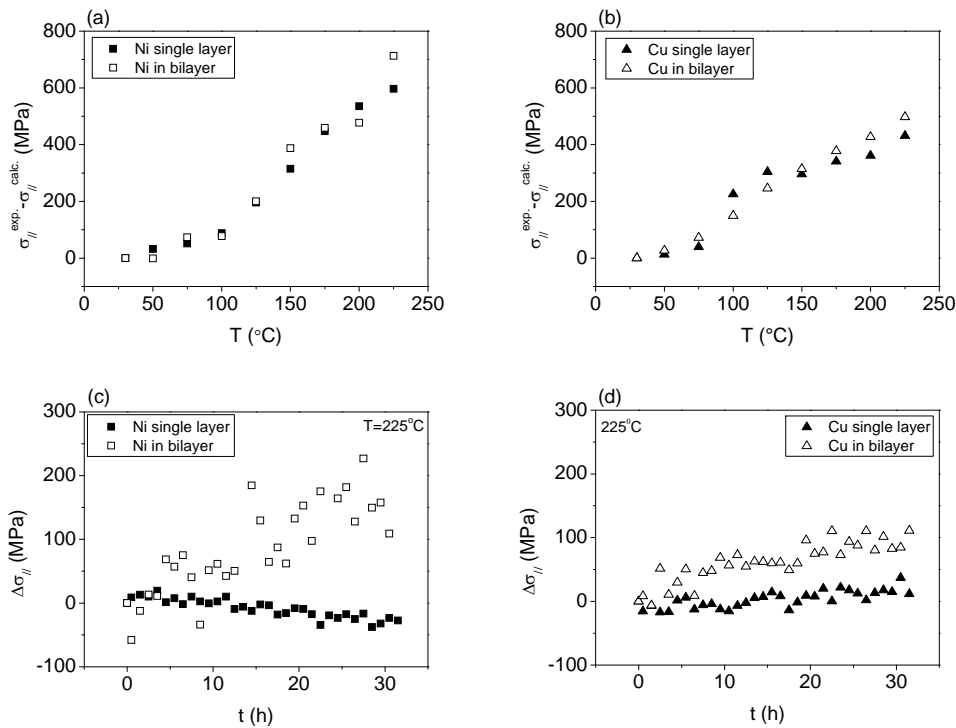


Fig. 2.9. Experimentally determined stress, $\sigma_{||}^{exp.}$, (in-situ measurements) minus the expected thermal stress contribution, $\sigma_{||}^{calc.}$, developing during heating to the annealing temperature (here 225°C) as function of temperature for (a) the Ni single layer and the Ni sublayer of the normally deposited bilayer, (b) the Cu single layer and the Cu sublayer of the normally deposited bilayer. Stress changes, $\Delta\sigma_{||}$, during annealing as function of time at the annealing temperature (here 225°C) for (c) the Ni single layer and the Ni sublayer of the normally deposited bilayer, (d) the Cu single layer and the Cu sublayer of the normally deposited bilayer.

For the as-prepared PA specimens, the lateral crystallite sizes are considerably larger than for the as-prepared ND specimens (ND: 20 nm for Cu, 15 nm for Ni; PA: 80 nm for Cu, 25 nm for Ni; all measured at $\psi = 70.5^\circ$; cf. Table 2.1). This makes plausible that distinct grain growth does not occur during heating of the PA specimens: a purely thermoelastic behavior prevails; no other stress generating or relaxing mechanism is found to be operative (see Fig. 2.8b).

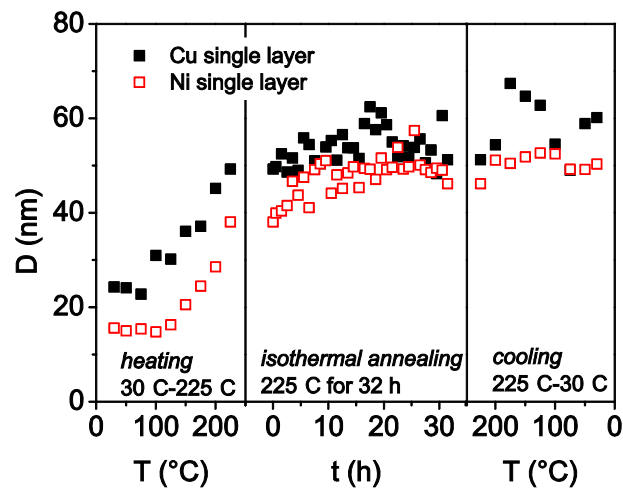


Fig. 2.10. Evolution of crystallite size of the Ni single layer and of the Cu single layer during heating to the annealing temperature of 225°C , subsequent isothermal annealing at 225°C for 32 hours and following cooling, as determined by diffraction line-broadening analysis (in-situ measurements).

Having arrived upon heating at the annealing temperature, evidently the stress of the single layers does not change distinctly during the isothermal anneal (see Figs. 2.9c and 2.9d). The stress of the pre-annealed Cu sublayer remains constant during the isothermal annealing (Fig. 2.8d) because neither grain growth nor significant diffusion into this Cu sublayer (cf. Fig. 2.4b) occurs. The modest stress change in the Ni sublayer for the pre-annealed specimen during the isothermal annealing (cf. Figs. 2.8d) is likely due to (marginal) grain growth during annealing.

This contrasts with the (continued; see above discussion) development of tensile stress contributions (200 MPa and 100 MPa for the Ni and Cu sublayers, respectively) in the sublayers of the ND specimen (Figs. 2.9c and 2.9d).

The following mechanisms leading to stress change during the isothermal annealing can be conceived: (i) interdiffusion (differences in the molar volumes and differences in the atomic fluxes of the diffusing species), (ii) (continued) grain growth, (iii) excess vacancy annihilation and shrinkage of grain-boundary voids, and (iv) plastic deformation (yielding; creep). Whereas mechanisms (ii) and (iii) invariably generate tensile stresses, mechanism (iv) always leads to stress relaxation (i.e. a decrease of the stress level). For both sublayers of the ND specimen, mechanism (iv) is less likely due to the relatively small stress level of the sublayers (Fig. 2.8c).

The influence of mechanism (i) on the change of the stresses of the Ni and Cu sublayers can be quantitatively determined as follows: if the diffusion-induced misfit with the rigid substrate due to volume changes of the sublayers is accommodated elastically, the corresponding diffusion-induced stress in the sublayer parallel to the surface, σ_{\parallel}^i , as compared to the state before interdiffusion, can be calculated from the relative volume change, $\Delta v/v$, as [5, 39]:

$$\sigma_{\parallel}^i = -\frac{M_{\{111\}}}{3} \frac{\Delta v_i}{v_i} \quad (2.4)$$

where $M_{\{111\}}$ is the biaxial modulus for the sublayer adopted in this work for the $\{111\}$ fibre-textured sublayers and $i=\text{Cu, Ni}$. $M_{\{111\}}^{\text{Ni}}$ and $M_{\{111\}}^{\text{Cu}}$, are calculated as 388.85 GPa and 261.26 GPa, respectively, according to Ref. [40]. The volume change, Δv_i resulting from concentration changes in the Cu and Ni sublayers can be expressed, assuming that the number of lattice sites in each layer is constant, as [5]:

$$\Delta v_{\text{Cu}} = N_{\text{Ni}}(\Omega_{\text{Ni}} - \Omega_{\text{CuV}}) + N_{\text{Cu}}(\Omega_{\text{CuV}} - \Omega_{\text{Cu}}) \quad (2.5)$$

$$\Delta v_{\text{Ni}} = N_{\text{Cu}}(\Omega_{\text{Cu}} - \Omega_{\text{NiV}}) + N_{\text{Ni}}(\Omega_{\text{NiV}} - \Omega_{\text{Ni}}) \quad (2.6)$$

where N_{Cu} and N_{Ni} are the moles of Cu and Ni crossing the initial interface during a diffusion anneal, respectively, and Ω_{Cu} and Ω_{Ni} are the molar volumes of Cu and Ni and the Ω_{CuV} and Ω_{NiV} are the molar volumes of vacancies in Cu and Ni. Eqs. (2.5.-2.7.) express that the influence of interdiffusion on the change of the stresses in both sublayers is the outcome of differences between (a) the flux of Ni atoms into the Cu

sublayer and the flux of Cu atoms into the Ni sublayer and (b) the molar volumes of Ni and Cu ($V_{Ni}=6.59 \text{ cm}^3$; $V_{Cu}= 7.11 \text{ cm}^3$). The molar volumes of vacancies in Cu and Ni can be taken as half of the molar volumes of Cu and Ni, respectively. Using these data $-\Delta v_i/N_i$ can be calculated as function of N_{Cu}/N_{Ni} (Fig. 2.11). The ratio $-\Delta v_i/N_i$ is proportional to σ_{\parallel}^i (Eq. (2.4.)): evidently, the sign and value of the diffusion-induced stress in the sublayers depend on the ratio N_{Cu}/N_{Ni} .

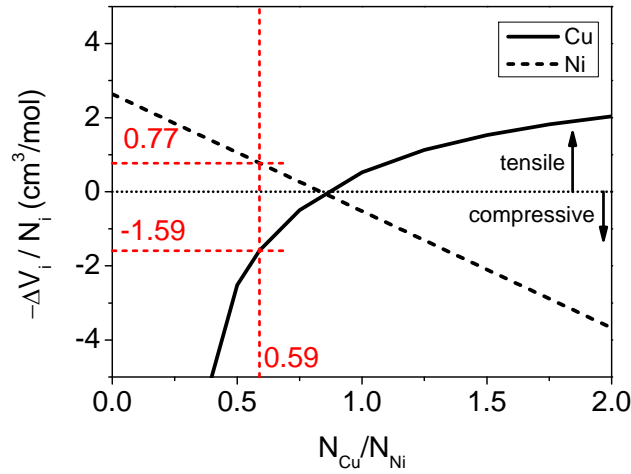


Fig. 2.11. Ratio, $-\Delta v_i/N_i$, ($i = Ni, Cu$) which is proportional to the diffusion-induced stress σ_{\parallel}^i versus the diffusion flux ratio N_{Cu}/N_{Ni} .

The concentration-depth profile of the ND Ni-Cu diffusion couple annealed at 225°C for 32 hours is revisited and shown in Fig. 2.12. The areas of the concentration profiles of Cu and Ni in the initially pure Ni and pure Cu sublayers, $A_{Cu \text{ in } Ni}$ and $A_{Ni \text{ in } Cu}$ can be determined as $A_{Cu \text{ in } Ni}=367.4$ and $A_{Ni \text{ in } Cu}=618.1$ (the unit is nm/100). The ratio, $A_{Cu \text{ in } Ni}/A_{Ni \text{ in } Cu}$, is then 0.59.

For a rough estimate (i.e. assuming that the original interface can be adopted as the Matano interface) the ratio $A_{Cu \text{ in } Ni}/A_{Ni \text{ in } Cu}$ can be taken as a measure of the ratio, N_{Cu}/N_{Ni} . Thus, N_{Cu}/N_{Ni} is 0.59 and N_{Ni}/N_{Cu} is 1.69 for the experiment considered (Figs. 2.9c,d and 2.12). According to Fig. 2.11, the corresponding values of $-\Delta v_i/N_i$ then are obtained as $0.77 \text{ cm}^3/\text{mol}$ and $-1.59 \text{ cm}^3/\text{mol}$ for Ni and Cu, respectively, as marked in Fig. 2.11. Hence, the diffusion-induced stress change in the Ni sublayer

after annealing at 225°C for 32 hours must be tensile, and the stress change in the Cu sublayer after annealing at 225°C for 32 hours must be compressive because the stress change is proportional to the value of $-\Delta v_i/N_i$ (Eq. (2.4.)).

The stress changes of the Ni sublayer and the Cu sublayer calculated from previous analysis indicate that the tensile stress generation in the Ni sublayer upon isothermal annealing at 225°C for 32 hours is likely due to interdiffusion. However, a tensile stress develops in the Cu sublayer during isothermal annealing (Fig. 2.9d). Hence, mechanisms (ii) (grain growth) and/or mechanism (iii) (excess vacancy annihilation and shrinkage of grain-boundary voids) must be operative. The tensile stress contribution in the Cu sublayer is thus the net outcome of interdiffusion (compressive stress contribution) and grain growth, excess vacancy annihilation and shrinkage of grain-boundary voids (all associated with tensile stress contributions).

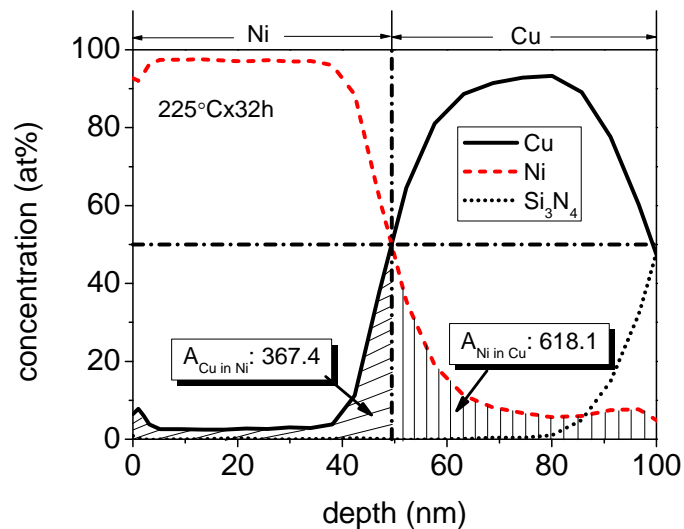


Fig. 2.12. Concentration-depth profile of the normally deposited (ND) Ni-Cu diffusion couple after isothermal annealing at 225° C for 32 hours. $A_{Cu \text{ in } Ni}$ and $A_{Ni \text{ in } Cu}$ (unit: nm/100) are the areas under concentration profiles of Cu in the initially pure Ni sublayer and of Ni in the initially pure Cu sublayer, respectively.

2.4. Conclusions

- 1) Annealing of Ni-Cu thin film (thickness of each sublayer: 50 nm) diffusion couples at temperatures between about 225°C - 300°C results in considerable diffusional intermixing, in particular via grain boundaries in the Cu sublayer.
- 2) A pre-annealing treatment of the Cu bottom layer results in a considerably lower grain-boundary density of *both* the (bottom) Cu layer and the (top) Ni layer. As a consequence, considerably less diffusional intermixing occurs in bilayers with pre-annealed Cu bottom sublayers upon annealing at temperatures between about 225°C - 300°C.
- 3) Upon heating up (in particular) and at the annealing temperature (lateral) grain growth occurs in the sublayers, except for the pre-annealed (Cu) sublayer. The pre-annealing (of the Cu, bottom layer) leads to a more pronounced (stronger and sharper) {111} fibre texture. The subsequent heating up and annealing leads to a strengthening and sharpening of the {111} fibre texture of the Ni, top sublayer to an extent matching that of the pre-annealed Cu, bottom sublayer, indicating that lateral growth (of Ni grains with {111} planes parallel to the surface) occurs to an extent prescribed by the lateral size of the grains (with {111} planes parallel to the surface) in the pre-annealed Cu, bottom sublayer.
- 4) For the first time, direct experimental evidence (by high-resolution X-ray powder diffraction) has been obtained for the existence of a miscibility gap in the Cu-Ni system by decomposition of an initial homogenous Cu-Ni alloy upon annealing at 300°C for 30 days (at about 1 atm).
- 5) *In-situ* X-ray diffraction investigations of single Ni and Cu layers demonstrated that the substantial grain growth occurring during heating to the annealing temperature is responsible for development of considerable tensile stress contribution, superimposed on the thermal stress developing in each (sub)layer due to the difference of the coefficients of thermal expansion of the (sub)layer and the substrate. During heating up (at least to 225°C) stress development due to interdiffusion is negligible.

6) During isothermal annealing at 225°C no distinct grain growth occurs. The isothermal annealing at 225°C induces a distinct tensile stress contribution in the Ni sublayer likely due to the interdiffusion process, whereas an occurring tensile stress contribution in the Cu sublayer is the net outcome of interdiffusion (compressive stress contribution) and grain growth, excess vacancy annihilation and shrinkage of grain-boundary voids (all associated with tensile stress contributions).

Acknowledgement

The authors are grateful to Dipl.-Ing. B. Siegle, Dr. L.P.H. Jeurgens and Dr. J.Y. Wang for Auger-electron spectroscopy measurements and assistance in the corresponding data evaluation, and to Dr. E. Bischoff for TEM analysis. Mr. F. Thiele and Dr. G. Richter are thankful for the preparation of the single and bilayer specimens.

References

- [1] Freund LB, Suresh S. Thin film materials: stress, defect formation, and surface evolution. Cambridge: Cambridge university press, 2006.
- [2] Ohring M. The materials science of thin films. San Diego: Academic press, 2002.
- [3] Chakraborty J, Welzel U, Mittemeijer EJ. J. Appl. Phys. 2008;103:113512.
- [4] Welzel U, Mittemeijer EJ. Diffusion and Defect Data 2007;264:71.
- [5] Kuru Y, Wohlschlögel M, Welzel U, Mittemeijer EJ. Thin Solid Films 2008;516:7615.
- [6] Kuru Y, Chakraborty J, Welzel U, Wohlschlogel M, Mittemeijer EJ. Mater. Sci. Forum 2006;524-525:801.
- [7] Stevens DW, ., Powell GW. Metall. Trans. A Phys. Metall. Mater. Sci. 1977;8:1531.
- [8] Beke DL, Szabó IA, Erdélyi Z, Opposits G. Mater. Sci. Eng. A Struct. Mater. 2004;387:4.
- [9] Daruka I, Szabo IA, Beke DL, Cserhati C, Kodentsov A, Loo FJJV. Acta Mater. 1996;44:4981.
- [10] Shewmon PG. Diffusion in solids. Warrendale, Pa.: Minerals, Metals, & Materials Society, 1989.
- [11] Larché FC, Cahn JW. Acta Metall. 1985;33:331.
- [12] Stoney GG. Proc. R. Soc. London, Ser. A: Containing Papers of a Mathematical and Physical Character 1909;82:172.
- [13] Welzel U, Ligot J, Lamparter P, Vermeulen AC, Mittemeijer EJ. J. Appl. Cryst. 2005;38:1.
- [14] Kuru Y, Wohlschlögel M, Welzel U, Mittemeijer EJ. Appl. Phys. Lett. 2009;163:112.
- [15] Welzel U, Lamparter P, Leoni M, Mittemeijer EJ. Mater. Sci. Forum 2000;347-349:405.
- [16] Welzel U, Lamparter P, Mittemeijer EJ. Mater. Res. Soc. Symp. Proc. 1999;562:147.
- [17] Bokstein B, Epishin A, Esin V, Mendeleev M, Rodin A, Zhevnenko S. Cross diffusion-stresses effects. In: Beke DL, Erdelyi Z, Szabo IA, editors. DS 2006:

- Diffusion and Stresses, vol. 264. Stafa-Zurich: Trans Tech Publications Ltd, 2007. p.79.
- [18] Subramanian PR, Chakrabarti DJ, Laughlin DE. Phase diagrams of binary copper alloys. OH: ASM international Materials Park, 1994.
- [19] Strecker A, Bader U, Kelsch M, Salzberger U, Sycha M, Gao M, Richter G, van Benthem K. Z. Metallkd. 2003;94:290.
- [20] Ho PS, Lewis JE, Howard JK. Journal of Vacuum Science and Technology 1977;14:322.
- [21] Wohlschlögel M, Welzel U, Maier G, Mittemeijer EJ. J. Appl. Cryst. 2006;39:194.
- [22] ProFit for Windows User's Guide: Philips Analytical X-ray, 1996.
- [23] Welzel U, Mittemeijer EJ. Mater. Sci. Forum 2004;443-444:131.
- [24] Gale WF, Totemeier TC. Sithells metals reference book. Amsterdam: Elsevier, 2004.
- [25] Welzel U, Mittemeijer EJ. J. Appl. Phys. 2003;93:9001.
- [26] Welzel U, Mittemeijer EJ. Materials Science Forum 2004;443-444:pp. 131.
- [27] Langford JI. J. Appl. Cryst. 1978;11:10.
- [28] Langford JI, Delhez R, de Keijser TH, Mittemeijer EJ. Aust. J. Phys. 1988;41:173.
- [29] Delhez R, de Keijser TH, Mittemeijer EJ. Fresenius Zeitschrift Für Analytische Chemie 1982;312:1.
- [30] Keijser THd, Langford JI, Mittemeijer EJ, Vogels ABP. J. Appl. Cryst. 1982;15:308.
- [31] Mittemeijer EJ, Scardi P. Diffraction analysis of the microstructure of materials. Berlin: Springer, 2004.
- [32] Wang JY, Mittemeijer EJ. Journal of Materials Research 2004;19:3389.
- [33] Levasseur J, Philibert J. CR. Acad. Sci. Paris 1967;264:277.
- [34] Lefakis H, Cain JF, Ho PS. Thin Solid Films 1983;101:207.
- [35] Welzel U, Ligot J, Lamparter P, Vermeulen AC, Mittemeijer EJ. J. Appl. Crystallogr. 2005;38:1.
- [36] Landolt-Boernstein. Numerical data and functional relationships in science and technology 1979;III/29a 1.2.1.:12.
- [37] Touloukian YS. Thermal Expansion: Metallic Elements and Alloys 1975:77.

- [38] Kuru Y, Wohlschlägel M, Welzel U, Mittemeijer EJ. J. Appl. Cryst. 2008;41:428.
- [39] Doerner MF, Nix WD. Crit. Rev. Solid State Mater. Sci. 1988;14:225.
- [40] Chakraborty J, Welzel U, Mittemeijer EJ. J. Appl. Phys. 2008;103.

3. Non-monotonic crystallite-size dependence of the lattice parameter of thin films of metals

J. Sheng, U. Welzel, E. J. Mittemeijer

Abstract

A non-monotonic crystallite-size dependence of the lattice parameter of ultrathin, nanocrystalline Ni films, i.e., *lattice contraction* followed by *lattice expansion* with decreasing crystallite size, was observed for the first time using *in-situ* X-ray diffraction stress measurements combined with a novel thermal treatment called ‘loop annealing’. The expected lattice contraction with decreasing crystallite size was found for nanocrystalline Cu and nanocrystalline Pd.

3.1. Introduction

The “size effect” is one of the most important aspects of nanostructured materials as pronounced changes of the properties of nanocrystalline solids (e.g. coefficient of thermal expansion [1], Young’s modulus [2] and magnetic properties [3]) can occur when the crystallite size is reduced [4]. Although the size dependence of the crystal-lattice parameter(s) has been frequently investigated since the 1950’s (cf. Ref. [5]), the experimental and theoretical results obtained until now are inconclusive: With decreasing crystallite size, the lattice parameters of nanocrystalline materials can, apparently, both contract (for example, Cu [6], Au [7], Sn [8] and Bi [8]) and expand (for example, Nb [9] and Ge [10]). Moreover, inconsistent experimental results have been presented: for example, both lattice contraction in Ni [11] and Pd [12], and lattice expansion in Ni [13-15] and Pd [16] have been reported. Several models/approaches have been proposed to understand the crystallite-size dependence of the lattice parameter(s). These consider the roles of, for example, intracrystalline pressure [13, 17], interface stress [18], interfacial excess volume [19], grain-boundary enthalpy [20], excess grain-boundary volume [21], and the effective negative Madelung pressure of ionic nanocrystals [22]. However, these explanations are of limited generality and none of them can explain all experimental findings.

In this work, the crystallite-size dependence of the lattice parameters of nanocrystalline Cu, Ni, and Pd single layers, with crystallite sizes ranging from about 10 nm to 95 nm, was investigated using an *in-situ* X-ray diffraction technique. The obtained results could be discussed as effects induced by the interface stress (for Cu, Pd and Ni (for crystallite size larger than 45 nm) and by the change of spin interaction, during the magnetic structural transition from multi-domain to single domain (for Ni, for crystallite size below about 45 nm).

3.2. Experimental details

3.2.1. Specimen preparation

Pure Cu, Ni and Pd thin films with thicknesses from 20 nm to 100 nm were prepared by direct current magnetron sputtering (base pressure about 5×10^{-8} mbar) onto Si (100) wafers covered with 50 nm SiO₂ and 50 nm Si₃N₄ barrier layers to prevent interdiffusion between the deposited layer and the substrate. The initial crystallite size was varied by tuning the magnetron power and the Ar partial pressure. The film thickness was determined by calibration of the deposition rate using a stylus profilometer. For this purpose a sample with a step in height was produced. The surface morphology and the film continuity/integrity were validated by atomic force microscopy (AFM) in contact mode using a Digital Instrument Nanoscope III at ambient conditions (cantilevers with a spring constant of $K \sim 0.03$ nN/nm were used).

3.2.2. Ex situ and in-situ X-ray diffraction measurements and their evaluation

The *ex-situ* and *in-situ* X-ray diffraction measurements were performed employing a Bruker D8 Discover diffractometer operating in parallel-beam geometry equipped with an X-ray lens in the incident beam, a parallel-plate collimator in the diffracted beam and an energy-dispersive detector. A domed hot stage DHS900 (Anton Paar) was mounted on the Eulerian cradle for the *in-situ* measurements. *In-situ* measurements on Ni and Pd were done under vacuum and *in-situ* measurements on Cu specimens were done under protective gas flow (N₂+H₂) because Cu oxidizes more easily than Ni and Pd. The software ProFit [23] was used to fit measured diffraction lines by symmetric Pseudo-Voigt functions for the determination of

diffraction-line position, maximum intensity, full width at half maximum and peak-shape parameter.

Residual stresses (of in-plane, biaxial and rotationally symmetric nature, as verified in this study; characterized by the symbol $\sigma_{//}$) were measured employing the crystallite-group method making use of the 111 reflections of the metal films, as all layers investigated had a strong and sharp {111} fiber texture (see below) [24]. The strain-free lattice parameters were determined from the interplanar spacing of the {111} lattice planes by interpolating at the strain-free direction $\sin^2 \psi^*$ (ψ is the angle between the diffraction vector and the specimen surface normal) [25]. The crystallite sizes were evaluated employing single-line broadening analysis with the diffraction vector oriented nearly parallel to the specimen surface ($\psi=70.53^\circ$) [26-27]. The instrumental broadening was obtained from the measurement of a standard specimen of LaB₆ (SRM 660a provided by the National Institute for Standards and Technology, Gaithersburg). More sophisticated methods for the analysis of the diffraction-line broadening exist [27]. However, the single-line method can be employed relatively easily and, of pronounced importance here, rapidly (as only one particular diffraction line has to be recorded) to obtain estimates for the size of the coherently diffracting domains D and the microstrain ε and thus is in particular suited to trace the evolution of these parameters *in-situ* as function of temperature.

A new approach, called “loop annealing” in the following, was devised to investigate *in-situ* variations of the strain-free lattice parameters as function of crystallite size: The as-deposited specimens containing nano-sized crystallites are sequentially annealed isothermally at temperatures increasing with each step (‘loop’). After each anneal at a given temperature, the specimen is cooled back to room temperature for performing the X-ray diffraction measurement. For each annealing step, the specimen is heated isochronically (heating rate is 0.1 K/s) to the annealing

temperature, which is maintained for five minutes. The cooling to room temperature has an undefined cooling rate, as the chamber used facilitates only free cooling (i.e. heat is removed only by thermal conduction to the surroundings of the heating chamber). This ‘loop annealing’ has two advantages: (i) Accurate knowledge of the coefficient of thermal expansion is not required, as all X-ray diffraction measurements are done at the same, ambient temperature and (ii) the time required for investigating a certain range of crystallite sizes is drastically reduced as compared to *ex-situ* annealing of the specimens in a furnace, where each anneal at a certain temperature requires transferring the specimen from the diffractometer to the furnace and vice versa. One X-ray diffraction measurement at ambient temperature consists of two scans covering the angular range comprising the 111 reflection at two tilt angles ($\psi = 0^\circ$ and $\psi = 70.5^\circ$) and takes less than half an hour including a waiting time of five minutes at ambient temperature to guarantee temperature homogenization and stability.

3.3. Results

The as-deposited layers of Cu, Ni, and Pd show strong and sharp {111} fiber textures (e.g. for the as-deposited 50 nm Ni layer the pole width, i.e. the full width at half maximum for the intensity maximum at the center of pole figure recorded using the 111 reflection, is only 5.4°). This justifies the use of the crystallite-group method for diffraction stress analysis and determination of the unstrained lattice plane spacing [28]. In addition, the thin films used in this work are closed and smooth (even for the thinnest layers of thickness 20 nm, the root mean square roughnesses of the layers are below about 1.30 nm according to the AFM measurements).

The 50 nm thick Ni layer and the 50 nm thick Pd layer with initial crystallite sizes of about 15 nm were ‘loop-annealed’ from room temperature up to 450°C with temperature steps of 25°C. The 20 nm thick Pd single layer exhibited a smaller as-deposited crystallite-size (10 nm) and was loop-annealed up to 325°C with temperature steps of 25°C. After annealing at each elevated temperature, the 111 reflections were recorded at two tilt angles ψ , 0° and 70.53°, after the specimen had been cooled back to room temperature (see above). The thus determined changes of the strain-free lattice parameters of the Ni and Pd films have been plotted versus the inverse crystallite size in Figs. 3.1 and 3.2, respectively.

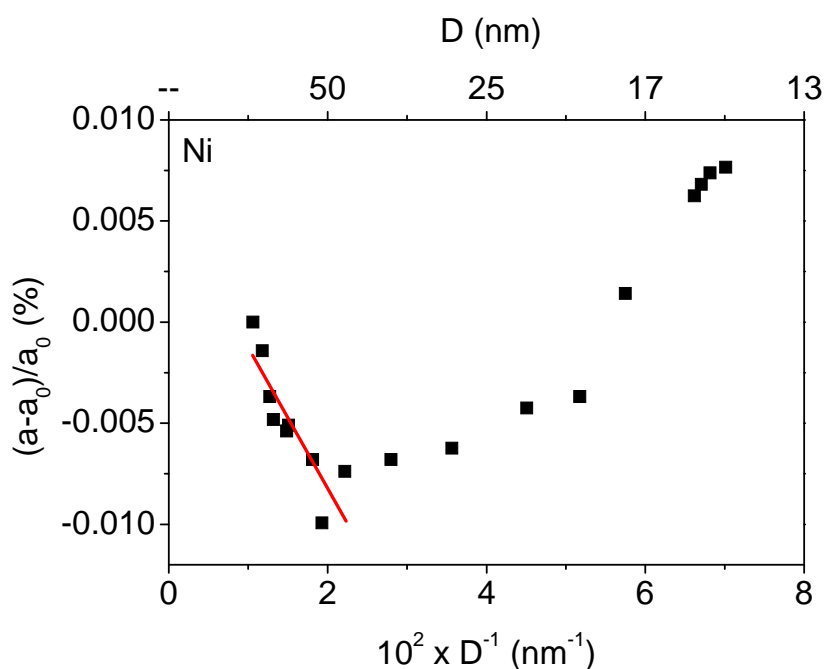


Fig. 3.1. Fractional change of the strain-free lattice parameter, $(a-a_0)/a_0$ (a_0 is the value obtained for the specimen exhibiting the largest crystallite size), of the 50 nm thick Ni layer upon ‘loop annealing’ up to 450°C under vacuum as function of the reciprocal crystallite size, D^{-1} .

For investigating the crystallite-size dependence of the strain-free lattice parameter of nanocrystalline Cu, a 50 nm thick Cu layer with an initial crystallite size of about 23 nm was investigated in-situ by ‘loop-annealing’ from room temperature up to 450°C with temperature steps of 25°C (the results obtained are represented by the black squares in Fig. 3.3). In addition, as-deposited Cu single layers of different thicknesses were investigated ex-situ (the results obtained are represented by the open data points in Fig. 3.3). The combination of the ex-situ results with the in-situ results made investigation of a wide range of crystallite size possible, as only by reduction of the film thickness crystallite sizes below about 20 nm can be obtained.

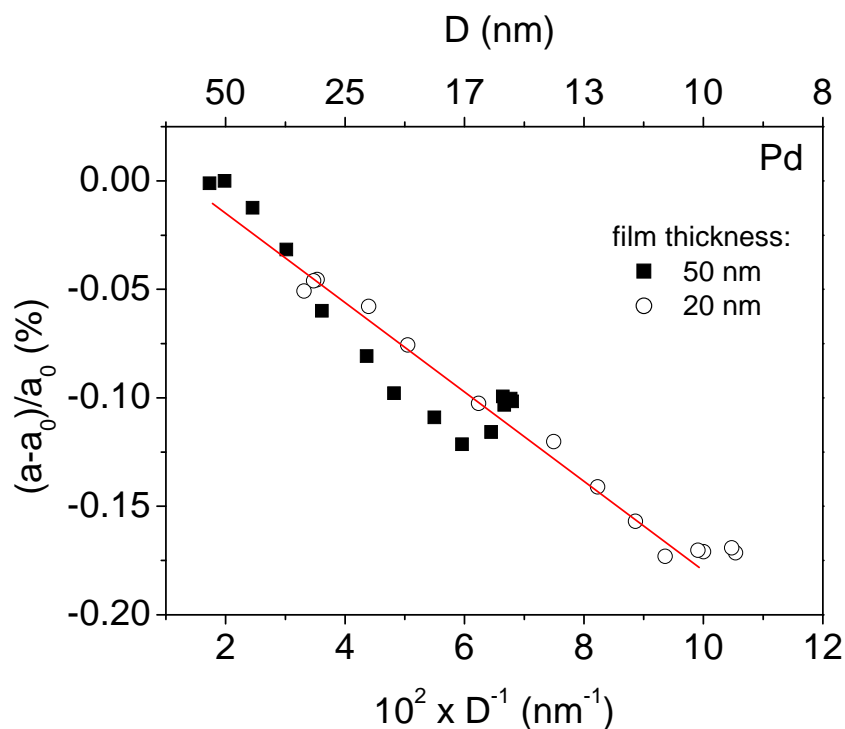


Fig. 3.2. Fractional change of the strain-free lattice parameter, $(a-a_0)/a_0$, (a_0 is the value obtained for the specimen exhibiting the largest crystallite size), of the ultrathin Pd thin layers as function of the reciprocal crystallite size, D^{-1} . The 50 nm thick Pd layer (black squares) was ‘loop-annealed’ under vacuum up to 450°C, and the 20 nm thick Pd layer (open circles) was loop-annealed under vacuum up to 325°C.

Both Cu and Pd exhibit a distinct lattice contraction with decreasing crystallite size. A strikingly different result is obtained for Ni: Upon decreasing crystallite size, the strain-free lattice parameter first decreases and subsequently shows a pronounced increase below a crystallite size of about 45 nm.

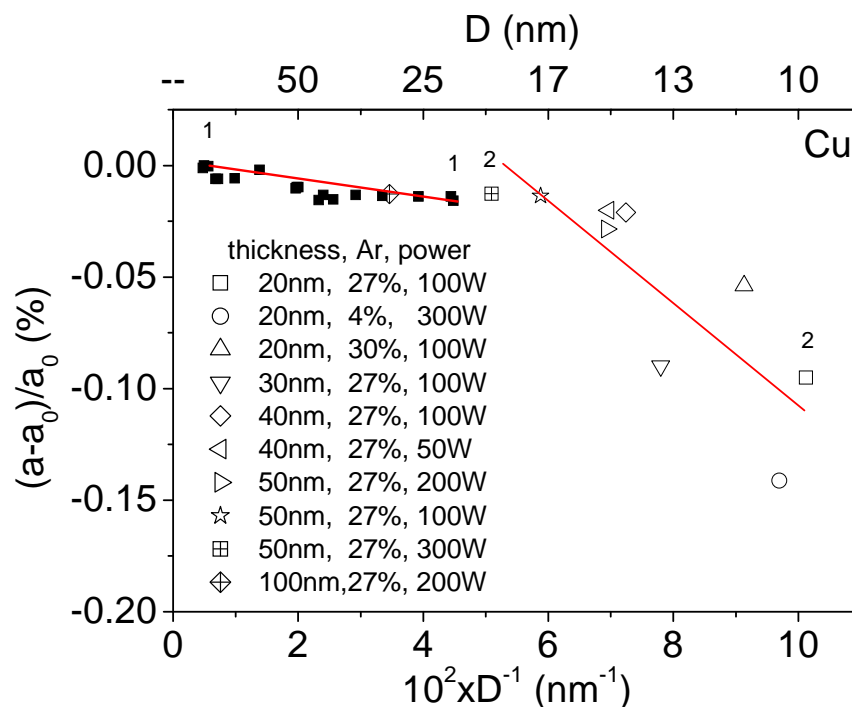


Fig. 3.3. Fractional change of the strain-free lattice parameters, $(a-a_0)/a_0$, (a_0 is the value obtained for the specimen exhibiting the largest crystallite size), of the ultrathin Cu layers as function of the reciprocal crystallite size, D^{-1} . The data were obtained from in-situ measurement upon 'loop annealing' up to 450° C under protective (N_2+H_2) gas flow (black squares; Cu layer of thickness 50 nm) and from ex-situ measurements of as-deposited specimens of different thickness, as indicated in the figure and as prepared employing different deposition parameters as also indicated in the figure (Ar flow set by a flow controller determines the pressure in the deposition chamber and the magnetron power).

3.4. Discussion

(Surface and) Interface stresses have been successfully identified as sources for lattice contraction of nanocrystalline materials [18]. The lattice contraction induced by interface stress can be given by [12]:

$$\frac{a - a_0}{a_0} = -\frac{4}{3K} \sigma_s \frac{1}{D} \quad (3.1.)$$

where $(a-a_0)/a_0$, K , σ_s , and D are the relative change of the lattice constant, the bulk modulus, the interface stress, and the volume-weighted crystallite size, respectively. Hence, the interface stress can be determined from the slope of the straight line fitted to the data in a plot of the fractional lattice-parameter change vs. reciprocal crystallite size.

By fitting a straight line to the measured data for the dependences of the lattice parameter versus reciprocal crystallite size as shown for Pd in Fig. 3.2, an interface stress of 2.62 ± 0.16 N/m is obtained for Pd. This value is comparable to the value obtained by Birringer *et al.* (1.2 N/m) as obtained by combining X-ray diffraction lattice parameter measurement with X-ray diffraction Warren-Averbach line broadening analysis [29]. The discrepancy is probably due to (i) a difference in the definitions of surface stress and interface stress (see detailed discussion in Ref. [30]), and/or (ii) due to experimental inaccuracies.

For Cu, two separate linear regions can be distinguished for the data on the dependence of the lattice parameter on crystallite size (see Fig. 3.3): One below a crystallite size of about 20 nm and one above. The corresponding values derived for the interface stress are 0.37 ± 0.06 N/m (above 20 nm) and 2.33 ± 0.60 N/m (below

20 nm). Thus, a drastic increase of the interface stress occurs below a crystallite size of about 20 nm. The interface stress depends on the grain-boundary structure, which is related to the grain-boundary excess volume. According to Ref. [31], the excess volume per unit grain-boundary area, Δa , of nanocrystalline Pd and Ni is much larger than for coarse-grained Pd and Ni. A higher excess free volume leads to higher grain boundary energy due to an increasing proportion of high-energy atomic sites [32-33]. Since the interface stress, σ_s , is related to the grain boundary energy, γ_{Gb} , by $\sigma_s = \gamma_{Gb} + \frac{\partial \gamma_{Gb}}{\partial \varepsilon}$ (ε is the homogeneous variational strain; cf. Ref. [34]), an increase of grain-boundary energy will likely lead to an increase of the interface stress.

Hence, a non-linear variation of the lattice parameter of Cu thin films with decreasing crystallite size can be expected. The occurrence of a constant interface stress for Pd within the range of crystallite size investigated implies that a similar increase of interface stress, as observed for Cu, could also occur for Pd, but at crystallite sizes below about 10 nm.

The lattice parameter of nanocrystalline Ni, surprisingly, first exhibits a contraction and thereafter an expansion with decreasing crystallite size. The contraction-expansion transition occurs at a crystallite size of about 45 nm. If the crystallite size of Ni is above about 45 nm, the lattice parameter of Ni exhibits contraction with a maximum fractional change of the lattice parameter of about -0.01% at a crystallite size of about 45 nm, which, at this crystallite size of about 45 nm, is similar as for the case of Cu (note the difference in ordinate scales of Figs. 3.1 and 3.3). The evaluation of the interface stress of Ni, by fitting a straight line to the more or less linear, first part of the fractional change of the lattice parameter vs. reciprocal crystallite size, yields an interface-stress value (0.93 ± 0.19 N/m) compatible with corresponding data for other metals (see above results and Ref. [11]).

Lattice expansion of Ni occurs for decreasing crystallite size beyond the “critical” crystallite size of about 45 nm. Lattice expansion (only) has been reported before for nanocrystalline Ni powder and has been attributed to a decrease of intracrystalline pressure resulting from the electrostatic interaction of ions and electrons in the metal lattice [13, 17]. It is suggested here that the contraction-expansion transition occurring for ferromagnetic Ni (but not for diamagnetic Cu and paramagnetic Pd) may be caused by a magnetic multi domain-single domain transition at a “critical size” value, which is a well-known phenomenon for ferromagnetic materials as Ni, Co and Fe [35]. Upon the transition from a multidomain to a single domain microstructure the spin directions within a grain, departing from a more or less random distribution, become uniformly oriented. The multi domain-single domain transition occurs at about 42 nm for a spherical Ni particle according to Refs. [36-37], which value indeed is in the range of “critical size” values observed in this study for the contraction-expansion transition.

3.5. Conclusion

In conclusion, the crystallite-size dependences of the lattice parameters of nanocrystalline Ni, Cu, and Pd thin films have been investigated. The interface stresses acting in nanocrystalline Ni, Cu, and Pd have been evaluated quantitatively from the decrease of strain-free lattice parameter upon decreasing crystallite size. The interface stress can depend on the crystallite size (as shown for Cu) because the grain-boundary excess volume depends on crystallite size. For the first time, a non-monotonic behavior of the lattice parameter of Ni has been observed: first a decrease, then an increase with decreasing crystallite size. The change of spin interaction in

ferromagnetic material (as Ni, for crystallite size below about 45 nm), during the transition from multi domain to single domain, may cause a lattice expansion. Because lattice contraction and lattice expansion are counteracting effects, one or the other may be dominating depending on the range of crystallite size investigated.

Acknowledgement

The authors are grateful to Dr. Z. M. Wang (Max Planck Institute for Metals Research) for fruitful discussion and to Mr. F. Thiele (Max Planck Institute for Metals Research) for specimen fabrication.

References

- [1] Kuru Y, Wohlschlägel M, Welzel U, Mittemeijer EJ. *Appl. Phys. Lett.* 2007;90:243113.
- [2] Chen CQ, Shi Y, Zhang YS, Zhu J, Yan YJ. *Phys. Rev. Lett.* 2006;96.
- [3] Zhong WH, Sun CQ, Li S. *Solid State Commun.* 2004;130:603.
- [4] Gleiter H. *Acta Mater.* 2000;48:1.
- [5] Boswell FWC. *Proc. Phys. Soc. London, Sect. A* 1951;64:465.
- [6] Apai G, Hamilton JF, Stohr J, Thompson A. *Phys. Rev. Lett.* 1979;43:165.
- [7] Mays CW, Vermaak JS, Kuhlmann D. *Surf. Sci.* 1968;12:134.
- [8] Yu XF, Liu X, Zhang K, Hu ZQ. *J. Phys.: Condens. Matter* 1999;11:937.
- [9] Chatterjee PP, Pabi SK, Manna I. *J. Appl. Phys.* 1999;86:5912.
- [10] Wang ZM, Wang JY, Jeurgens LPH, Phillip F, Mittemeijer EJ. *Acta Mater.* 2008;56:5047.
- [11] Birringer R, Zimmer P. *Acta Mater.* 2009;57:1703.
- [12] Lamparter P, Mittemeijer EJ. *Int. J. Mat. Res.* 2007;98:485.
- [13] Gamarnik MY. *Phys. Status Solidi B* 1991;168:389.
- [14] Okram GS, Devi KN, Sanatombi H, Soni A, Ganesan V, Phase DM. *J. Nanosci. Nanotechnol.* 2008;8:4127.
- [15] Liu XD, Zhang HY, Lu K, Hu ZQ. *J. Phys.: Condens. Matter* 1994;6:L497.
- [16] Heinemann K, Poppa H. *Surf. Sci.* 1985;156:265.
- [17] Gamarnik MY. *Phys. Status Solidi B* 1991;164:107.
- [18] Vermaak JS, Mays CW, Kuhlmann D. *Surf. Sci.* 1968;12:128.
- [19] Lu K, Sui ML. *Scripta Metall. Mater.* 1993;28:1465.
- [20] Lu K, Sun NX. *Philos. Mag. Lett.* 1997;75:389.
- [21] Qin W, Chen ZH, Huang PY, Zhuang YH. *J. Alloys Compd.* 1999;292:230.

- [22] Perebeinos V, Chan SW, Zhang F. *Solid State Commun.* 2002;123:295.
- [23] ProFit for Windows User's Guide: Philips Analytical X-ray, 1996.
- [24] Welzel U, Mittemeijer EJ. *Mater. Sci. Forum* 2004;443-444:pp. 131.
- [25] Welzel U, Ligot J, Lamparter P, Vermeulen AC, Mittemeijer EJ. *J. Appl. Cryst.* 2005;38:1.
- [26] Mittemeijer EJ, Scardi P. *Diffraction analysis of the microstructure of materials.* Berlin: Springer, 2004.
- [27] Mittemeijer EJ, Welzel U. *Zeitschrift Fur Kristallographie* 2008;223:552.
- [28] Hauk V, Vaessen G. *Z. Metallkd.* 1985;76:102.
- [29] Birringer R, Hoffmann M, Zimmer P. *Phys. Rev. Lett.* 2002;88:206104.
- [30] Sheng J, Welzel U, Mittemeijer EJ. In preparation.
- [31] Kuru Y, Wohlschlögel M, Welzel U, Mittemeijer EJ. *Appl. Phys. Lett.* 2009;95.
- [32] Olmsted DL, Foiles SM, Holm EA. *Acta Mater.* 2009;57:3694.
- [33] Wolf D. *Acta Metall.* 1989;37:1983.
- [34] Sutton AP, Balluffi RW. *Interfaces in crystalline materials.* Oxford New York: Oxford University Press, 1995.
- [35] Cullity BD, Graham CD. *Introduction to Magnetic Materials: Wiley-IEEE Press,* 2008.
- [36] Kitakami O, Sakurai T, Miyashita Y, Takeno Y, Shimada Y, Takano H, Awano H, Ando K, Sugita Y. *Jpn. J. Appl. Phys. Part 1* 1996;35:1724.
- [37] Brown WF. *Phys. Rev.* 1957;105:1479.

4. The lattice parameter of nanocrystalline Ni as function of crystallite size

J. Sheng, G. Rane, U. Welzel, E. J. Mittemeijer

Abstract

An anomalous dependence on crystallite size of the lattice parameter of nanocrystalline Ni as occurring in ultrathin Ni films and in ball-milled Ni powder was observed: *lattice contraction* followed by *lattice expansion* with decreasing crystallite size. These data were determined by application of detailed *in-situ* X-ray diffraction measurements during annealing treatments. To this end, the lattice parameter of Ni was accurately determined by correcting for influences of residual stress and stacking faults in the thin films and ball-milled Ni powders, respectively. The non-monotonic variation of the lattice constant was discussed in terms of competing mechanisms: interface stress induced contraction versus magnetic multi-domain to single-domain transition occurring at about the crystallite size value where a minimum value for the lattice parameter is observed.

4.1. Introduction

The properties of nano-sized materials can be rather different from corresponding coarse-grained material. For example, the coefficient of thermal expansion [1], the Young's modulus [2], and the magnetic properties [3]) can change pronouncedly when the crystallite size is reduced [4]. Although the size dependence of the crystal-lattice parameter(s) has been frequently investigated since the 1950's (cf. Ref. [5]), the experimental and theoretical results obtained until now are inconclusive. Several models/approaches have been proposed to understand the crystallite-size dependence of the lattice parameter(s). These consider the roles of, for example, intracrystalline pressure [6-7], interface stress [8], interfacial excess volume [9], grain-boundary enthalpy [10], excess grain-boundary volume [11], or the effective negative Madelung pressure of ionic nanocrystals [12-13]. However, these explanations are of limited generality and none of them can explain all experimental findings.

Experimental results indicate that, with decreasing crystallite size, the lattice parameters of nanocrystalline materials can, apparently, either contract (for example, Cu [14], Au [15], Sn [16], and Bi [16]) or expand (for example, Nb [17], and Ge [18]). Moreover, inconsistent experimental results have been presented: for example, both lattice contraction in Ni [19] and Pd [20], and lattice expansion in Ni [6, 21-22] and Pd [23] have been reported. Such inconsistent experimental results maybe partly caused by experimental pitfalls: As an example, a correction of measured lattice-plane spacings for the presence of residual stresses is indispensable, in particular when investigating nanocrystalline thin films. Further, the presence of stacking faults, which can occur in particular in nanocrystalline materials produced by severe plastic deformation processes, as ball-milling and high-pressure torsion, may also affect measured peak positions and thus lattice-plane spacings [24].

In this work, the dependence of the lattice parameters of nanocrystalline Ni on crystallite size has been investigated employing (i) nanocrystalline thin Ni films prepared by physical vapor deposition (PVD, here: DC-magnetron sputtering) and (ii) nanocrystalline Ni powders prepared by severe plastic deformation (SPD, here: ball milling). Particular care has been taken to avoid experimental pitfalls as mentioned above for the accurate determination of the lattice parameter(s): the effects of residual stresses in the thin Ni films and of stacking faults in the ball-milled Ni powder have been accounted for quantitatively.

For both types of nanocrystalline nickel, the same non-monotonic dependence of the lattice parameter on crystallite size has been established (see Section 4.3.4). The possible background for this phenomenon has been discussed in Section 4.4.

4.2. Experimental procedures and data evaluation

4.2.1 Specimen preparation and processing

Ni thin films with a thickness of 20 nm and 50 nm were prepared by direct current magnetron sputtering (base pressure about 5×10^{-8} mbar) on Si (100) wafers covered with a 50 nm thick, amorphous SiO₂ layer and a 50 nm thick, amorphous Si₃N₄ layer on top, which layers act as diffusion barrier layers. The purity of the Ni target is 99.99 wt%. Prior to the deposition, the substrates were sputter-cleaned for about 1 minute with Ar⁺ ions accelerated with -105 V. During the film deposition, the chamber pressure was maintained at 1.4×10^{-4} mbar using Ar as a sputter gas. The specimens were rotated around the surface normal at a rate of a few tens of revolutions per minute to assure in-plane isotropy of the microstructure of the film.

Ni powder (purity of 99.8 wt.-%) with a particle size of less than 50 μm was subjected to ball milling for durations of 1 minute up to 80 hours at room temperature in a planetary ball mill (Fritsch Pulverisette P6). A custom-made Ni milling case and Ni milling balls were used in order to avoid contamination of the powder with wear products from the milling case or the balls. The mill was operated at a constant speed of 150 rpm with a ball-to-powder weight ratio of 10:1. About 10 g of Ni powder was used in one milling run. The handling of the powders before milling and the sealing of the milling vessel were performed in a glove box under an Ar atmosphere. Part of the as-received Ni powder was encapsulated in an evacuated quartz tube and heated to 900 °C in a furnace for 10 minutes for the preparation of a Ni reference sample containing no significant amount of crystal defects and a crystallite size exceeding 1 μm . In order to produce Ni powders of different nanocrystallite size, Ni powders milled for 5 hours were encapsulated in an evacuated quartz tube and annealed at temperatures between 250°C and 375°C in a furnace for various durations.

All Ni powder specimens, i.e. unmilled, ball-milled and annealed, Ni powders, were analyzed for oxygen and nitrogen impurities by carrier gas hot extraction. For the specimen milled for the longest duration (80 hours), oxygen contamination was found to be about 2 at.% and nitrogen contamination was found to be about 0.1 at.%. The X-ray diffraction diagrams of all these Ni powder specimens did not show any lines of impurity phases, i.e. only the diffraction lines of fcc Ni were observed.

4.2.2. Microstructure investigation

The morphology and the film continuity were investigated by atomic force microscope (AFM) in contact mode using a Digital Instrument Nanoscope III at ambient conditions (cantilevers with a spring constant of $K \sim 0.03$ nN/nm were used).

The cross-sectional microstructure of both as-deposited and annealed Cu-Ni thin-film diffusion couples was investigated using a Philips CM200 transmission electron microscope (TEM) operated with a 200 kV electron beam. The TEM samples were prepared by cutting two pieces off the bilayer/substrate specimens and sandwiching these pieces (bilayers of both pieces facing each other) with epoxy glue. After subsequent mechanical thinning by grinding, the resulting thin slice of material was embedded with the film surface parallel to the cylinder axis into a specially designed cylindrical polycrystalline Al₂O₃ tube of 3 mm diameter as a holder for the cross-sectional sample. Then, the tube was cut into slices with a thickness about 350 μm. The slices underwent mechanical grinding, dimpling from both sides, and, finally, ion thinning (Ar⁺ ions with 3.5 keV energy and 1 mA ion current in a BAL-TEC RES 010 apparatus with liquid nitrogen cooling) for several hours to achieve electron transparency. Details of the cross-sectional specimen preparation can be found elsewhere [25].

For the powder specimens, the TEM specimens were prepared using a FIB Nova Nanolab 600, following the lift-out technique [26] applied to individual powder particles. The procedure is as follows: A protective Pt layer was deposited all around on the surface of a selected powder particle to prevent Ga⁺ damage in the region of interest during the following cutting and thinning process. Then, applying a focused Ga⁺ ion beam operating at 30 KeV, a thin slice of the Ni powder particle was cut and ion-beam cleaned. This slice of the powder particle was picked thereafter using a micro manipulator and then welded onto a Cu grid for TEM examination. Finally, this sample was thinned to electron transparency using low Ga⁺ ion currents of 10-30 pA.

4.2.3. Ex situ and in situ X-ray diffraction measurements and their evaluation

The *ex-situ* and *in-situ* X-ray diffraction measurements of the Ni thin films were performed with $\text{CuK}\alpha$ radiation employing a Bruker D8 Discover diffractometer, operating in parallel-beam geometry, equipped with an X-ray lens in the incident beam, a parallel-plate collimator in the diffracted beam and an energy-dispersive detector. A domed hot stage DHS900 (Anton Paar) was mounted onto the Eulerian cradle for the *in-situ* measurements, which were carried out under vacuum.

X-ray diffraction measurements of the ball-milled Ni powders were made with $\text{Cu K}\alpha$ radiation employing a Philips (now: Panalytical) MRDpro diffractometer, operating in parallel-beam geometry equipped with an X-ray lens in the incident beam, a parallel-plate collimator in the diffracted beam and a proportional counter. The parallel-beam geometry avoids aberrations related to specimen roughness, transparency and displacement that would occur in a powder diffractometer based on focusing geometry (e.g. Bragg-Brentano geometry). The specimens for the measurement were prepared by spreading the powder on a double sided tape on a glass slide.

The software ProFit [27] was used to fit the measured diffraction lines by Pseudo-Voigt functions for the determination of the diffraction-line positions, the intensities, the full widths at half maximum and the peak-shape parameters.

Residual stresses (of in-plane, biaxial and rotationally symmetric nature, as verified in this study; characterized by the symbol $\sigma_{//}$) and strain-free lattice parameters of the Ni thin films were measured employing the crystallite-group method making use of the 111 reflections, as all layers investigated had a strong and sharp fiber texture (see below) [28]. The strain-free lattice parameters were determined from the interplanar spacing of the $\{111\}$ lattice planes, as measured as

The lattice parameter of nanocrystalline Ni as function of crystallite size

function of ψ , where ψ is the angle between the diffraction vector and the specimen surface normal, by interpolating at the strain-free direction $\sin^2 \psi^*$ [29]. A correction for an offset of the diffraction angle scale was performed on the basis of measurement of the peak positions of a LaB₆ (NIST SRM660a) standard powder sample.

A special approach, called “loop annealing” in the following, was devised to investigate the *in-situ* variation of the strain-free lattice parameter of the thin Ni films as function of crystallite size: The as-deposited specimens containing nano-sized crystallites were annealed isothermally, sequentially at temperatures increasing with each step (‘loop’). After each anneal at a given temperature, the specimen was cooled back to room temperature for performing the X-ray diffraction measurement. For each annealing step, the specimen was heated isochronically (with a heating rate of 0.1 K/s) to the annealing temperature, which was maintained for five minutes. The cooling to room temperature had an undefined cooling rate, as the heating chamber used allows for only free cooling (i.e. heat is transferred by only thermal conduction to the surroundings of the heating chamber). This ‘loop annealing’ has two advantages: (i) accurate knowledge of the coefficient of thermal expansion is not required, as all X-ray diffraction measurements are performed at the same, ambient temperature, (ii) the time required for investigating a certain range of crystallite sizes is drastically reduced as compared to *ex-situ* annealing of the specimens in a furnace, where each anneal at a certain temperature requires transferring the specimen from the diffractometer to the furnace and vice versa. One measurement at ambient temperature consists of two scans, covering the diffraction-angular range containing the 111 reflection, at two tilt angles ($\psi = 0^\circ$ and $\psi = 70.53^\circ$) and takes less than half an hour including a waiting time of five minutes at ambient temperature to guarantee temperature homogenization and stability.

For the Ni powder specimens, the lattice parameter was determined as follows: As it is well-known that severe plastic deformation (SPD) induced by prolonged ball milling can lead to a considerable density of planar, stacking faults, a correction for such stacking faults is indispensable, as stacking faults on the (111) planes of a FCC metal produce broadening *and* shifting of diffraction lines [30-31]. It is difficult to obtain information about faulting from only line broadening measurements as the broadening is affected by crystallite size, microstrain and faulting. However, the peak-maximum position is affected solely by faulting (in the absence of macrostrain) so that a direct determination of the stacking fault probability can be made using such data. The stacking fault probability α can be determined from a change of the diffraction-angular separation of the Ni 111 and 200 reflections with respect to a Ni powder specimen containing no stacking faults. The diffraction-angular separation of the 111 and 200 diffraction lines, $(2\theta_{200} - 2\theta_{111})$, in the absence of stacking faults was obtained from a Ni powder sample annealed at 900°C for 10 minutes. The absence of crystal defects in this Ni reference sample was verified by comparing its diffraction-line broadening with the instrumental line broadening as recorded from a LaB₆ powder sample: The line broadening (characterized by, for example, the full width at half maximum (FWHM)) of the Ni powder sample was identical to that of the instrumental line broadening (obtained by interpolating the FWHM of the LaB₆ diffraction lines at the peak positions of the Ni peaks). The effect of stacking faults is to move the 111 diffraction line to higher and the 200 diffraction line to lower diffraction angles; thus, the spacing between the 111 and 200 reflection lines decreases with increasing stacking fault probability [32]:

$$\Delta(2\theta_{200} - 2\theta_{111})(^\circ) = -45\sqrt{3} \frac{2\tan\theta_{200} + \tan\theta_{111}}{2\pi^2} \alpha \quad (4.1.)$$

After determination of the stacking fault probability α on the basis of Eq. (4.1.), the positions of seven diffraction lines (111, 200, 220, 311, 222, 331, and 420) investigated were corrected for peak shift induced by the presence of stacking faults according to:

$$\Delta(2\theta) = \pm \tan\theta \cos^2 \Phi 270 \frac{\sqrt{3}\alpha}{\pi^2 h_3} \quad (4.2.)$$

where Φ is the angle between the normal of the diffracting plane and the planes containing the deformation faults, α is the stacking fault probability (assumed to be small in the present treatment) and $h_3 = |h + k + l|$. The diffraction-line shift is positive or negative, depending on whether h_3 is $3n+1$ or $3n-1$ (n is an integer); when $h_3=3n$ there is no shift.

After having performed the correction for peaks shifts induced by stacking faults, the offset of the diffraction-angle scale was corrected. As the measurements of the nanocrystalline Ni powder specimens were carried out over an extended period of time, small changes of the offset might have occurred over this time period. For a rigorous correction of a possible instrumental offset of the diffraction-angle scale, a Nelson-Riley plot (i.e. a plot of the lattice parameter determined from individual reflections versus $\cos^2 \theta / \sin \theta$) [33] was made and the lattice parameter was determined from the intercept of the ordinate in the Nelson-Riley plot. As an alternative to the Nelson-Riley extrapolation for determination of the lattice parameter, a simultaneous least-squares refinement of the lattice parameter and the offset of the diffraction-angle scale was performed employing seven different hkl reflections. These two procedures led to identical results for the lattice parameter within experimental accuracy.

The crystallite sizes were evaluated employing the single-line broadening analysis applied to the 111 reflections [34-35]. Assuming that the Cauchy component of the structurally broadened profile is due to the small crystallite size and that the

Gaussian component of the structurally broadened profile, f , is due to microstrain, the crystallite size, D , and the microstrain, e , can be obtained from:

$$\beta_{f,c} = \frac{K\lambda}{D\cos\theta_0} \quad (4.3.)$$

$$\beta_{f,g} = 4e\tan\theta_0 \quad (4.4.)$$

where $\beta_{f,c}$ and $\beta_{f,g}$ are the integral breadths of the Cauchy- and Gaussian components of the structurally broadened profiles, the size value, D , is the volume-weighted domain size in the direction parallel to the diffraction vector, λ is the wavelength and θ_0 is the position of the diffraction-line maximum. The shape factor, K , used in this work was set to equal to unity. In order to determine the instrumentally broadened profile of the diffractometer as function of diffraction angle 2θ , 13 hkl reflections of the LaB₆ (NIST SRM660a) standard powder sample were measured (see above). The integral breadths and the Voigt parameters [35] of the instrumental profile at the diffraction angles of the Ni 111 reflections were then determined by interpolation. More sophisticated methods for the analysis of the diffraction-line broadening exist [36]. However, the single-line method can be employed relatively easily and rapidly (as only one particular diffraction line has to be recorded) to obtain estimates for the size of the coherently diffracting domains D and the microstrain ε and is, in particular, useful to observe the evolution of these parameters *in-situ* as function of temperature. For the Ni thin films, the crystallite size was measured in the direction inclined at $\psi = 70.53^\circ$ with respect to the film normal.

4.3. Results

4.3.1. Microstructure of the Ni layer

A cross-sectional bright-field transmission electron micrograph of an as-deposited Ni layer is shown in Fig. 4.1. The thickness of the deposited Ni layer is about 50 nm. The interface between the Ni layer and the amorphous substrate is clearly visible and very sharp. The Ni layer is composed of both columnar and equiaxed crystallites exhibiting sizes of less than 20 nm. The strain-induced contrast variations indicate the presence of a considerable density of crystal defects. The layer is closed and exhibits a very homogenous thickness. Atomic force microscopy investigations of an even thinner (20 nm thick) Ni layer revealed that even this considerably thinner layer is fully closed and exhibits only a small surface roughness (see Fig. 4.2).

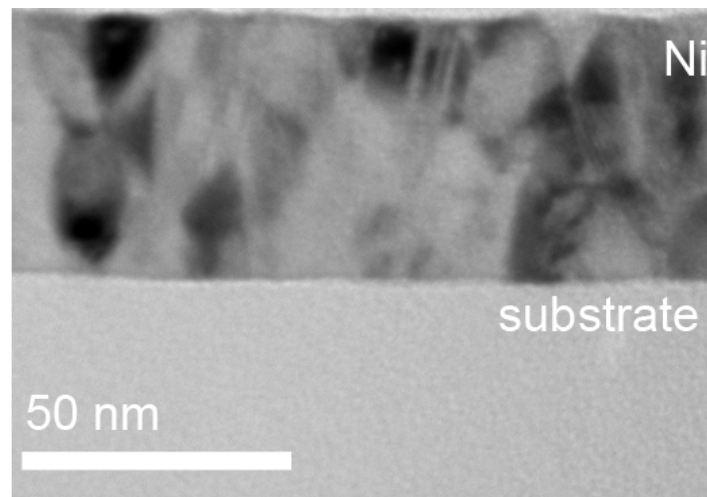


Fig. 4.1. Bright field transmission electron micrograph of the cross-section of the 50 nm thick Ni single layer after deposition by magnetron sputtering.

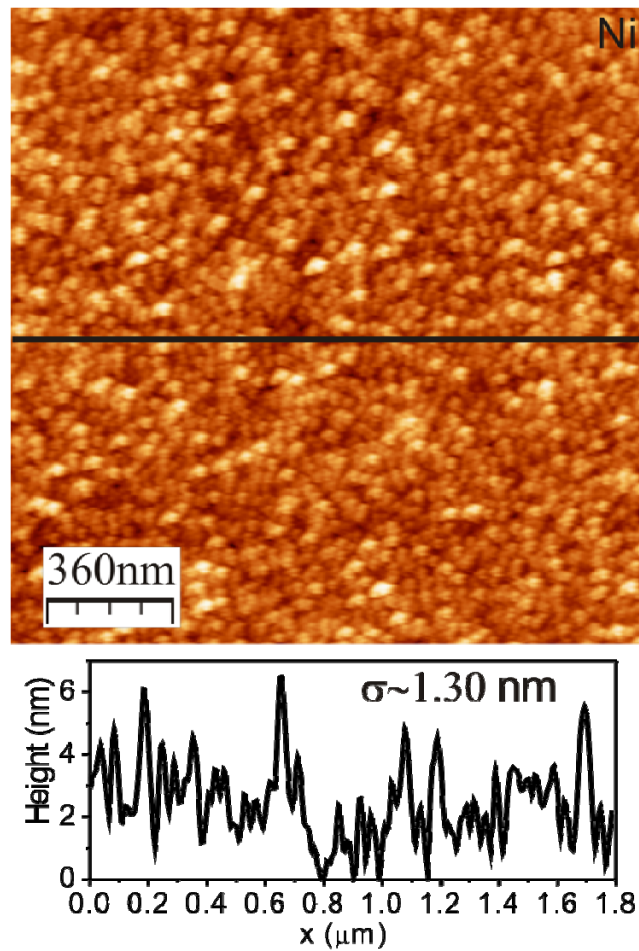


Fig. 4.2. Topographic image of the 20 nm thick Ni film recorded by atomic force microscopy (AFM). The black line indicates the position of the line scan shown at the bottom of the figure; the corresponding root-mean-square roughness equals about 1.30 nm.

The crystallographic texture of the thin Ni film was analyzed on the basis of $\theta/2\theta$ -scans (with the diffraction vector oriented parallel to the specimen-surface normal). $\{111\}$ pole figures and $\{111\}$ pole figure sections (i.e. plots of the diffraction-line intensity versus the inclination angle of the diffraction vector with respect to the surface normal ψ) were determined. In a $\theta/2\theta$ -scan, only the Ni 111 and 222

reflections appear (see Fig. 4.3a). This indicates the occurrence of a very strong and sharp texture with the $\{111\}$ planes oriented parallel to the surface; the $\{111\}$ pole-figure indicates a $\{111\}$ fibre texture (Fig. 4.3b). The full width at half maximum (FWHM) of the $\{111\}$ pole maximum, deduced from the pole figure section, is about 5° (Fig. 4.3c). These results justify the use of the crystallite group method (cf. Section 4.2.3) for diffraction-stress analysis.

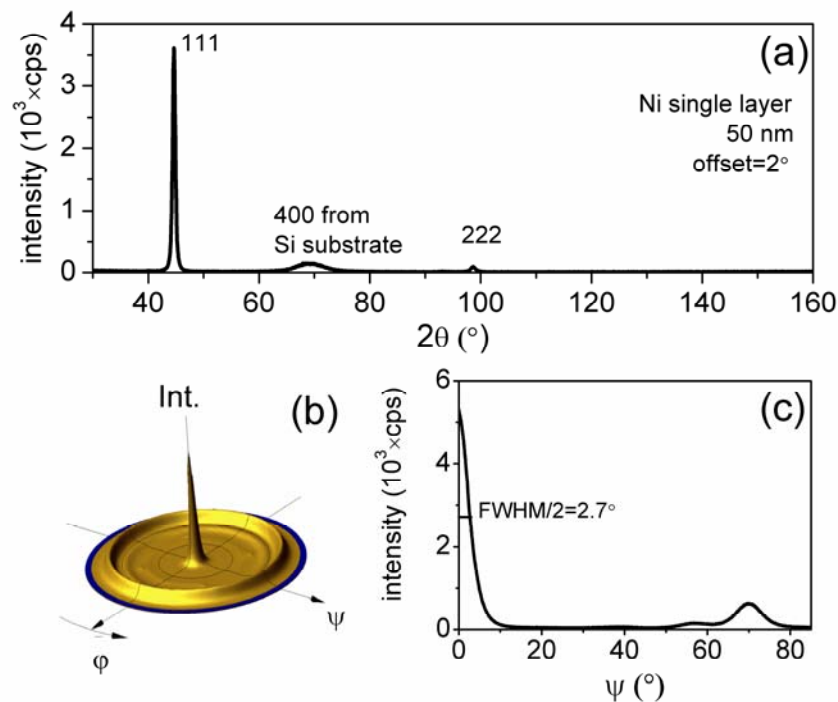


Fig. 4.3. Crystallographic texture of as-deposited Ni single layer (50 nm thick). (a) $\theta/2\theta$ -scan (with an offset of 2° from the symmetrical diffraction geometry, to avoid a too high intensity from the 400 reflection of the single-crystalline (100)-oriented Si substrate), (b) 111 pole figure, and (c) ψ -scan (pole figure section) recorded employing the 111 reflection.

4.3.2. Non-monotonic size-dependence of the lattice parameter of Ni thin film

Upon annealing the 50 nm thick Ni single layer with an initial crystallite size of 15 nm, the crystallite size increases. The corresponding values of the strain-free lattice parameter are shown in Fig. 4.4 as function of the inverse of the crystallite size. A non-monotonic variation is observed: after an initial decrease of the lattice parameter with decreasing crystallite size, a subsequent increase of the lattice parameter with decreasing crystallite size is observed below a crystallite size of about 45 nm.

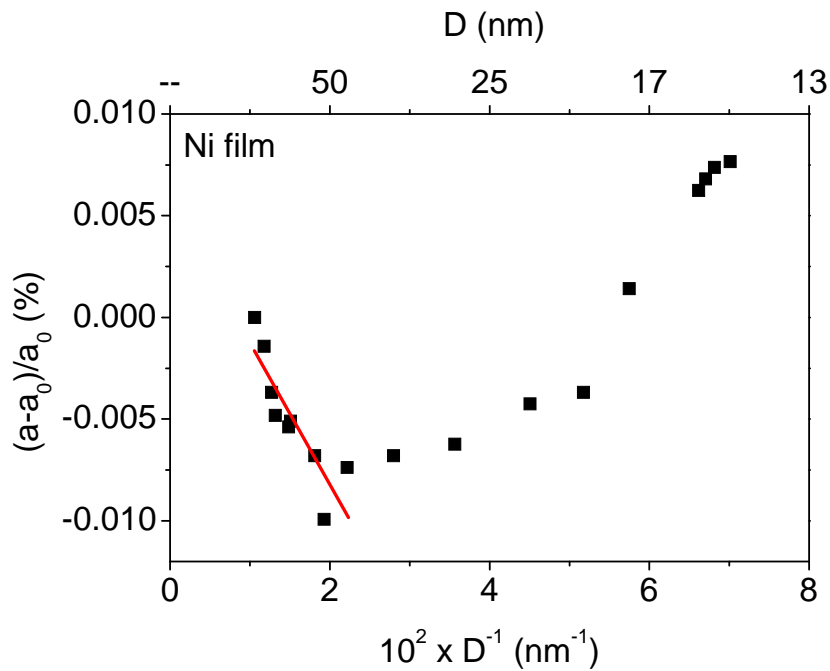


Fig. 4.4. Fractional change of the strain-free lattice parameter, $(a-a_0)/a_0$, (a_0 is the value obtained for the specimen exhibiting the largest crystallite size) as function of reciprocal crystallite size, D^{-1} , as measured for the 50 nm thick Ni single layer upon loop annealing up to 450°C under vacuum. The linear part of the measured lattice parameters plotted versus the reciprocal crystallite size has been fitted for evaluating interface stress of nanocrystalline Ni.

4.3.3. Microstructure of the ball-milled Ni powder

The microstructure of a Ni powder specimen ball-milled for 5 h was investigated by transmission electron microscopy before and after annealing at 325°C for 200 h (see Fig. 4.5). For the as-milled specimen, the analysis of a number of micrographs (see e.g. Fig. 4.5a) indicated that the crystallite sizes are of the order of 30 nm. This result is compatible with the crystallite-size data obtained from the X-ray diffraction line broadening analysis (see Fig. 4.6). The distinct dark contrast variations in the bright field TEM micrograph indicate a high density of crystal defects. The grains shown in Fig. 4.5a have a slightly elongated shape, which may be characteristic for the initial state of ball milling pertaining to Fig. 4.5a: plastic deformation upon trapping of a (not yet deformed) powder particle between milling balls and/or a ball and the wall would result in a flattening of the grains perpendicular to the direction of the impact.

Upon ball-milling, the crystallite size of the Ni powder decreases rapidly down to about 30 nm within about 1 hour of milling time and then continues to decrease at a lower rate down to about 18 nm followed by a steady state for milling times larger than 30 hours (see the open circles in Fig. 4.6). The microstrain increases steadily with increasing milling time (see the black squares in Fig. 4.6), indicating an increasing amount of crystal imperfection with increasing milling time.

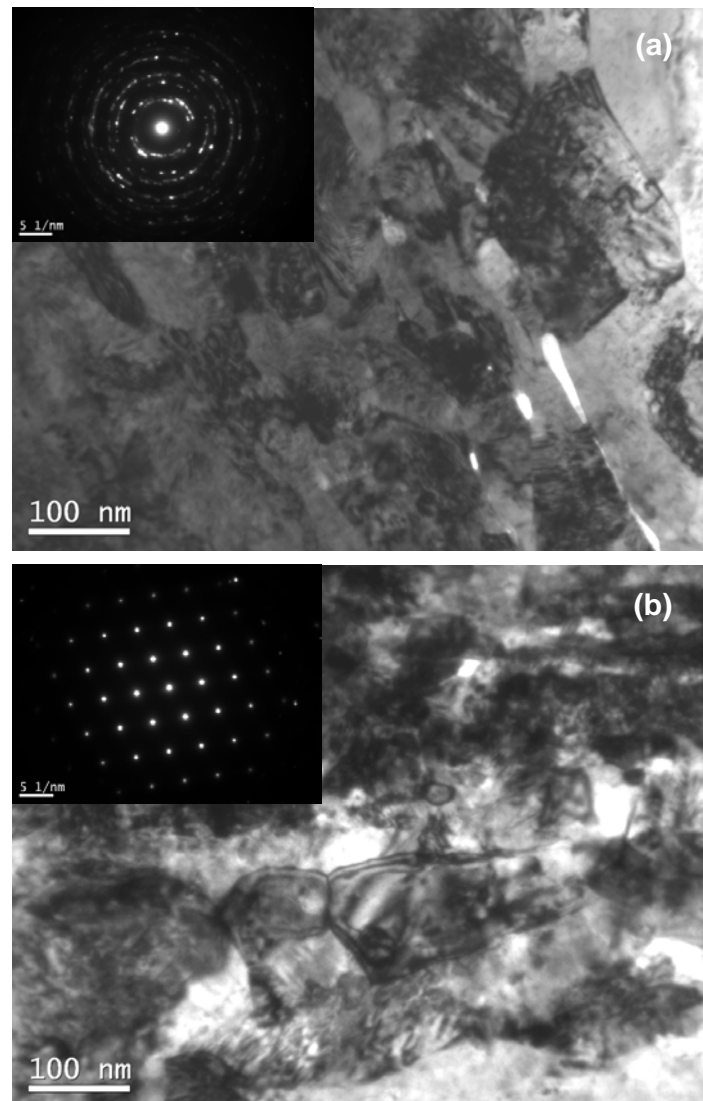


Fig. 4.5. Bright-field transmission electron micrographs of the Ni powder after ball-milling for 5 h, (a) as-milled and (b) after a subsequent annealing at 325°C for 200 h. The insets show the corresponding selected area diffraction patterns (SADPs) of [110] zone axis.

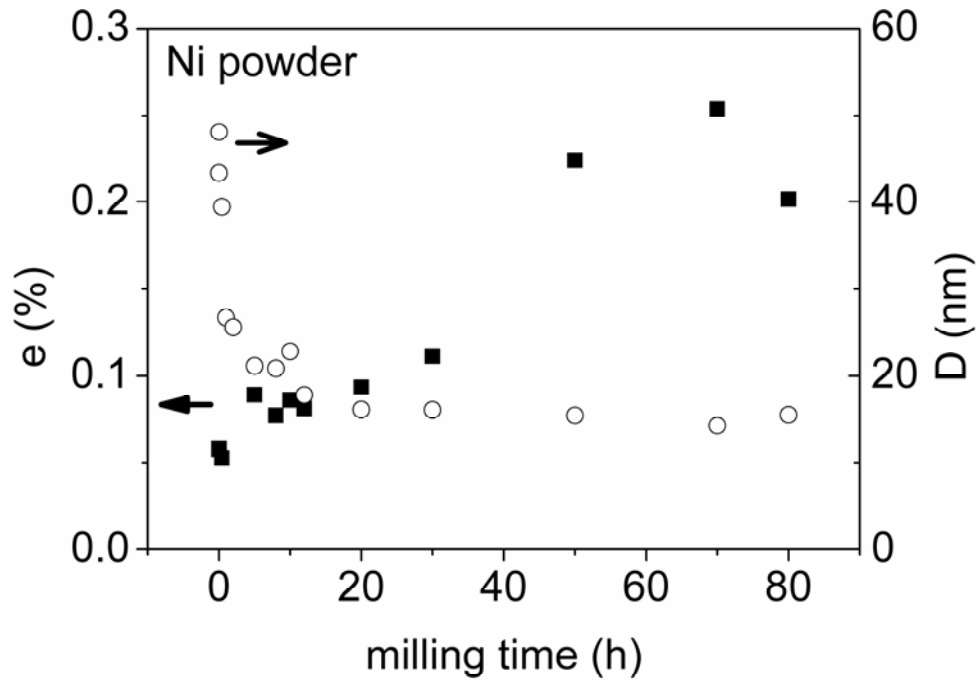


Fig. 4.6. Microstrain (black squares) and the crystallite size (open circles) of the Ni powder as function of ball-milling time.

The stacking fault probability, α , is shown in Fig. 4.7 as function of ball-milling time. With increasing milling time, the stacking fault probability increases from about 0.2% up to 0.6%. This result is in line with previous data for severely plastically deformed metals (as filed [37] and ground [38] metals).

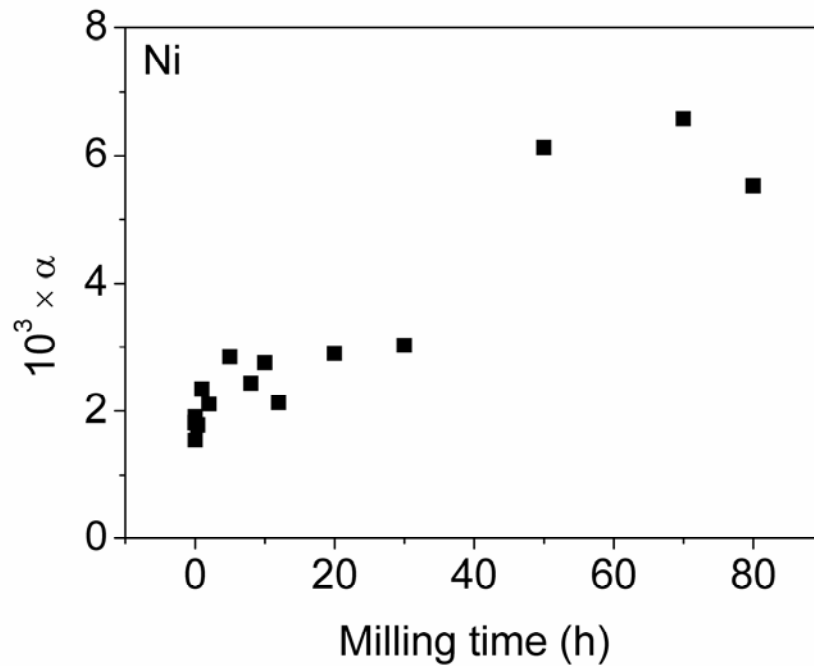


Fig. 4.7. Variation of the stacking fault probability, α , of the Ni powder as function of ball-milling time.

For the milled specimen subjected to annealing at 325°C for 200 hours under (N_2+H_2) atmosphere, considerable grain growth had occurred. Based on analysis of a number of micrographs as Fig. 4.5b, it follows that the crystallite size after annealing equals about 100 nm. The electron micrographs indicate that a considerable density of crystal defects still exist after the annealing.

4.3.4. Non-monotonic size-dependence of the lattice parameters of Ni powder

The lattice parameter of unmilled, ball-milled, and ball-milled and annealed Ni powders has been plotted as function of the reciprocal of the crystallite size in Fig. 4.8.

As observed for the thin Ni film (Fig. 4.4), a non-monotonic variation is observed: with decreasing crystallite size, the lattice parameter first decreases and below a crystallite size of about 25 nm, the lattice parameter increases.

4.4. Discussion

It has been shown in this work that, independent of the process applied to produce nanocrystalline nickel, the lattice parameter of nanocrystalline Ni upon decreasing crystallite size first exhibits a contraction and subsequently an expansion. Such contraction-expansion behavior has not been observed before. The contraction-expansion transition occurs at a “critical” crystallite size of about 45 nm for the nanocrystalline Ni prepared as a film by vapor deposition and at a crystallite size of about 25 nm for the nanocrystalline Ni prepared by ball milling. Upon decreasing crystallite size down to the “critical” size, the fractional change (contraction) of the lattice parameter equals about -0.01%.

(Surface and) Interface stresses have been proposed as causes for lattice-parameter contraction for nanocrystalline materials [8]. The lattice contraction induced by interface stress can be expressed as [20]:

$$\frac{a - a_0}{a_0} = -\frac{4}{3K} \sigma_s \frac{1}{D} \quad (4.5.)$$

where $(a-a_0)/a_0$, K , σ_s , and D are the relative change of the lattice constant, the bulk modulus, the interface stress, and the volume-weighted crystallite size, respectively. Hence, the interface stress can be determined from the slope of the straight line fitted to the data in a plot of the fractional lattice-parameter change (contraction) vs. reciprocal crystallite size.

The evaluation of the interface stress of Ni by fitting such a straight line to the more or less linear, fractional decrease of the lattice parameter as function of the reciprocal crystallite size up till the “critical” crystallite size (cf. Figs. 4.4 and 4.8) yields interface-stress values of (0.93 ± 0.19) N/m, and (0.41 ± 0.05) N/m for the Ni thin film and the Ni powder, respectively. Such interface-stress values are in the expected range for an fcc metal [19].

Lattice expansion of Ni occurs for decreasing crystallite size beyond the “critical” crystallite size (Figs. 4.4 and 4.8). Lattice expansion (only) has been reported before for nanocrystalline Ni powder and has been attributed to a decrease of intracrystalline pressure resulting from the electrostatic interaction of ions and electrons in the metal lattice [6-7].

It is suggested here that the contraction-expansion transition occurring for ferromagnetic Ni may be caused by a magnetic multi domain-single domain transition at a “critical size” value, which is a well-known phenomenon for ferromagnetic materials as Ni, Co and Fe [39]. Upon the transition from a multidomain to a single domain microstructure the spin directions within a grain, departing from a more or less random distribution, become uniformly oriented. The multi domain-single domain transition occurs at about 42 nm for a spherical Ni particle according to Refs. [40-41], which value indeed is in the range of “critical size” values observed in this study for the contraction-expansion transition.

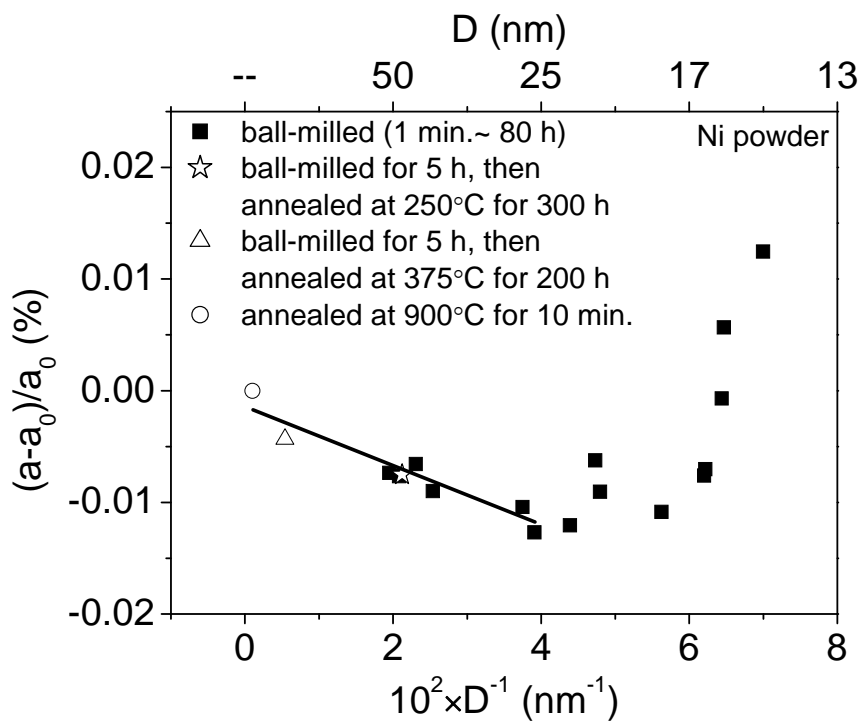


Fig. 4.8. Fractional change of the strain-free lattice parameter, $(a-a_0)/a_0$, (a_0 is the lattice parameter obtained for the as-received Ni powder after annealing at 900°C for 10 min) as function of the reciprocal crystallite size, D^{-1} , as measured from the Ni powder after ball-milling (black squares) and subsequent annealing at different temperatures and durations (open symbols as indicated in the legend). The linear part of the measured lattice parameters plotted versus the reciprocal crystallite size has been fitted for evaluating interface stress of nanocrystalline Ni.

4.5. Conclusion

- The (strain-free) lattice parameter of nanocrystalline Ni reveals a strikingly non-monotonic variation with decreasing crystallite size: first a decrease, then an increase upon decreasing crystallite size. This unusual behaviour has been established both for nanocrystalline Ni thin films prepared by physical vapour deposition and for nanocrystalline Ni powders prepared by ball milling.
- The decrease of the lattice parameter upon decreasing crystallite size, until a “critical size” value is reached, is ascribed to interface stress induced contraction. The interface stress values deduced quantitatively from the measured data are of the order 1 N/m, as expected for fcc metals.
- The increase of the lattice parameter upon decreasing crystallite size below the “critical size” is ascribed to a multidomain to single domain transition in a single Ni grain occurring at a “critical size” value. The “critical size” values reported in the literature are in the range of “critical size” values found in this work for the multidomain-single domain transition.

Acknowledgement

The authors are grateful to Dr. Z. M. Wang for fruitful discussion, to Dr. E. Bischoff and Mr. W.D. Lang for TEM analysis and sample preparation, respectively, and to Mr. F. Thiele (Max Planck Institute for Metals Research) for specimen fabrication.

References

- [1] Kuru Y, Wohlschlägel M, Welzel U, Mittemeijer EJ. *Appl. Phys. Lett.* 2007;90:243113.
- [2] Chen CQ, Shi Y, Zhang YS, Zhu J, Yan YJ. *Phys. Rev. Lett.* 2006;96.
- [3] Zhong WH, Sun CQ, Li S. *Solid State Commun.* 2004;130:603.
- [4] Gleiter H. *Acta Mater.* 2000;48:1.
- [5] Boswell FWC. *Proc. Phys. Soc. London, Sect. A* 1951;64:465.
- [6] Gamarnik MY. *Phys. Status Solidi B* 1991;168:389.
- [7] Gamarnik MY. *Phys. Status Solidi B* 1991;164:107.
- [8] Vermaak JS, Mays CW, Kuhlmann D. *Surf. Sci.* 1968;12:128.
- [9] Lu K, Sui ML. *Scripta Metall. Mater.* 1993;28:1465.
- [10] Lu K, Sun NX. *Philos. Mag. Lett.* 1997;75:389.
- [11] Qin W, Chen ZH, Huang PY, Zhuang YH. *J. Alloys Compd.* 1999;292:230.
- [12] Perebeinos V, Chan SW, Zhang F. *Solid State Commun.* 2002;123:295.
- [13] Kittel C. *Introduction to solid state physics.* New York, London, Sydney: John Wiley & Sons, Inc., 1968.
- [14] Apai G, Hamilton JF, Stohr J, Thompson A. *Phys. Rev. Lett.* 1979;43:165.
- [15] Mays CW, Vermaak JS, Kuhlmann D. *Surf. Sci.* 1968;12:134.
- [16] Yu XF, Liu X, Zhang K, Hu ZQ. *J. Phys.: Condens. Matter* 1999;11:937.
- [17] Chatterjee PP, Pabi SK, Manna I. *J. Appl. Phys.* 1999;86:5912.
- [18] Wang ZM, Wang JY, Jeurgens LPH, Phillip F, Mittemeijer EJ. *Acta Mater.* 2008;56:5047.
- [19] Birringer R, Zimmer P. *Acta Mater.* 2009;57:1703.
- [20] Lamparter P, Mittemeijer EJ. *Int. J. Mat. Res.* 2007;98:485.
- [21] Liu XD, Zhang HY, Lu K, Hu ZQ. *J. Phys.: Condens. Matter* 1994;6:L497.

- [22] Okram GS, Devi KN, Sanatombi H, Soni A, Ganesan V, Phase DM. J. Nanosci. Nanotechno. 2008;8:4127.
- [23] Heinemann K, Poppa H. Surf. Sci. 1985;156:265.
- [24] Palosz B, Stelmakh S, Grzanka E, Gierlotka S, Palosz W. Z. Kristallogr. 2007;222:580.
- [25] Strecker A, Bader U, Kelsch M, Salzberger U, Sycha M, Gao M, Richter G, van Benthem K. Z. Metallkd. 2003;94:290.
- [26] Prenitzer BI, Giannuzzi LA, Newman K, Brown SR, Irwin RB, Shofner TL, Stevie FA. Metall. Mater. Trans. A 1998;29:2399.
- [27] ProFit for Windows User's Guide: Philips Analytical X-ray, 1996.
- [28] Welzel U, Mittemeijer EJ. Mater. Sci. Forum 2004;443-444:131.
- [29] Welzel U, Ligot J, Lamparter P, Vermeulen AC, Mittemeijer EJ. J. Appl. Cryst. 2005;38:1.
- [30] Paterson MS. J. Appl. Phys. 1952;23:805.
- [31] Velterop L, Delhez R, de Keijser TH, Mittemeijer EJ, Reefman D. J. Appl. Crystallogr. 2000;33:296.
- [32] Warren BE. X-ray diffraction. New York: Addison-Wesley, 1990.
- [33] Klug HP, Alexander LE. John Wiley and Sons, New York 1974:643.
- [34] Delhez R, de Keijser TH, Mittemeijer EJ. Fresenius Zeitschrift Für Analytische Chemie 1982;312:1.
- [35] Keijser THd, Langford JI, Mittemeijer EJ, Vogels ABP. J. Appl. Cryst. 1982;15:308.
- [36] Mittemeijer EJ, Welzel U. Z. Kristall. 2008;223:552.
- [37] Smallman RE, Westmacott KH. Philos. Mag. 1957;2:669.
- [38] Nakajima K, Okada K, Koda S. J. Phys. Soc. Jpn. 1964;19:2356.

- [39] Cullity BD, Graham CD. Introduction to Magnetic Materials: Wiley-IEEE Press, 2008.
- [40] Kitakami O, Sakurai T, Miyashita Y, Takeno Y, Shimada Y, Takano H, Awano H, Ando K, Sugita Y. Jpn. J. Appl. Phys. Part 1 1996;35:1724.
- [41] Brown WF. Phys. Rev. 1957;105:1479.

5. Summary

Residual, mechanical stresses in thin films are of great importance for the reliability and performance of film systems in technological applications [1-2]. The residual stresses can be due to the deposition process, the mismatch of the coefficients of thermal expansion of the thin film(s) and the substrate upon cooling or heating (thermal stresses), interdiffusion (differences in the molar volumes and differences in the atomic fluxes of the diffusing species), (continued) grain growth, excess vacancy annihilation and shrinkage of grain-boundary voids, phase formation, and plastic deformation (yielding; creep) [3]. Interdiffusion and phase transformations in thin films can occur at much lower temperatures as compared to bulk diffusion couples due to the presence of a high density of defects and grain boundaries and can thus lead to pronounced changes of the state of stress already at comparatively low annealing temperatures (see, for example, Ref. [4] and references therein). Chapter 2 of this thesis addresses in particular the relationship between stresses and diffusion in nanocrystalline Ni-Cu thin films. Interdiffusion and the stress evolution in thin bilayer (individual layer thickness: 50 nm) diffusion couples of Cu and Ni have been investigated employing Auger-electron spectroscopy in combination with sputter-depth profiling and ex-situ and in-situ X-ray diffraction measurements. In addition, single layers of Ni and Cu have been investigated. The specific residual stresses that emerge due to diffusion between the (sub)layers in the bilayer could then be identified by comparing the stress changes in the bilayer system with corresponding results obtained for single layers of the components in the bilayer system under identical conditions.

Stresses can also be due to an extra pressure in nanocrystalline materials due to surface (or interface) stress [5]: Based on the concept of the Laplace pressure at the concave side of a surface or interface, a decrease of the lattice parameter(s) with decreasing crystallite size is expected. Although the size dependence of the crystal-lattice parameter(s) has been frequently investigated since the 1950's, the experimental and theoretical results obtained until now are inconclusive (for details and references, see Chapter 4): With decreasing crystallite size, the lattice parameters of nanocrystalline materials can, apparently, both contract and expand. Moreover,

inconsistent experimental results have been reported. A non-monotonic change (i.e., first lattice contraction and later lattice expansion) of the lattice parameter with respect to crystallite size was observed in this work both for Ni thin films and ball-milled Ni powders for the first time employing *in-situ* X-ray diffraction measurements. The change of spin interaction in ferromagnetic material (as Ni, for crystallite size below a certain threshold) during the transition from a multidomain to a single domain structure may cause this abnormal phenomenon of lattice expansion. These results are discussed in the light of different models describing the crystallite-size dependence of the lattice parameters.

Interdiffusion, solid solution formation and stress development in thin-film Ni-Cu diffusion couples – Chapter 2

Thin bi-layer (individual layer thickness: 50 nm) diffusion couples of Cu and Ni were prepared by direct-current magnetron sputtering on silicon substrates covered with amorphous layers of Si₃N₄ and SiO₂ (each 50 nm thick) as barrier layers to prevent diffusion between the bottom Cu layer and the substrate. To decrease the defect density in the Cu sublayer, a pre-annealing treatment was applied to some of the specimens: The Cu sublayer was annealed at 500°C for 3 hours and cooled back to ambient temperature after its deposition without breaking the vacuum (called 'pre-annealed condition' in the following). Thereafter, the Ni layer was deposited. The formation and the decomposition of the (Cu,Ni) solid solution, interdiffusion, stress evolution and the microstructural evolution upon annealing have been investigated employing Auger-electron spectroscopy in combination with sputter-depth profiling, transmission electron microscopy, *ex-situ* X-ray diffraction phase and texture measurements and *in-situ* X-ray diffraction stress measurements. Moreover, single layers of Ni and Cu were prepared under identical deposition conditions for identifying the stress contributions related to interdiffusion at elevated temperatures.

Microstructural investigations by transmission electron microscopy and X-ray diffraction line broadening analysis revealed that a columnar microstructure (columns traversing the entire sublayer) prevails in both sublayers, with a somewhat more irregular microstructure in some portions of the Cu sublayer. For the as-prepared PA specimens, the lateral crystallite sizes are considerably larger than for the as-

Summary

prepared ND specimens (ND: 20 nm for Cu, 15 nm for Ni; PA: 80 nm for Cu, 25 nm for Ni; all measured at $\psi = 70.5^\circ$). It is worth noting that the pre-annealing of the Cu bottom layer affects also the microstructure of the Ni top layer.

The concentration-depth profiles of Ni normally deposited (ND) and pre-annealed (PA) Ni-Cu diffusion couples annealed at temperatures of 225°C and 300°C are shown in Fig. 5.1a,b.

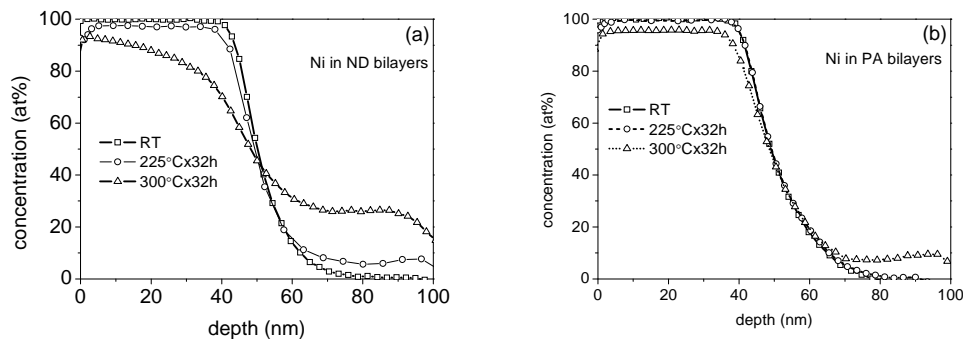


Fig. 5.1. Depth profiles of (a) normally deposited (ND) and (b) pre-annealed (PA) Ni(top)-Cu(bottom) bilayer diffusion couples after isothermal annealing at temperature of 225°C and 300°C for 32 hours in comparison with dept profiles of as-dept bilayers at room temperature (RT).

After annealing a ND diffusion couple at 225°C for 32 hours, the depth profile shows a change of the concentration slope at the position of the initial interface and the emergence of a plateau region of considerable Ni concentration in the initially pure Cu sublayer (see Fig. 5.1a). The height of this Ni plateau in the Cu sublayer of the ND specimen increases significantly when the annealing temperature increases from 225°C to 300°C. Whereas the change of the slope at the position of the initial interface is due to the volume diffusion across the initial interface, the plateau region on the Cu-rich side of the couple is the result of Ni diffusion through Cu grain boundaries, oriented more or less perpendicularly to the original interface (columnar grains), accompanied with sideways Ni volume diffusion from the Cu grain boundaries through the Cu grains. On the initially Ni-rich side of the ND couple, a distinct Cu plateau hardly develops upon annealing at 225°C or even at 300°C (Fig. 5.1a): The concentration profile is dominated by volume diffusion across the original interface. However, a significant Cu concentration occurs at the surface of the

bilayer specimen. This implies that sideways Cu diffusion from the Ni grain boundaries through the columnar Ni grains is limited. This is likely a consequence of the concentration-dependence of the interdiffusion coefficient in the Cu/Ni system: the interdiffusion coefficient is pronouncedly smaller at high Ni concentration [6-7].

The extent of diffusion intermixing at a given annealing condition is much less pronounced for a pre-annealed (PA) diffusion couple: See Fig. 5.1b. The concentration slope at the position of the initial interface changes only slightly even after annealing at a relatively high temperature of 300°C. This is a consequence of very limited volume diffusion across the initial interface due to a reduced density of crystalline defects accelerating volume diffusion (as compared to the ND specimens). The plateau concentrations of Ni and Cu in the initially pure Cu and Ni sublayers, respectively, are significantly lower for the PA diffusion couples as compared to the ND diffusion couples (compare Fig. 5.1a and 5.1b). This effect is a direct consequence of the drastically reduced grain-boundary density in the PA Cu layer as compared to the ND Cu layer.

For an in-situ thermal treatment employed for tracking the stress evolution employing in-situ X-ray diffraction stress measurements, the complete temperature cycle consists of three segments, namely heating from 30°C (ambient temperature in the diffractometer) to the annealing temperature, isothermal annealing, and cooling back to ambient temperature.

The specific residual stresses that emerge due to diffusion between the (sub)layers in the bilayer can be identified by comparing the stress changes in the bilayer system with corresponding results obtained for single layers of the components in the bilayer system under identical conditions. After subtraction of the thermal stress contribution developing upon heating it follows that significant tensile stress contributions occur for both sublayers of the ND bilayer and for the single layers (see Figs. 5.2a, b). Thus, apart from thermal misfit as a source of stresses, other stress-generating/relaxing mechanisms must be operative upon heating: The relaxation of compressive thermal stresses due to plastic yielding and the generation of tensile stresses upon heating a layer sputter-deposited at ambient temperature due to the thermally activated compaction of material as a consequence of grain growth can be considered as possible sources of stress generation.

Summary

Analysis of the crystallite sizes, as obtained by X-ray diffraction line broadening analysis, during heating up to the annealing temperature, isothermal annealing and cooling indeed reveals that substantial grain growth indeed occurs during heating up to the annealing temperature. The stress evolution of the sublayers in the ND bilayer and the single layers exhibits almost identical evolutions during heating (Figs. 5.2a, b). Hence, it is very likely that grain growth (possibly in association with defect annihilation) is the dominant source of the tensile stress contributions developing during heating of the sublayers and the single layers.

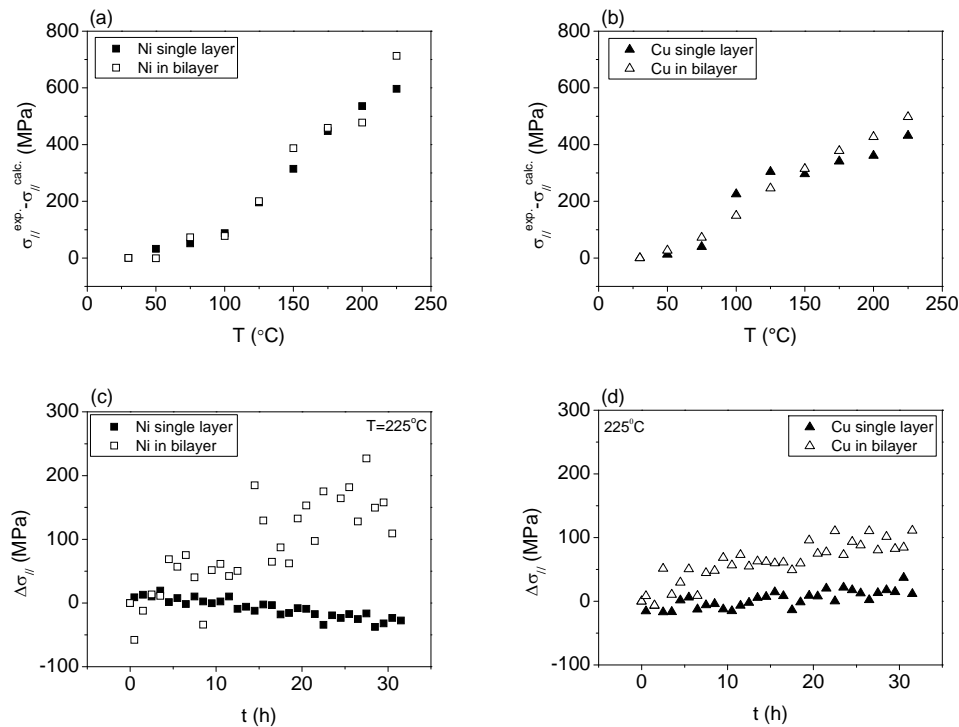


Fig. 5.2. Experimentally determined stress minus the expected thermal stress contribution developing during heating to the annealing temperature as function of temperature for (a) the Ni single layer and the Ni sublayer of the normally deposited bilayer, (b) the Cu single layer and the Cu sublayer of the normally deposited bilayer. Stress changes during annealing as function of time for (c) the Ni single layer and the Ni sublayer of the normally deposited bilayer, (d) the Cu single layer and the Cu sublayer of the normally deposited bilayer.

Evidently, the stress of the single layers does not change distinctly during the isothermal anneal. Tensile stress contributions (200 MPa and 100 MPa for Ni and Cu sublayers, respectively) develop in the sublayers of the ND specimen, most pronouncedly in the Ni sublayer (Figs. 5.2c, d).

For the pre-annealed specimens, the crystallite sizes obtained by single-line broadening analysis are considerably larger prior to the diffusion anneal (ND: 20 nm for Cu, 15 nm for Ni; PA: 80 nm for Cu, 25 nm for Ni; all measured at $\psi = 70.5^\circ$). This makes plausible that distinct grain growth does not occur during heating of the pre-annealed specimen and that almost purely thermoelastic behavior thus prevails during heating, annealing and cooling (considering that the extent of interdiffusion is also very limited). The stress of the pre-annealed Cu sublayer remains constant because neither grain growth nor significant diffusion into this Cu sublayer occurs. The stress change in the Ni sublayer for the pre-annealed specimen is likely due to (marginal) grain growth during annealing (for further details, see Chapter 2).

The following mechanisms leading to stress change upon isothermal annealing can be conceived: (i) interdiffusion (differences in the molar volumes and differences in the atomic fluxes of the diffusing species), (ii) (continued) grain growth, (iii) excess vacancy annihilation and shrinkage of grain-boundary voids, and (iv) plastic deformation (yielding; creep). Whereas mechanisms (ii) and (iii) invariably generate tensile stresses, mechanism (iv) always leads to stress relaxation (i.e. a decrease of the stress level). For both sublayers of the ND specimen, mechanism (iv) is less likely due to the small stress level of the sublayers.

The influence of interdiffusion on the change of stress state in both sublayers can be understood as a competition between (a) stress generation due to a flux of Ni atoms diffused into the Cu sublayer not balanced by a flux of Cu atoms into the Ni layer and (b) stress generation due to the difference in molar volumes of Ni and Cu ($V_{\text{Ni}} = 6.59 \text{ cm}^3$; $V_{\text{Cu}} = 7.11 \text{ cm}^3$; cf. Chapter 2). The stress changes of the Ni sublayer and the Cu sublayer due to interdiffusion calculated from an approximate analysis (for details, see Chapter 2) indicate that the tensile stress generation in the Ni sublayer upon isothermal annealing at 225°C for 32 hours is likely due to interdiffusion. However, a tensile stress develops in the Cu sublayer during isothermal annealing (Fig. 5.2d), whereas a compressive stress distribution due to interdiffusion would be expected. Hence, mechanisms (ii) (grain growth) and/or mechanism (iii) (excess vacancy annihilation and shrinkage of grain-boundary voids) must be operative.

*Summary***Non-monotonic crystallite-size dependence of the lattice parameter of thin films of metals– Chapter 3**

Pure Cu, Ni and Pd thin films with thicknesses from 20 nm to 100 nm were prepared by direct current magnetron sputtering (base pressure about 5×10^{-8} mbar) onto Si (100) wafers covered with 50 nm SiO_2 and 50 nm Si_3N_4 barrier layers to prevent interdiffusion between the deposited layer and the substrate. Residual stresses (in-plane, biaxial and rotationally symmetric, as verified in this study; characterized by the symbol $\sigma_{//}$) and strain-free lattice parameters were measured by X-ray diffraction residual stress analyses. Crystallite sizes were evaluated employing single-line broadening analysis with the diffraction vector oriented nearly parallel to the specimen surface. A new approach, called “loop annealing”, was devised to investigate in-situ variations of the strain-free lattice parameters as function of crystallite size: The as-deposited specimens containing nano-sized crystallites are sequentially annealed isothermally at temperatures increasing with each step (‘loop’). After each anneal at a given temperature, the specimen is cooled back to room temperature for performing the X-ray diffraction measurement. For each annealing step, the specimen is heated isochronically (heating rate of 0.1 K/s) to the annealing temperature, which is maintained for five minutes. The cooling to room temperature has an undefined cooling rate, as the chamber used facilitates only free cooling (i.e. heat is removed only by thermal conduction to the surroundings of the heating chamber). This ‘loop annealing’ has two advantages: (i) Accurate knowledge of the coefficient of thermal expansion is not required, as all X-ray diffraction measurements are done at the same, ambient temperature (ii) The time required for investigating a certain range of crystallite sizes is drastically reduced as compared to ex-situ annealing of the specimens in a furnace, where each anneal at a certain temperature requires transferring the specimen from the diffractometer to the furnace and vice versa. One measurement at ambient temperature consists of two scans covering the angular range containing the 111 reflections at two tilt angles ($\psi = 0^\circ$ and $\psi = 70.53^\circ$) and takes less than half an hour including a waiting time of five minutes at ambient temperature to guarantee temperature homogenization and stability.

Both Cu and Pd exhibit a distinct lattice contraction with decreasing crystallite size (for details, see Chapter 3). A strikingly different result is obtained for Ni: With decreasing crystallite size, the strain-free lattice parameter first decreases and

subsequently shows a pronounced increase below a crystallite size of about 45 nm as shown in Fig. 5.3. The evaluation of the interface stress of Ni by fitting a straight line to the more or less linear, first part of the fractional change of the lattice parameter vs. reciprocal crystallite size yields a interface-stress value of (0.93 ± 0.19) N/m, which is comparable with values obtained for various metals (see Chapter 3). When the crystallite size of Ni decreases below 45 nm, a lattice expansion is observed. Lattice expansion (only) has been reported before for nanocrystalline Ni powder and has been attributed to the decrease of intracrystalline pressure resulting from the volume forces of electrostatic interaction of the ions and electrons in the metal lattice (see Chapter 3).

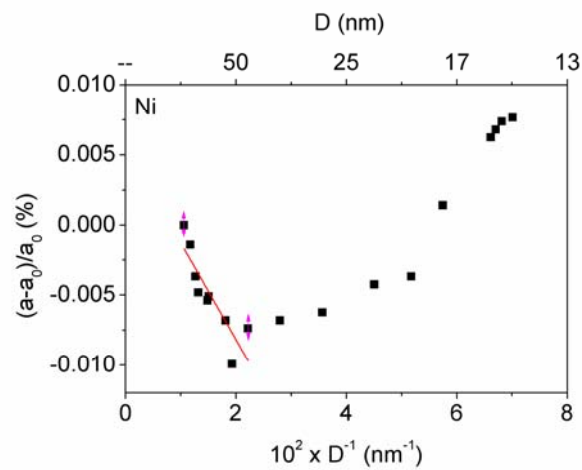


Fig. 5.3. Fractional change of the lattice parameter, $(a-a_0)/a_0$, (a_0 is the value obtained for the specimen exhibiting the largest crystallite size), of the 50 nm thick Ni single layer after loop annealing up to 450°C under vacuum as function of the reciprocal crystallite size, D^{-1} .

Here an alternative explanation for the contraction-expansion transition is offered: Ni is ferromagnetic. It is suggested here that the contraction-expansion transition occurring for ferromagnetic Ni may be caused by a magnetic multi domain-single domain transition at a “critical size” value, which is a well-known phenomenon for ferromagnetic materials as Ni, Co and Fe [8]. Upon the transition from a multidomain to a single domain microstructure the spin directions within a grain, departing from a more or less random distribution, become uniformly oriented. The multi domain-single domain transition occurs at about 42 nm for a spherical Ni

Summary

particle according to Refs. [9-10], which value indeed is in the range of “critical size” values observed in this study for the contraction-expansion transition.

The lattice parameter of nanocrystalline Ni as function of crystallite size – Chapter 4

Ni thin films of thickness 50 nm were prepared by direct current magnetron sputtering (base pressure about 5×10^{-8} mbar) onto Si (100) wafers covered with 50 nm SiO₂ and 50 nm Si₃N₄ barrier layers to prevent interdiffusion between the deposited layer and the substrate. Residual stresses (in-plane, biaxial and rotationally symmetric, as verified in this study; characterized by the symbol $\sigma_{//}$) and strain-free lattice parameters were measured by X-ray diffraction residual stress analyses. Crystallite sizes were evaluated employing single-line broadening analysis with the diffraction vector oriented nearly parallel to the specimen surface. The method of “loop annealing” was employed to investigate in-situ variations of the strain-free lattice parameters as function of crystallite size (see Chapter 4).

Ni powder (purity of 99.8 wt.-%) with a particle size of less than 50 μm was subjected to ball milling for durations of 1 min up to 80 h at room temperature in a planetary ball mill (Fritsch Pulverisette P6). A custom-made Ni milling case and Ni milling balls were used in order to avoid contamination of the powder with wear products from the milling case or the balls. The handling of the powders before milling and the sealing of the milling vessel were performed in a glove box under an Ar atmosphere. In order to produce Ni powders of different crystallite sizes, Ni powders milled for 5 hours were encapsulated in an evacuated quartz tube and annealed at temperatures between 250°C and 375°C in a furnace for various durations. Crystallite sizes were evaluated employing single-line broadening analysis. Lattice parameters were determined from measured diffraction line positions after correcting for instrumental aberrations and peak shifts due to stacking faults.

Upon ball-milling, the crystallite size of the Ni powder decreases rapidly down to about 30 nm within about 1 hour of milling time and then continues to decrease at a lower rate down to about 18 nm followed by a steady state for milling times larger

than 30 hours. The microstrain increases steadily with increasing milling time, indicating an increasing amount of crystal imperfections with increasing milling time.

The stacking fault probability of the ball-milled Ni powders continuously increases from about 0.2% up to 0.6% with increasing milling time up to 80 hours. After correcting for the effect of stacking faults and instrumental aberrations on diffraction line position, the fractional changes of the lattice parameter of the ball-milled Ni powder specimens subjected to different milling and annealing conditions have been plotted versus the reciprocal crystallite size in Fig. 5.4. The contraction-expansion transition observed for Ni thin films (see Fig. 5.3 and summary for Chapter 3) with decreasing crystallite size is confirmed by the results obtained for the Ni powders; also the values of the fractional change of the lattice parameters of the Ni thin films and the Ni powders agree very well. These findings confirm that the observed contraction-expansion transition is a genuine phenomenon of nanocrystalline Ni, which does not depend upon the method of preparation. For a discussion of the origin of the contraction-expansion transition, see Chapters 3 and 4 and English summary of Chapter 3 above.

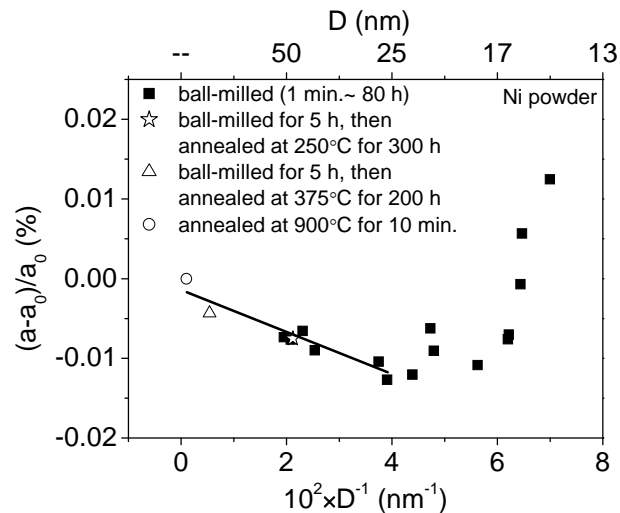


Fig. 5.4. Fractional change of the strain-free lattice parameter, $(a-a_0)/a_0$, (a_0 is the lattice parameter obtained for the as-received Ni powder after annealing at 900°C for 10 min) as function of the reciprocal crystallite size, D^{-1} , as measured from the Ni powder after ball-milling (black squares) and subsequent annealing at different temperatures and durations (open symbols as indicated in the legend). The linear part of the measured lattice parameters plotted versus the reciprocal crystallite size has been fitted for evaluating interface stress of nanocrystalline Ni.

6. Kurzfassung der Dissertation in deutscher Sprache

Mechanische Eigenspannungen in dünnen Schichten sind von großer Bedeutung für die Eigenschaften und die Zuverlässigkeit, z.B. für Anwendung in der Mikroelektronik [1]. Eigenspannungen können durch verschiedene Mechanismen verursacht bzw. beeinflusst werden (siehe Refs. [2-3]; für weitere Details, siehe auch Kapitel 1 – Einleitung): (i) Eigenspannungen können während der Schichtabscheidung entstehen (intrinsische Eigenspannungen); (ii) Unterschiede in den thermischen Ausdehnungskoeffizienten von Schicht und Substrat verursachen bei Temperaturänderungen Spannungen (thermische Spannungen); Interdiffusion und/oder Phasenumwandlungen können Spannungen verursachen; (iv) Kornwachstum und der Abbau von Defekten können zur Entstehung von Zugspannungen durch Volumenverringerung führen; (v) Plastische Deformation kann zum Abbau von Eigenspannungen führen.

Interdiffusion und Phasenumwandlungen, und damit einhergehend ausgeprägte Spannungsänderungen, können in dünnen Schichten schon bei vergleichsweise niedrigen Temperaturen auftreten, da dünne Schichten oft hohe Dichten von Korngrenzen und kristallinen Defekten aufweisen, die den Stofftransport begünstigen (siehe z.B. Ref. [4]; siehe auch Kapitel 2). Kapitel 2 ist deswegen insbesondere dem Einfluss von Interdiffusion auf den Spannungszustand von dünnen Cu-Ni Doppelschichten gewidmet. Zur Untersuchung wurden hier Auger-Elektronenspektroskopie (AES) in Kombination mit Sputter-Tiefenprofilanalyse, ex-situ und in-situ Röntgenbeugungsuntersuchungen und Transmissionselektronenmikroskopie (TEM) eingesetzt. Einzelne Ni und Cu Schichten wurden ebenfalls untersucht: Die durch Interdiffusion in den Doppelschichten verursachten Spannungsänderungen konnten durch Vergleich der Spannungsentwicklungen der Doppel- und Einzelschichten während der Wärmebehandlungen identifiziert werden.

Spannungen in nanokristallinen Materialien können auch durch einen zusätzlichen Druck auf Grund von Oberflächen- bzw. Grenzflächenspannungen verursacht werden [5]: Auf Grund einer Laplace-Spannung hinter der konkaven Seite einer Ober- bzw. Grenzfläche sind im inneren eines kleinen Partikels bzw. in einem nanokristallinen Korn Druckspannungen zu erwarten. Diese Druckspannungen können zu einer Abnahme des Gitterparameters führen. Obwohl der Einfluss der Kristallitgröße auf den Gitterparameter seit ca. 1950 ausgiebig untersucht wurde ergeben weder die experimentellen noch die theoretischen Untersuchungen ein klares Bild (für Details, siehe Kapitel 4): Es scheint, dass die Gitterparameter von nanokristallinen Materialien mit abnehmender Kristallitgröße sowohl zu als auch abnehmen können. In der vorliegenden Arbeit wurden die Gitterparameter von nanokristallinen Nickel-Schichten und Nickel-Pulvern ausführlich untersucht. Dabei kamen vor allem in-situ Röntgenbeugungsmessungen der Gitterparameter und der Kristallitgröße zur Anwendung. Es konnte gezeigt werden, dass der Gitterparameter von nanokristallinem Ni mit abnehmender Kristallitgröße zunächst abnimmt, unterhalb von einer Kristallitgröße von ca. 45 nm jedoch wieder zunimmt. Diese Beobachtung wird im Lichte verschiedener Modelle diskutiert.

Interdiffusion und Spannungsaufbau in Diffusionspaaren aus Ni-Cu Dünnschichten – Kapitel 2

In Kapitel 2 dieser Arbeit wurden Interdiffusion, Phasenbildung und Spannungsentwicklung in Diffusionspaaren aus dünnen Nickel/Kupfer Doppelschichten (Schichtdicke einer Einzelschicht 50 nm) mit Hilfe von *ex-situ* und *in-situ* Röntgenbeugungsuntersuchungen, Auger-Elektronenspektroskopie (AES), kombiniert mit Ionensputtern, und Transmissionselektronenmikroskopie (TEM) untersucht. Die Doppelschichten wurden durch DC-Magnetronspütern auf Si-Substrate, welche mit amorphen Zwischenschichten (Si_3N_4 und SiO_2) beschichtet waren, abgeschieden. Ni- und Cu-Einzelschichten, die unter identischen Bedingungen abgeschieden und wärmebehandelt wurden, wurden als Vergleichsproben verwendet um insbesondere Spannungen, die durch Diffusion hervorgerufen werden, zu identifizieren. Für einige Proben wurde die Cu-Schicht unmittelbar nach der Abscheidung einer Wärmebehandlung unterzogen (3 Stunden bei 500 °C;

vorbehandelte Proben); diese Vorbehandlung resultierte in einer Kornvergrößerung sowie einer Verringerung der Dichte von kristallinen Defekten.

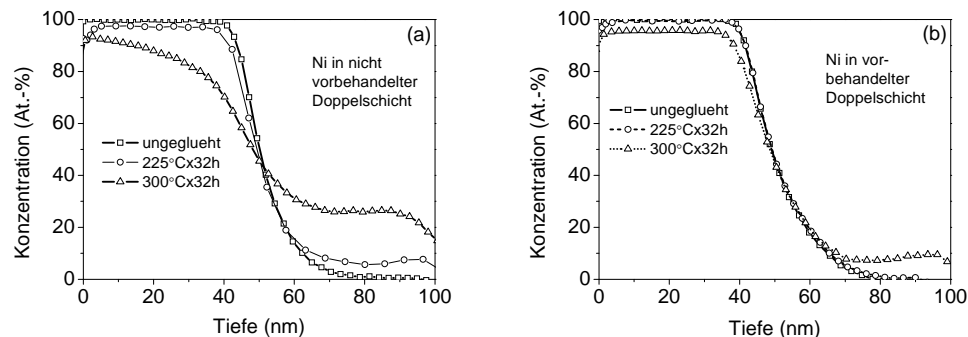


Abb. 6.1. Ni Tiefenprofile (ermittelt mit AES) für (a) normal hergestellte Ni(oben)-Cu(unten) Doppelschichten (b) vorbehandelte Ni(oben)-Cu(unten) Doppelschichten nach isothermen Wärmebehandlungen bei 225 °C und 300 °C für 32 Stunden. Zum Vergleich sind auch die Tiefenprofile der ungeglühten Proben dargestellt.

In Abb. 6.1 sind mit AES aufgezeichnete Zusammensetzungs-Tiefenprofile dargestellt. Bereits bei 225 °C tritt eine beträchtliche Vermischung der beiden Metallschichten durch Diffusion auf. Abgesehen von einer Veränderung der Steigung im Konzentrations-Tiefenprofil an der Stelle der ursprünglichen Grenzfläche zwischen den Schichten kann man in den Sputter-Tiefenprofilen der ausgelagerten Proben ein Konzentrationsplateau von Ni in Cu erkennen, innerhalb dessen die Ni-Konzentration mit der Auslagerungstemperatur zunimmt. Dieses Plateau entsteht durch die Diffusion von Ni durch die Cu-Korngrenzen gefolgt von Seitwärtsdiffusion von Ni aus der Korngrenze in die Cu-Körner (Untersuchungen mittels Transmissionselektronenmikroskopie ergaben, dass die Schichten im Wesentlichen eine kolumnare Mikrostruktur aufweisen). Andererseits sind Cu-Atome auf der Oberfläche der Ni-Schicht vorhanden, wohingegen sich jedoch kaum ein Cu-Plateaubereich in Ni ausbilden kann. Dies deutet darauf hin, dass in erheblichem Maße Korngrenzendiffusion von Cu in Ni auftritt, Volumendiffusion von Cu in Ni jedoch vernachlässigbar ist. Diese Beobachtung kann durch die Konzentrationsabhängigkeit der Diffusion verstanden werden: Der Interdiffusionskoeffizient nimmt mit zunehmender Ni-Konzentration ab [6-7].

Für die vorbehandelten Doppelschichten tritt bei gleichen Wärembehandlungen wesentlich weniger Interdiffusion auf: Die Plateau-Konzentrationen von Ni und Cu in den Cu- und Ni-Subschichten sind deutlich geringer als für die nicht vorbehandelten Proben. Dies ist auf eine deutlich verminderte Dichte von Korngrenzen in vor allem der vorbehandelten Cu-Schicht (aber auch der Ni- Schicht, die in den vorbehandelten Proben ebenfalls eine größere laterale Korngröße aufweist) zurückzuführen (für weitere Details, siehe Kapitel 2). Die Steigung im Konzentrations-Tiefenprofil an der Stelle der ursprünglichen Grenzfläche zwischen den Schichten ändert selbst bei einer Wärmebehandlung bei einer Temperatur von 300 °C kaum. Dies ist auf eine Abnahme der Dichte von Kristalldefekten (die die Interdiffusion beschleunigen) zurückzuführen.

Die Spannungsentwicklungen während der Wärmebehandlungen können wie folgt diskutiert werden: Abgesehen von rein thermoelastischem Verhalten können weitere Mechanismen den Spannungszustand eines Schichtsystems auf einem Substrat während einer Wärmebehandlung verändern [3]: (i) Kornwachstum, (ii) Defektannihilation und Verkleinerung von Hohlräumen an Korngrenzen, (iii) plastische Verformung, (iv) Phasenumwandlungen und (v) Interdiffusion.

Die Mechanismen (i) und (ii) (thermisch aktivierte Relaxationsprozesse) treten bei Schichten, die bei Temperaturen um Raumtemperatur mittels Sputtern hergestellt wurden, nach der Abscheidung im Allgemeinen auf, wenn die Temperatur erhöht wird (wenn nicht sogar schon bei Raumtemperatur). Diese Relaxationsprozesse bewirken eine Verdichtung der Schicht durch die Annihilation überschüssigen Volumens in Defekten und Korngrenzen und sorgen dadurch für den Aufbau von Zugeigenspannungen in den Schichten. Während Mechanismus (iii) immer zu einer Spannungsrelaxation (d.h. einer Abnahme des Spannungsbetrages) führt, kann das Auftreten der Mechanismen (iv) und (v) abhängig vom Vorzeichen der Nettovolumenänderung in einer Schicht einen Spannungsbeitrag sowohl in Richtung Druck als auch in Richtung Zug leisten.

Für die Cu- und Ni-Einzelschichten können Zugspannungsbeiträge, die durch Stabilisierungsprozesse (Prozesse (i) & (ii); siehe oben) entstehen, aus den Unterschieden zwischen oberhalb von Raumtemperatur gemessenen und den auf Basis des rein thermoelastischen Verhaltens extrapolierten Spannungswerten

berechnet werden. Für die Einzelschichten des Diffusionspaares jedoch stellt der Unterschied zwischen thermoelastischer Spannung und gemessener Spannung eine Summierung über durch thermisch aktivierte Prozesse und durch Interdiffusion hervorgerufene Spannungen dar.

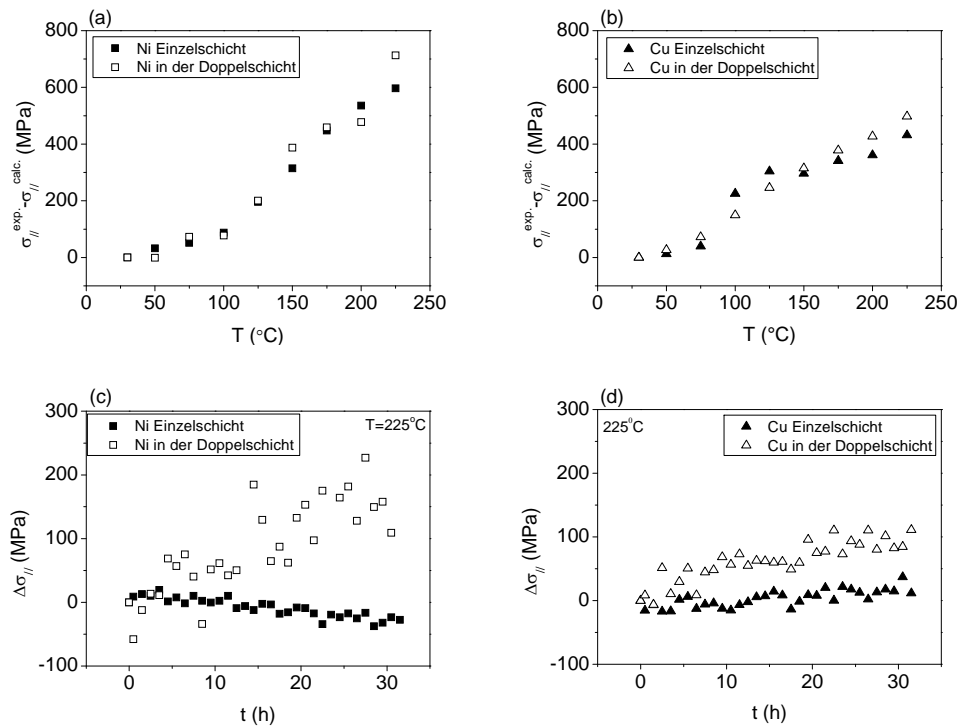


Abb. 6.2. Experimentell ermittelte und auf thermoelastische Spannungen korrigierte Spannungsverläufe für (a) Ni-Einzelschicht und Ni-Schicht der nicht vorbehandelten Doppelschichten, (b) Cu-Einzelschicht und Cu-Schichten der nicht vorbehandelten Doppelschicht beim Aufheizen auf 225 °C; (c) Ni-Einzelschicht und Ni-Schicht der nicht vorbehandelten Doppelschicht, (d) Cu-Einzelschicht und Cu-Schicht der nicht vorbehandelten Doppelschicht bei isothermer Wärmebehandlung bei 225 °C.

Durch Vergleich der Ergebnisse aus den Messungen der Einzelschichten mit denen der Doppelschichten erhält man daher Informationen über diffusionsbedingte Spannungen (siehe Abbildung 6.2). Nach Abzug der thermoelastischen Spannungen zeigt sich, dass sowohl für die jeweiligen Einzel- als auch für die Doppelschichten für den Fall der nicht vorbehandelten Schichten beim Aufheizen erhebliche Zugspannungen entstehen. Es müssen also weitere Mechanismen zur Spannungsentwicklung beitragen: Dafür kommen plastische Relaxation von Druckspannungen und/oder Zugspannungen bedingt durch Kornwachstum und/oder

das Ausheilen von Defekten in Betracht. Die in-situ Bestimmung der Kristallitgrößen mittels Linienprofilanalyse zeigt in der Tat, dass beim Aufheizen Kornwachstum auftritt. Es erscheint also plausibel, dass die experimentell ermittelten Zugspannungen in den Einzel- und Doppelschichten beim Aufheizen durch Kornwachstum verursacht werden.

Offensichtlich ergeben sich für die Einzelschichten keine signifikanten Spannungsänderungen während der isothermen Wärmebehandlung. Hingegen entstehen, insbesondere für die Ni-Schicht, Zugspannungen.

Für die vorbehandelten Proben kann der Spannungsverlauf beim Aufheizen und Abkühlen im Wesentlichen als rein thermoelastische Spannungsentwicklung verstanden werden: Durch die verminderte Dichte von Korngrenzen (siehe oben) tritt beim Aufheizen kein weiteres Kornwachstum auf. Bei der Wärmebehandlung bleiben die Spannungen in den Schichten nahezu konstant, da weder Kornwachstum noch ausgeprägte Interdiffusion auftreten (für Details, siehe Kapitel 2).

Für die nicht vorbehandelten Schichten kann der Einfluss der Interdiffusion auf die Spannungsentwicklung als Überlagerung von Spannungen durch die folgenden beiden Prozesse verstanden werden: (i) Spannungen entstehen wenn der Fluss von Ni-Atomen nicht durch einen betragsmäßig gleich großen Rückfluss von Cu-Atomen kompensiert wird (Kirkendall-Effekt). (ii) Spannungen entstehen auf Grund der unterschiedlichen Molvolumina von Ni und Cu. Ein mathematische Betrachtung der mit der Interdiffusion verbundenen Volumenänderungen der beiden Subschichten zeigt, dass die in der Ni-Schicht entstehenden Zugspannungen als Konsequenz des Interdiffusionsprozesses verstanden werden können, wohingegen für die Cu-Schicht weitere spannungserzeugende Mechanismen aktiv sein müssen. Hierfür kommen insbesondere fortgesetztes Kornwachstum sowie das Ausheilen von Kristalldefekten in Frage. Für weitere Details, siehe Kapitel 2.

Abhängigkeit des Gitterparameters von Metallen von der Kristallitgröße; Untersuchungen an dünnen, nanokristallinen Schichten – Kapitel 3

In den Experimenten wurden Cu, Pd und Ni Dünnschichten (Schichtdicken im Bereich zwischen 20 nm und 100 nm) untersucht, die bei Raumtemperatur auf (100)-orientierte Si-Wafer, welche mit dünnen amorphen SiO₂ und Si₃N₄

Diffusionsbarrieren (je 50 nm dick) beschichtet waren, mittels DC Magnetronspütern unter Hochvakuum-Bedingungen (Basisdruck ungefähr 5×10^{-8} mbar) abgeschieden wurden. Röntgenbeugungsmessungen wurden an einem Diffraktometer, das mit einer auf einer Eulerwiege montierten Heiz-/Kühlkammer ausgerüstet war, durchgeführt (siehe Kapitel 3 für Details der Röntgenbeugungsmessungen).

Zunächst wurden spannungsfreie Gitterebenenabstände der Schichten mittels röntgenographischer in-situ Eigenspannungsanalyse ermittelt. Die Kristallitgrößen wurden mittels der Einzellinienanalyse aus der Linienverbreiterung der Röntgenbeugungslinien bestimmt. Als neue Methode zur in-situ Untersuchung der Abhängigkeit des Gitterparameters von der Kristallitgröße wurde das folgende Messverfahren („loop annealing“) entwickelt: Die gesputterten, nanokristallinen Schichten werden in der auf dem Diffraktometer montierten Heizkammer sequentiell bei ansteigenden Temperaturen einer isothermen Wärmebehandlung unterzogen. Nach jedem isothermen Behandlungsschritt werden die Proben zur Durchführung der Röntgenbeugungsmessungen auf Raumtemperatur abgekühlt. Für jeden Wärmebehandlungsschritt werden die Proben isochron aufgeheizt, dann für fünf Minuten isotherm gehalten und dann auf Raumtemperatur abgekühlt (undefinierte Kühlrate durch freies Abkühlen in der Heizkammer). Dieses Verfahren hat zwei Vorteile: (i) Alle Röntgenbeugungsmessungen werden bei Raumtemperatur (hier: 30 °C; Temperatur im Diffraktometer) durchgeführt. Das Umrechnen von Gitterparametern, die bei erhöhten Temperaturen gemessen wurden, auf Raumtemperatur entfällt damit (kleine Fehler im Ausdehnungskoeffizienten könnten die Ergebnisse erheblich verfälschen). (ii) Die in-situ Methode verkürzt die Gesamtzeit erheblich; bei einer ex-situ Wärmebehandlung in einem Ofen müsste die Probe bei jeder Wärmebehandlung zwischen dem Diffraktometer und dem Ofen transferiert werden.

Die Untersuchung von nanokristallinen Cu und Pd Schichten ergab, dass für diese Schichten die erwartete Verminderung des Gitterparameters mit abnehmender Kristallitgröße beobachtet werden konnte (für weitere Details, siehe Kapitel 3). Ein grundsätzliches anderes Verhalten ergab sich für die Ni-Schichten: Mit abnehmender Kristallitgröße ergab sich zunächst die erwartete Abnahme des Gitterparameters. Jedoch nahm der Gitterparameter für Kristallitgrößen unterhalb von ca. 45 nm wieder deutlich zu: Siehe Abbildung 6.3.

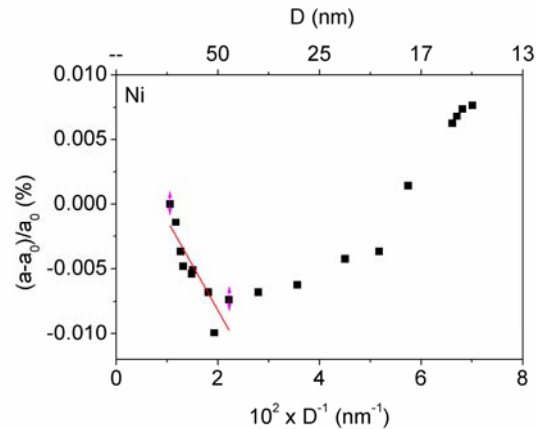


Abb. 6.3. Relative Änderungen des Gitterparameters, $(a-a_0)/a_0$ (a_0 ist der Gitterparameter der für die Schicht mit der größten Kristallitgröße erhalten wurde), für eine 50 nm dicke Ni Schicht die mittels 'loop annealing' (für Details siehe Text) unter Vakuum bis auf 450°C aufgeheizt wurde, aufgetragen gegen die reziproke Kristallitgröße, D^{-1} .

Aus einer Auswertung der Steigung in einer Auftragung der relativen Änderung des Gitterparameters gegen die reziproke Kristallitgröße (bis zu einer Kristallitgröße von 45 nm) kann die Grenzflächenspannung zu (0.93 ± 0.19) N/m bestimmt werden.

Bei der Abnahme der Kristallitgröße unter 45 nm tritt hingegen wieder eine Zunahme des Gitterparameters ein. Eine Zunahme des Gitterparameters (ohne einer vorherigen Abnahme) wurde für nanokristallines Ni bereits berichtet und dort der Abnahme des intrakristallinen Drucks (resultierend aus den Kräften der elektrostatischen Wechselwirkungen der Ionen und Elektronen im Metallgitter) mit abnehmender Kristallitgröße zugeschrieben [8]. In der gegenwärtigen Arbeit wird noch der folgende alternative Erklärungsansatz vorgeschlagen: Nickel ist ferromagnetisch. Es wird deswegen vorgeschlagen, dass der Übergang von einer Abnahme des Gitterparameters zu einer Zunahme durch die Entstehung einer Dömanenstruktur bedingt ist, bei der anstelle von mehreren unterschiedlichen Domänen in einem Korn bei einer kritischen Korngröße nur noch eine Domäne vorliegt. Beim Übergang von einer Struktur mit mehreren Domänen zu einer Struktur mit einer Domäne stellt sich für das gesamte Korn eine einheitliche Magnetisierung ein. Dieser Übergang tritt für ein kugelförmiges Nickel-Korn bei ca. 42 nm Durchmesser ein [9-10]; dieser Wert stimmt in der Tat mit der beobachteten kritischen Korngröße überein, bei der der Übergang von einer Abnahme des Gitterparameter zu einer Zunahme auftritt.

Abhängigkeit des Gitterparameters von Nickel von der Kristallitgröße; Vergleichende Untersuchungen an dünnen, nanokristallinen Schichten und kugelmahlenen, nanokristallinen Pulvern – Kapitel 4

In den Experimenten wurden Ni Dünnschichten (Schichtdicke 50 nm) untersucht, die bei Raumtemperatur auf (100)-orientierte Si-Wafer, welche mit dünnen amorphen SiO₂ und Si₃N₄ Diffusionsbarrieren (je 50 nm dick) beschichtet waren, mittels DC Magnetronspütern unter Hochvakuum-Bedingungen (Basisdruck ungefähr 5×10⁻⁸ mbar) abgeschieden wurden. Röntgenbeugungsmessungen wurden an einem Diffraktometer, das mit einer auf einer Eulerwiege montierten Heiz-/Kühlkammer ausgerüstet war, durchgeführt (siehe Kapitel 4 für Details der Röntgenbeugungsmessungen). Zunächst wurden spannungsfreie Gitterebenenabstände der Schichten mittels röntgenographischer in-situ Eigenspannungsanalyse ermittelt. Die Kristallitgrößen wurden mittels der Einzellinienanalyse aus der Linienverbreiterung der Röntgenbeugungslinien bestimmt. Als neue Methode zur in-situ Untersuchung der Abhängigkeit des Gitterparameters von der Kristallitgröße wurde das bereits oben (siehe Kurzfassung von Kapitel 3) beschriebene Messverfahren ‚loop annealing‘ angewendet.

Desweiteren wurde Ni-Pulver (Reinheit 99.8 Gew.-%) mit einer Partikelgröße kleiner 50 µm für Zeiten zwischen einer Minute und 80 Stunden bei Raumtemperatur einer Mahlbehandlung in einer Planetenkugelmühle unterworfen. Zum Mahlen wurden ein Ni-Mahlbecher und Ni-Mahlkugeln verwendet um Verunreinigungen der Pulver durch Abrieb vom Mahlwerkzeug zu vermeiden. Die Pulver wurden in einem Handschuhkasten unter Ar-Atmosphäre in den Mahlbecher eingefüllt. Um weitere Kristallitgrößen einzustellen wurden Pulver, die zunächst für fünf Stunden gemahlen worden waren, in Quarz-Ampullen verschlossen und danach isothermen Wärmebehandlungen zwischen 250 °C und 375 °C unterzogen. Die Kristallitgrößen wurden mittels der Einzellinienanalyse aus der Linienverbreiterung der Röntgenbeugungslinien bestimmt. Gitterparameter wurden aus den gemessenen Beugungswinkeln nach der Korrektur von instrumentellen Fehlern und von Verschiebungen durch Stapelfehler bestimmt.

Mit fortschreitender Mahldauer nimmt die Kristallitgröße schnell innerhalb der ersten Stunde bis auf ca. 30 nm ab, gefolgt von einer langsameren Abnahme bis auf ca. 18 nm. Nach ca. 30 Stunden stellt sich ein Gleichgewichtszustand ein. Die Mikrodehnung nimmt mit zunehmender Mahldauer ebenso wie die Stapelfehlerwahrscheinlichkeit kontinuierlich zu, welche nach 80 Stunden einen Wert von ca. 0.6% erreicht.

Abbildung 6.4 zeigt die nach Durchführung der Korrekturen erhaltenen relativen Änderungen des Gitterparameters als Funktion der reziproken Kristallitgröße. Der bereits für die nanokristallinen Ni-Dünnschichten erhaltene Übergang von Gitterkontraktion zu Gitterexpansion (siehe oben) ergibt sich auch für die kugelmahlenen (und zum Teil wärmebehandelten) Ni-Pulver. Desweiteren liegen die relativen Änderungen des Gitterparameters für nanokristalline Schichten und kugelmahlene Pulver in der gleichen Größenordnung. Dieser Übergang scheint damit ein für Ni universelles Phänomen darzustellen, das sowohl in nanokristallinen Schichten wie auch in nanokristallinen Pulver auftritt. Die Art der Herstellung scheint hierbei keine Rolle zu spielen (für eine Diskussion des Übergangs von Abnahme des Gitterparameters zur Zunahme, siehe Kapitel 3 und 4 sowie die deutsche Kurzfassung von Kapitel 3 oben).

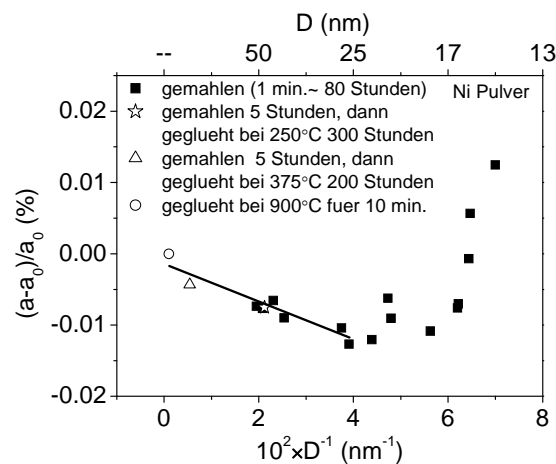


Abb. 6.4. Relative Änderungen des Gitterparameters, $(a-a_0)/a_0$ (a_0 ist der Gitterparameter der für eine bei 900 °C für 10 Minuten wärmebehandelte Probe erhalten wurde) für Ni Pulver aufgetragen gegen die reziproke Kristallitgröße, D^{-1} . Die Pulver wurden durch Kugelmahlen (schwarze Quadrate) und Wärmebehandlungen bei unterschiedlichen Temperaturen (offene Symbole, wie in der Legende beschrieben) hergestellt.

References for Chapter 5 and Chapter 6

- [1] Freund LB, Suresh S. Thin film materials: stress, defect formation, and surface evolution. Cambridge: Cambridge university press, 2006.
- [2] Ohring M. The materials science of thin films. San Diego: Academic press, 2002.
- [3] Doerner MF, Nix WD. Crc Critical Reviews in Solid State and Materials Sciences 1988;14:225.
- [4] Chakraborty J, Welzel U, Mittemeijer EJ. J. Appl. Phys. 2008;103.
- [5] Vermaak JS, Mays CW, Kuhlmann D. Surface Science 1968;12:128.
- [6] Levasseur J, Philibert J. CR. Acad. Sci. Paris 1967;264:277.
- [7] Lefakis H, Cain JF, Ho PS. Thin Solid Films 1983;101:207.
- [8] Cullity BD, Graham CD. Introduction to Magnetic Materials: Wiley-IEEE Press, 2008.
- [9] Kitakami O, Sakurai T, Miyashita Y, Takeno Y, Shimada Y, Takano H, Awano H, Ando K, Sugita Y. Jpn. J. Appl. Phys. Part 1 1996;35:1724.
- [10] Brown WF. Phys. Rev. 1957;105:1479.

List of publications

- [1] J. Sheng, G. Rane, U. Welzel, E.J. Mittemeijer, The lattice parameter of nanocrystalline Ni as function of crystallite size, *Acta Mater* (in preparation).
- [2] J. Sheng, U. Welzel, E.J. Mittemeijer, Interdiffusion and stress development in Ni-Cu thin film diffusion couples, *Zeitschrift für Kristallographie* (2009) 247-252.
- [3] J. Sheng, U. Welzel, E.J. Mittemeijer, In-situ X-ray diffraction investigations during diffusion anneals of Ni-Cu thin film diffusion couples, *Advanced Materials Research* 89-91 (2010) 503.
- [4] J. Sheng, U. Welzel, E.J. Mittemeijer, Interdiffusion, solid solution formation and decomposition and stress development in thin-film Ni-Cu diffusion couples, *Journal of Materials Research* (in preparation).
- [5] J. Sheng, U. Welzel, E.J. Mittemeijer, Non-monotonic crystallite-size dependence of the lattice parameter of thin films of metals, *Applied Physics Letters* (in preparation).

Acknowledgement

This work has been performed at the Max Planck Institute for Metals Research in Stuttgart and at the Institute for Materials Science at the University Stuttgart.

Above all I would like to thank Prof. Dr. Ir. E.J. Mittemeijer for his expert guidance during numerous fruitful discussions and the constant encouragement which contributed considerably to the completion of this work.

My sincere gratitude is expressed to Prof. Dr. J. Bill and Prof. Dr. Th. Schleid for agreeing to be my thesis examiners.

I am immensely thankful to my daily supervisor Dr. U. Welzel for innumerable discussions throughout the progress of my work. It was his expertise and inspiration that facilitated every step of my work. Apart from the great scientific help, his kindness and care make my research life in Germany much easier and smoother.

Dr. J.Y. Wang and Dr. Z.M. Wang are especially thanked for assistance in discussing experimental results and providing information about living and traveling inside and/or outside Germany throughout my doctoral study.

This Ph.D. project was made possible by a grant from the International Max Planck Research School for Advanced Materials (IMPRS-AM)

I would also like to thank all colleagues in the Department Mittemeijer for their assistance during my research and for the pleasant time with them.

Finally, I would like to take the chance to express my gratitude to my wife, Weiwei Shen, for being such a wonderful supporter and “secondary” daily supervisor.

Curriculum Vitae

Personal

Name: Jianfeng Sheng
Date and Place of Birth: 01.06.1980, Ningxia, China
Marital status: Married
Nationality: Chinese

Schooling

1996-1998 The 3rd high school of Shizuishan, Ningxia, China

Higher education

1998-2002 B.Sc. (Materials Science and Engineering), Chongqing University, Chongqing, China
2003-2006 M. Sc. (Materials Science and Engineering), Tsinghua University, Beijing, China

Dissertation

2006-2010 Ph.D. student at Max Planck Institute for Metals Research and University Stuttgart
Title: "Stresses in nanocrystalline materials".